2D Materials Based on Main Group Element Compounds: Phases, Synthesis, Characterization, and Applications

Ziyang Lu, Guru Prakash Neupane, Guohua Jia, Haitao Zhao, Dongchen Qi, Yaping Du,* Yuerui Lu,* and Zongyou Yin*

2D materials based on main group element compounds have recently attracted significant attention because of their rich stoichiometric ratios and structure motifs. This review focuses on the phases in various 2D binary materials including III–VI, IV–VI, V–VI, III–V, IV–V, and V–V materials. Reducing 3D materials to 2D introduces confinement and surface effects as well as stabilizes unstable 3D phases in their 2D form. Their crystal structures, stability, preparation, and applications are summarized based on theoretical predictions and experimental explorations. Moreover, various properties of 2D materials, such as ferroelectric effect, anisotropic optical and electrical properties, ultralow thermal conductivity, and topological state are discussed. Finally, a few perspectives and an outlook are given to inspire readers toward exploring 2D materials with new phases and properties.

1. Introduction

Since the discovery of graphene, material scientists have witnessed a rapid expansion of the 2D material family owing to its unusual electronic, mechanical, and optical properties.[1] Compared with the extensively studied graphene and transition metal dichalcogenides (TMDs), 2D binary materials based on main group element compounds have a more complex layer structure and have recently received increasing research interest because of their novel optoelectronic properties.[2,3] Unlike TMDs, the d orbitals in the main group elements, which are also called blocked d orbitals, are fully occupied.

During the formation of compounds, the main group elements contribute electrons only from the s and p orbits. Thus, there are many forms of these compounds, such as MX, M_2X_3, M_3X_4, and MX_2 (M can be mixed oxidation states), which form monolayer structures with X–M–M–X, X–M–X–M–X, and X–M–X–M–X–M–X motifsapart from the sandwich structure. These provide significantly more possibilities of phases, properties, and applications of these materials.[2,4,5]

Given an equal composition and stoichiometric ratio, phase engineering is an effective method to determine the physical properties of materials.[6] The combination of phase engineering and the confinement effect in 2D materials enriches their properties and applications. For example, TMDs undergo indirect-to-direct band transitions when bulk materials break down to atom thickness. However, monolayer β-In_2Se_3 shows an indirect band structure, whereas monolayer α-In_2Se_3 has a direct band.[4,7] The 2D SnSe attained a recorded figure of merit (ZT) ≈2.8 through phase engineering. This is derived from the continuous phase transition from *Pnma* to *Cmcm*.[8] Most importantly, the single-layer β-In_2Se_3 becomes stable at room temperature, whereas bulk β-In_2Se_3 crystals can exist only at elevated temperatures.[9] This unstable-to-stable phase transition in the layer structure was observed in other materials as

Dr. Z. Y. Lu, Prof. Z. Y. Yin
Research School of Chemistry
Australian National University
Canberra ACT 2601, Australia
E-mail: zongyou.yin@anu.edu.au

Dr. G. P. Neupane, Prof. Y. R. Lu
Research School of Electrical, Energy and Materials Engineering
College of Engineering and Computer Science
The Australian National University
Canberra ACT 2601, Australia
E-mail: yuerui.lu@anu.edu.au

Dr. G. H. Jia
Curtin Institute of Functional Molecules and Interfaces
School of Molecular and Life Sciences
Curtin University
Perth, WA 6102, Australia

Dr. H. T. Zhao
Materials and Interfaces Center
Shenzhen Institutes of Advanced Technology
Chinese Academy of Sciences
Shenzhen, Guangdong 518055, China

Dr. D. C. Qi
School of Chemistry and Physics
Queensland University of Technology
Brisbane, Queensland 4001, Australia

Prof. Y. P. Du
Key Laboratory of Advanced Energy Materials Chemistry
Tianjin Key Lab for Rare Earth Materials and Applications
Center for Rare Earth and Inorganic Functional Materials
School of Materials Science and Engineering
National Institute for Advanced Materials
Nankai University
Tianjin 300350, China
E-mail: ypdu@nankai.edu.cn

well, such as hexagonal GaTe,[10,11] *Cmcm*-phase SnX,[12] and 1T(α) Te.[13] These observations have inspired the predictions and examinations of a new phase in 2D materials and studies on their potential properties and applications. Many new properties have also originated with these 2D materials, such as ferroelectric effects, anisotropic optical and electrical properties, and ultralow thermal conductivity.[14–17] The stable bulk phase do not display these properties. 2D Bi_2Te_3 and Sb_2Te_3 have shown topologically protected phases and strong quantum spin Hall (QSH) effects.[18] These can enhance the scope of quantum computing. However, no review on the phase structure control of 2D materials, phase transitions, and related properties and applications is available.

This review summarizes recent studies on the different phases of 2D binary materials based on main group element compounds, including III–VI, IV–VI, V–VI, III–V, IV–V, and V–V materials (Table 1). For each material, we discuss the multiphase structures, preparation methods, property characterization, and application demonstration. In addition, we illustrate potential phases of these 2D materials by comparing their bulk and 2D morphologies. Certain strategies for controlling the phases of these 2D materials are also given in this review. This is followed by a discussion and prediction of potential properties of these 2D materials with different phases. Finally, this review highlights the questions and challenges, and indicates the potential for the development of the phase control of these 2D materials.

2. Group III–VI

In this group, indium and gallium chalcogenides have been studied extensively for wide applications in photodetectors, thermoelectric, photocatalysis, and gas sensors. Among these, 2D indium selenide is the most extensively investigated material because of its rich phase and crystal structures and the wide range of applications. In this section, we consider this material as an example to illustrate the many phase structures. Then, we discussed the phase control of 2D materials in this group individually.

Indium selenide compounds including InSe, In_2Se_3, In_3Se_4, In_4Se_3, and In_6Se_7 are systems with different stoichiometric ratios. Different phase structures may exist for a given stoichiometric ratio, e.g., α-, β-, γ-, δ-, and κ-phase In_2Se_3. With regard to 2D structures, only α-, β-, and γ-phase In_2Se_3; β- and γ-phase InSe; and γ-In_3Se_4 are reported. **Figure 1**b–c shows the crystal structure model of 2D In_2Se_3 with the single-layer composition of Se–In–Se–In–Se. The layers are bonded to each other via van der Waals interactions. In α-In_2Se_3, In atoms occupy tetrahedral cages formed by Se packing. In contrast, in β-In_2Se_3, In atoms occupy octahedral cages. α-In_2Se_3 and β-In_2Se_3 can have either a rhombohedral structure α/β(3R) or hexagonal crystal structure α/β(2H). This is determined by the ABCABC and ABAB stacking sequences, respectively.[19] The heat treatment of β-In_2Se_3 can result in the formation of γ-In_2Se_3, which is a defective wurtzite structure (also known as vacancy ordered in screw form, Figure 1d).[20] Calculation[4] shows that the α-phase monolayers have direct bandgaps, whereas the β-phase monolayers have indirect bandgaps. For a stoichiometric ratio of 1:1, the layered MX (M: Ga, In; X: S, Se) with a hexagonal symmetry consists of covalently bonded X–M–M–X. The layers are stacked by van der Waals interactions in the ABAB (β phase) or ABCABC (γ phase) stacking sequences, as shown in Figure 1a.

Yaping Du is currently a Full Professor at the School of Material Science and Engineering, Nankai University. He is also the Director of Tianjin Key Lab for Rare Earth Materials and Applications. His research interests include rare-earth functional materials, colloidal inorganic nanocrystals, and energy storage and conversion applications. He obtained his B.Sc. degree and Ph.D. degree from Lanzhou University and Peking University in 2004 and 2009.

Yuerui Lu is an Associate Professor at Australian National University (ANU). He received his Ph.D. degree from Cornell University, the school of Electrical and Computer Engineering. He holds a B.S. degree in Applied Physics from University of Science and Technology of China. Currently, he is leading the Nano-Electro-Mechanical System (NEMS) Lab at the ANU. His research interests include MEMS/NEMS sensors and actuators, nanomanufacturing technologies, renewable energy harvesting, biomedical novel devices, and 2D materials and devices.
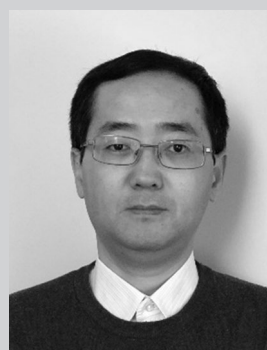
Zongyou Yin obtained his B.S. and M.S. degrees at Jilin University/China, and completed his Ph.D. at Nanyang Technological University (NTU)/Singapore in 2008. He started his postdoc careers at NTU/Singapore, IMRE/Singapore, followed by MIT and then Harvard University. Dr. Yin started his own Research Group at Australian National University from 2017. His group's research is interdisciplinary, encompassing nano-to-atomic materials, fundamental relationship among materials–structures–devices, and synergistic integration of multifunctions toward systems for energy and wearable applications.

Table 1. Summary of the various phases of 2D materials based on main group element compounds.

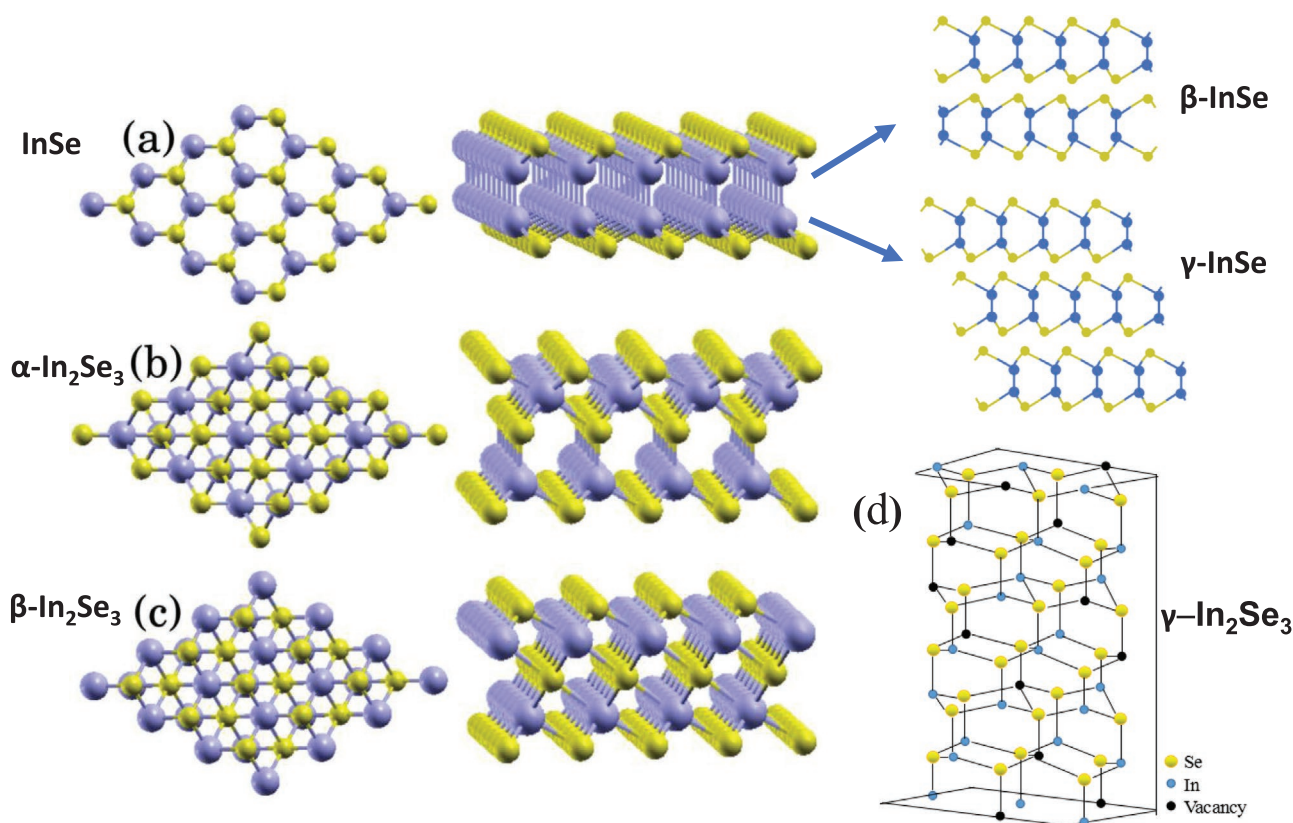|	O	S	Se	Te	N	P	As
B					Amorphous Hexagonal	Hexagonal	Hexagonal
In	Cubic rhombohedral	β	α, β, γ	α	Wurtzite (hexagonal)	Hexagonal Wurtzite cubic	Hexagonal
Ga	α, β, γ, ε amorphous	α, γ	Hexagonal	Monoclinic Hexagonal	Square–octagon (so, haeckelite) Hexagonal		Hexagonal
Si	1T, bitetrahedral Monoclinic	Orthorhombic (α, Pmma) Hexagonal (β)	Orthorhombic (Pmma)	α Orthorhombic (pmn2), β (p3m1)	α, β, γ	Orthorhombic (Cm) Hexagonal (P6m2)	Monoclinic, orthorhombic (Cm) Hexagonal (P6m2)
Ge	1T, bitetrahedral Monoclinic	α, β, γ amorphous	α (orthorhombic, pmmm), β (monoclinic, P21/c), γ (hexagonal), amorphous	Rhombohedral (R3m) Face centered cubic (Fm3m) Simple cubic (Pm3m) Amorphous	Hexagonal (P6m2)	Tetragonal Orthogonal Monoclinic Hexagonal (P6m2)	Monoclinic Orthorhombic (Cm) Hexagonal (P6m2) Pyrite Hexagonal (P6m2)
Sn	1T, bitetrahedral Monoclinic	α, β hexagonal	α (pnma), β (cmcm)	Cubic Rhombohedral	Hexagonal (P6m2)	Hexagonal (P6m2) Orthorhombic (Cm)	Orthorhombic (Cm) Hexagonal (P6m2)
Pb	1T, bitetrahedral Monoclinic	Orthorhombic Cubic	Cubic (Fm3m)	Cubic (Fm3m)		Orthorhombic (Cm) Hexagonal (P6m2)	Orthorhombic (Cm) Hexagonal (P6m2)
Sb	Orthorhombic Cubic	Amorphous Orthorhombic (pmma)	Orthorhombic Amorphous	Amorphous Hexagonal			α, β, γ, δ, ε
Bi	α (monoclinic), β (tetragonal), γ(bcc), δ (disordered)	Orthorhom Rhombohedral Cubic	α, β, γ/δ	A (rhombohedral, R3m), β (monoclinic, C2/m), γ (C2/c), δ (Im3m)			α, β, γ, δ, ε

2.1. In–X (InSe, In_2O_3, In_2S_3, In_2Se_3, In_3Se_4)

2.1.1. InSe

Monolayer group-III monochalcogenides are stacked in the order M–X–X–M. Their structural and electronic properties have been studied extensively.[21] 2D InSe is normally in D_{3h} symmetry, although another phase has been predicted[22] (note: the symbol for phase description may be different in other papers). Therefore, their monolayer structure has only one phase. Multiple-layer InSe can be a β or γ phase based on the stacking sequences. They are obtained mainly by exfoliating their bulk materials. The crystal growth of bulk InSe was optimized, and an equilibrium phase diagram of the In–Se system was investigated.[23]

Petroni et al. demonstrated the liquid-phase exfoliation of β-InSe in 2-propanol, which is a nontoxic and effective solvent.[24] After the exfoliation, β-phase InSe flakes with lateral sizes of 30 nm to a few micrometers and thicknesses of 1–20 nm were prepared. As a catalyst for the hydrogen evolution reaction (HER), the smallest flakes achieved the highest performance because of the rich edge effects.[24] The exfoliated β-InSe nanoflakes also exhibited apparent out-of-plane and in-plane ferroelectricity at room temperature.[25] Feng et al. stated that multilayer β-InSe can also be prepared by the CVD method.[26] The multilayer InSe can be used to fabricate field-effect transistors (FETs), which exhibit ultrahigh carrier mobilities and outperform the reported layer semiconductor-based FETs with a similar device configuration. The impact of thickness on the carrier mobility was investigated, and an optimized thickness of 35 nm was obtained.[26]

In γ-InSe, Se atoms in the second layer were aligned with In atoms of the first-layer InSe, and In atoms in the third layer were aligned with Se atoms of the first layer (Figure 1a). The few-atomic-layer γ-InSe nanosheets were generally prepared via exfoliation.[27,28] Their optical and electrical properties and photodetector application were studied. Herein, the 2D band structure of few-layer InSe was evaluated systematically by the direct correlation between resonance Raman spectra and the photoconductivity.[27] Furthermore, the piezophototronic effect in multilayer γ-InSe enabled the fabrication of self-powered flexible photodetectors with high reliability and stability.[29] Mudd et al. observed strong quantum confinement effects in few-layer γ-InSe flakes with thicknesses of a few nanometers. These could be tuned to the near-infrared spectral region from 1 and 0.8 µm, thereby offering unique opportunities for planar device architectures and near-infrared optical sensing.[28] Because of the high carrier mobility, Bandurin et al. observed the fully developed quantum Hall effect by encapsulating few-layer γ-InSe with different thicknesses in hexagonal boron nitride (h-BN) under protective gas.[30] Photoluminescence spectroscopy revealed that the bandgap increased by over 0.5 eV as the thickness decreased from bulk to bilayer (**Figure 2**c). The monolayer shows an electric band that splits into N sub-bands in the N-layered crystal, inducing an energy difference between the conduction and valence states. The effect of thickness on the high-energy band is weaker than that on the low-energy band (insert Figure 2c). They stated that the encapsulation of atomically thin InSe in h-BN enables the fabrication of

ADVANCED
SCIENCE NEWS
www.advancedsciencenews.com

ADVANCED
FUNCTIONAL
MATERIALS
www.afm-journal.de

Figure 1. Top and side views of a single layer of a) InSe (derived with β and γ phases), b) In$_2$Se$_3$ (α phase), and c) In$_2$Se$_3$ (β phase); d) structures of γ-In$_2$Se$_3$. a–c) Reproduced with permission.[4] Copyright 2015, American Chemical Society.

high-quality optics and electron transport devices. Recently, the quantum Hall effect was also realized by γ-InSe prepared by the chemical vapor transport (CVT) method, which produces high-quality crystals.[31]

An abnormal ε-phase 2D InSe was prepared by controlling the H$_2$ gas flow during the CVD growth and using a low-melting-point In precursor (InI).[32] While growing, undesirable In$_2$Se$_3$ transits into ε-InSe with the help of high H$_2$ content and Se deficiency. These ε-InSe nanoflakes with a noncentrosymmetric structure exhibited a high and accumulated second-harmonic generation (SHG) response with increasing thickness. As an effective and nondestructive method, SHG has been widely used to characterize the phase structure and crystal symmetry of 2D materials. In contrast to the absence of SHG effects in even number TMDs, ε-InSe with all the layer numbers had a noncentrosymmetric structure and was SHG active. Moreover, the nonlinear efficiency of ε-InSe had the highest SHG intensity among all the reported 2D materials.[33]

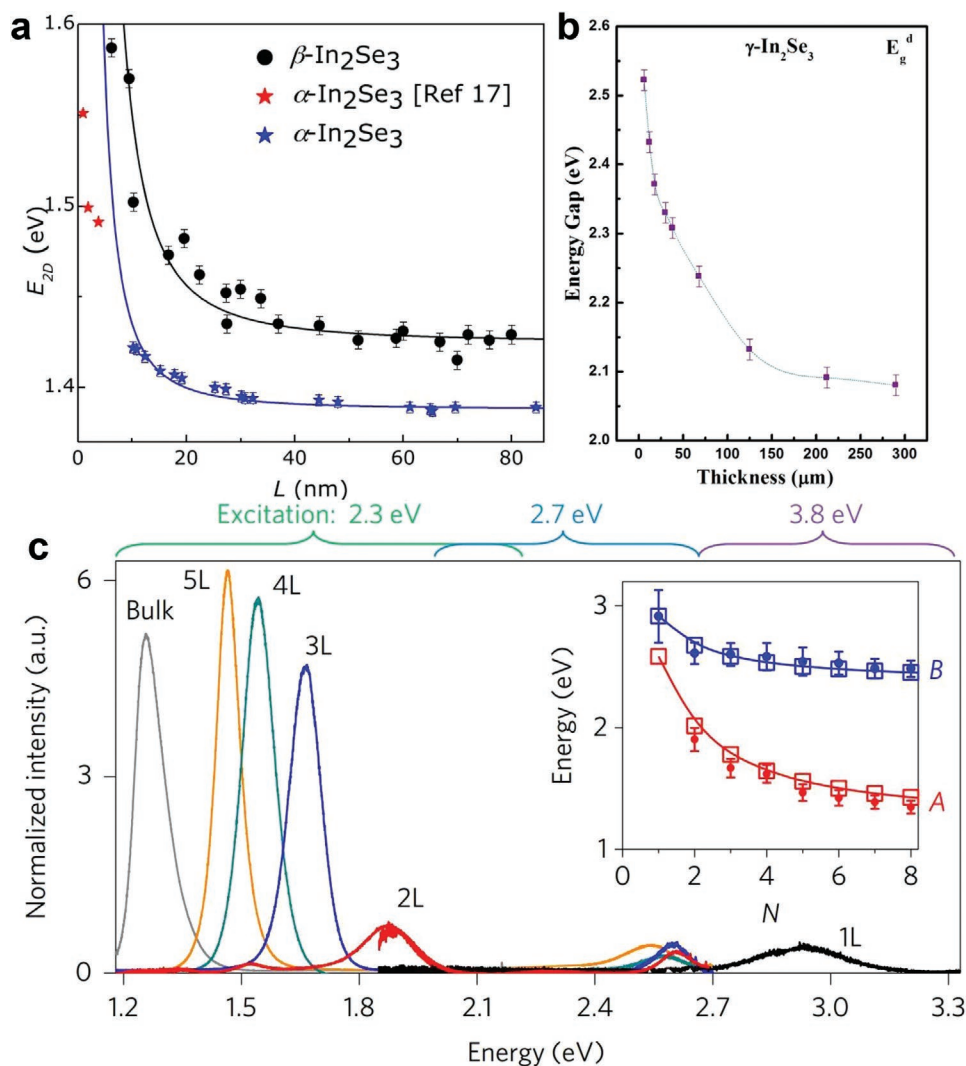### 2.1.2. In$_2$O$_3$, In$_2$S$_3$, In$_2$Se$_3$

Bulk α-In$_2$Se$_3$ is a stable semiconductor with an indirect band. A band transfer from indirect to direct with a decrease in the layer thickness to the atomic scale was verified by calculations and experimental measurements.[4,34] Furthermore, the bandgap was broadened (Figure 2a). α-In$_2$Se$_3$ monolayers can

be obtained via physical vapor deposition (PVD).[35] The size and number of layers can be controlled by the growth time (5 and 15 min for 5 μm monolayers and 10 μm multiple layers). A high temperature (800 °C) results in selenium-rich environments, which makes the material a p-type semiconductor. The carrier mobility (2.5 cm^2 V^{-1} S^{-1}) of the In$_2$Se$_3$ atomic layers is higher than that of materials with layers of group III–VI. This enables In$_2$Se$_3$ transistors to display a remarkable photoresponsivity. Multiple-layer α-In$_2$Se$_3$ phototransistors[36] are also fabricated for FET applications. These produce ultrahigh gain and fast response and high detectivity, thereby demonstrating that α-In$_2$Se$_3$ is a potential material for photodetection applications. An early study showed that few-layer α-In$_2$Se$_3$ is suitable for real-time light detection under very-low light conditions.[34] The performance of α-In$_2$Se$_3$ nanosheets exceeds that of graphene and other layered semiconductors including MoS$_2$, GaS, and GaSe. Multiple-layer α-In$_2$Se$_3$ also shows a thickness-dependent shift in the optical absorption spectra (the corresponding bandgap is from 1.45 to 2.8 eV, Figure 2). It is produced from mechanically exfoliated In$_2$Se$_3$ flakes with a thickness ranging from 3 layers to over 90 layers.[37] Recently, other applications such as wearable strain sensors and ferroelectric devices have been reported.[38] The piezoelectric properties of atom-thick α-M$_2$X$_3$ (M:Ga, In; X:S, Se) were predicted in addition to performing photodetection.[14,39]

Tao et al. first determined that the single-layer β-phase In$_2$Se$_3$ could be stable at room temperature, although its bulk crystals

**ADVANCED
SCIENCE NEWS**

www.advancedsciencenews.com

**ADVANCED
FUNCTIONAL
MATERIALS**

www.afm-journal.de

Figure 2. Thickness-dependent band gaps in a) α, β, and b) γ-In$_2$Se$_3$. The blue stars in (a) are α-In$_2$Se$_3$ flakes produced by exfoliation, and red stars are α-In$_2$Se$_3$ flakes prepared by the physical vapor transport method. a) Reproduced with permission.[41] Copyright 2016, IOP Publishing. b) Reproduced with permission.[49] Copyright 2013, Royal Society of Chemistry. c) PL spectra of InSe, measured at room temperature using different excitation energies (2.3, 2.7, and 3.8 eV). The intensities were normalized by the number of layers, and the intensity of bulk InSe was normalized to fit the scale. The insertion shows a plot of the band energy of two energy lines for different values of N. c) Reproduced with permission.[30] Copyright 2016, Springer Nature.

can exist only at elevated temperatures.[9] The electrical resistance of β-phase In$_2$Se$_3$ is one–two orders of magnitude lower than that of α-phase In$_2$Se$_3$, thereby providing the basis for multilevel phase-change memories in a single-material system. Furthermore, they observed that the α-phase $\rightarrow$ β-phase transition temperature increased with a decrease in the layer thickness. The transition temperature could be increased by 190 K compared with the bulk. This is attributed to the surface effects. The α-phase $\rightarrow$ β-phase transition is also considered to be the basis for the potential pyroelectricity in In$_2$Se$_3$ monolayers.[40] After the demonstration of the room temperature (RT) stability of the layered β-In$_2$Se$_3$ phase, physical[41,42] and chemical methods[7,43] were used to prepare single- and few-layer β-In$_2$Se$_3$ nanosheets. This exhibited their stable and reproducible photoresponsivity as photodetectors. The photodetectors based on β-In$_2$Se$_3$ nanosheets are comparable or superior to those reported previously for α-In$_2$Se$_3$. The bandgap can be tuned by

adjusting the layer thickness (Figure 2a).[41,44] Another derived phase, β', was observed to display reversible thermal transit with the β phase with a thickness ranging from 1 layer to $\approx$20 layers.[43]

However, the reason for the stability of 2D β-In$_2$Se$_3$ is unknown. Tao et al. proposed that energy barriers were created by the layer–substrate interaction to prevent the reverse transition from β-phase to α-phase. However, suspended monolayer β-In$_2$Se$_3$ was prepared in Ref. [7] using a thermosolvent method. In this work, amino nitriles were used as directing agents for the growth of the 2D morphology. We conjecture that as strong electron–donor molecules, these nitriles may also contribute to the stability of β-In$_2$Se$_3$. This phenomenon is similar to that of the stability of 1T-phase MoS$_2$ nanosheets, in which electron-rich m[9] molecules favor the octahedral d orbits in the 1T phase. Furthermore, the critical thickness (layers) for the RT stability of the β phase has not been addressed either.

**ADVANCED
SCIENCE NEWS**

www.advancedsciencenews.com

**ADVANCED
FUNCTIONAL
MATERIALS**

www.afm-journal.de

Perspectives with regard to β-In$_2$Se$_3$ are also conflicting. First, Julien et al.[45] and Almeida et al.[7] reported that bulk β-In$_2$Se$_3$ has a direct bandgap. Moreover, a direct-to-indirect bandgap transition occurs when the number of layers is reduced, as established by the quenching of PL in few-layer β-In$_2$Se$_3$.[41] However, a first-principle calculation[4] shows that bulk β-In$_2$Se$_3$ is an indirect semiconductor. Second, the bandgap of 2D β-In$_2$Se$_3$ reported recently is higher than that of α-In$_2$Se$_3$. This is in contrast to the calculation results[4] and earlier experimental report (at high T).[45] Furthermore, its higher conductivity (by one–two orders of magnitude) than α-In$_2$Se$_3$ cannot be explained.

Applications of combinations of α/β phases have also been reported. In$_2$Se$_3$ is a good material for thermoelectric devices. The fabrication of 2D-phase devices (e.g., α on β (α/β) and β on α (β/α)) produces van der Waals Schottky junctions and significantly enhances the thermoelectric properties, with ZT values approaching ≈ 1.[46] Another popular application is phase change ($\alpha \rightarrow \beta$) memory, which was realized by applying pressure on bulk In$_2$Se$_3$ and nanowires.[47] However, this application has not been reported in 2D In$_2$Se$_3$.

In the case of γ-In$_2$Se$_3$, physical[48,49] and chemical methods[50,51] have been applied to prepare nanosheets. Similar to other 2D materials, the bandgap (direct) can be tuned and varied from ≈ 2 to over 2.52 eV with various thicknesses (Figure 2b). Nanoflowers were assembled from p-type γ-In$_2$Se$_3$ nanosheets using the hot-injection thermosolvent method. These showed high performance of self-powered broadband while forming heterojunction photodiodes with n-type Si.[50] It is noteworthy that a recent paper[48] reported the physical vapor transport epitaxial growth of $\alpha/\beta/\gamma$-In$_2$Se$_3$ and γ-InSe on GaSe simultaneously. γ-In$_2$Se$_3$, β-In$_2$Se$_3$, α-In$_2$Se$_3$, and γ-InSe were formed in sequence from high to low temperatures (580–500 °C). Their bandgaps range from 1.3 to 2 eV, which is suitable for application in electronics and optoelectronics.

With regard to 2D In$_2$S$_3$, the β phase is the most popular because it is stable at room temperature.[52] β-In$_2$S$_3$ has noteworthy optical, electronic, and optoelectronic properties because of its natural defective structure with misvalency between In and S atoms. β-In$_2$S$_3$ can be prepared through various methods including chemical vapor deposition (CVD) as well as solvothermal and hydrothermal synthesis. It was used for photocatalysis,[53] photodetector,[54] and photoelectrochemical (PEC) processes.[55] In general, the CVD method is more effective than the others in terms of the controllability of the shape and thickness of β-In$_2$S$_3$ nanosheets grown. 2D γ-In$_2$S$_3$ was recently prepared by decomposing indium thiolate at a retarded low temperature. Higher temperatures and longer reaction times generate β-In$_2$S$_3$ nanoplates with the same system. The γ-phase $\rightarrow$ β-phase transition mechanism has been studied. The γ-In$_2$S$_3$ nanoplates exhibited high stability at room temperature. The properties and applications of this 2D γ-In$_2$S$_3$ need to be investigated further. The In$_2$Te$_3$ nanostructures of nanoparticles and nanowires with α/β phases have been widely reported.[56] However, their 2D structures are not popular. Only the α phase has been prepared by the hydrothermal or CVD technique.[57]

In$_2$O$_3$, another semiconductor compound with a direct bandgap of ≈ 3 eV, has also been reported.[58] In$_2$O$_3$ nanosheets have been prepared in multiple steps by combining hydrothermal and calcination techniques.[59,60] Their phases can be cubic or rhombohedral, which depends on the conditions during the preparation of InOOH.[59–61] In general, cubic-phase nanosheets are obtained with a standard hydrothermal operation.[60] However, with the help of oxalic acid, rhombohedral InOOH is first formed and then transferred into rhombohedral-phase In$_2$O$_3$ after calcination.[59] Both the phases are suitable for gas sensor (NOx, xylene, and amine) applications.[59–61]

2.1.3. In$_3$Se$_4$

In terms of 2D In$_3$Se$_4$, only the γ phase (rhombohedra, Rm) has been reported with a layer structure consisting of Se–In–Se–In–Se–In–Se. These γ-In$_3$Se$_4$ nanosheets can be prepared by the solvothermal method. The synthesis conditions were optimized to control the thickness to 20–40 nm.[62] This material is an n-type semiconductor with a bandgap of ≈ 0.55 eV and can be stable at 900 °C in N$_2$, 550 °C in Ar, and 200 °C in air.[63] A simulation also showed that In$_3$Se$_4$ and In$_3$Te$_4$ are stable and that the interlayer binding energies are low enough to obtain isolated-layer In$_3$Se$_4$ and In$_3$Te$_4$ structures.[64] Therefore, the new phases and properties of this material need to be explored further.

2.2. Ga-X (GaS, GaSe, GaTe, Ga$_2$O$_3$, Ga$_2$S$_3$)

2.2.1. GaS, GaSe, GaTe

In the Ga monochalcogenide system, GaS and GaSe have a structure similar to that of InSe. Their 2D materials have many applications such as photodetectors,[65][66] piezophototronic,[67] hydrogen evolution catalysts,[68] and SHG.[69] Similar to InSe, the β, γ, and ε phases of multiple-layer GaSe nanosheets are available, depending on the stacking sequences of Se–Ga–Ga–Se layers.[70] The bulk β and ε-GaSe are stable phases because their free energies are highly similar. When the thickness decreases to atomically thin, the β phase becomes more stable with a lower energy than that of the ε phase.[71] Therefore, the nonlinear properties of few-layer GaSe nanosheets prepared via exfoliation differ between thicknesses above five layers and those less than five layers. The SHG showed a cubic dependence for thicknesses below five layers and a quadratic dependence for thicknesses beyond five layers.[71] Meanwhile, 2D ε-GaSe developed by mechanical exfoliation has been widely reported. It has shown robust piezoelectric and piezo-phototronic effects from local strains, making it suitable for flexible and nanomicroelectromechanical systems.[67] Exfoliated ε-GaSe nanosheets can also realize multiple second-order nonlinear processes even with very-low power wave pumps when integrated with a photonic crystal cavity.[72] ε-GaSe nanosheets display an ultrahigh on/off ratio and ultralow set/reset electric fields while functioning as a resistive switching layer in a memristor device.[73]

Monolayer GaTe showed an additional monoclinic phase apart from the hexagonal structure (**Figure 3**a). The monoclinic phase is more stable than the hexagonal phase.[74] GaTe nanosheets consist of alternate Te–Ga–Ga–Te layers bonded via van der Waals interactions. Similar to GaS and GaSe, in the hexagonal phase, all the Ga–Ga bonds were perpendicular to the layer planes.
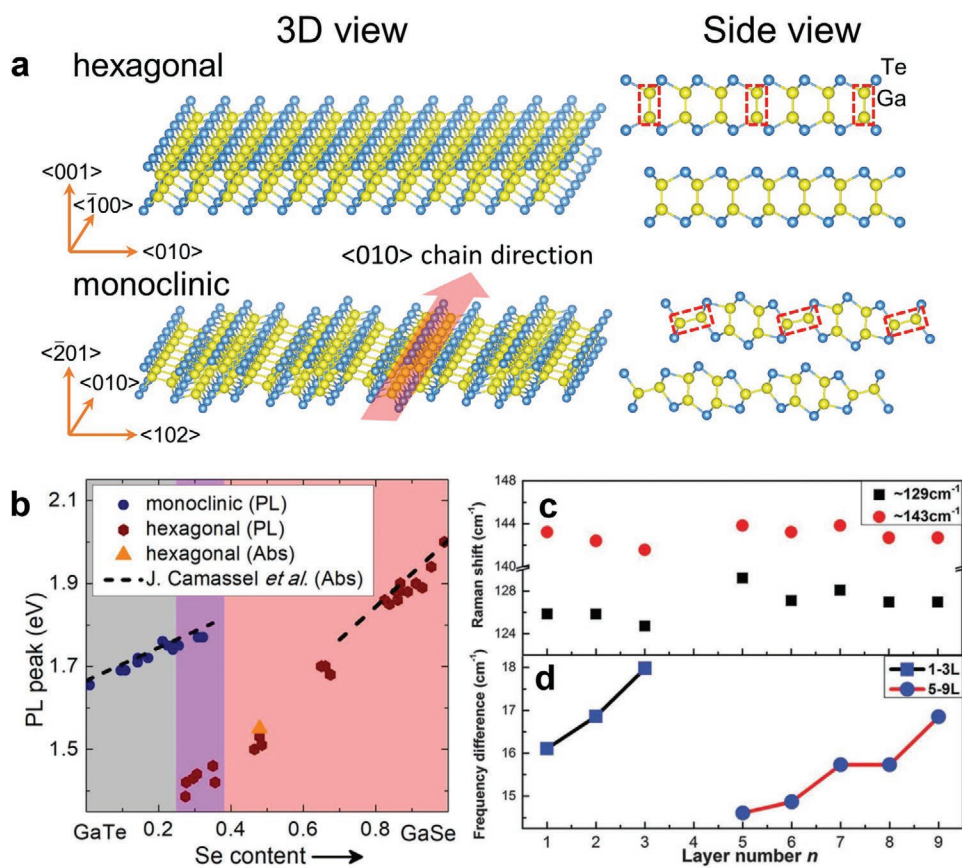
Figure 3. a) Schematics of the crystal structure of hexagonal and monoclinic GaTe. a) Reproduced with permission.[74] Copyright 2017, Wiley-VCH. b) the phase dependence of the PL peak energy on the Se content in hexagonal and monoclinic GaTe. b) Reproduced with permission.[78] Copyright 2018, American Chemical Society. c) Positions of the two Ag Raman-active modes at 129 and 144 cm^{-1} as a function of the number of layers. d) Raman frequency difference of A_g modes versus the number of layers, n. c,d) Reproduced with permission.[10] Copyright 2016, Royal Society of Chemistry.

In contrast, in the monoclinic phase, only two-thirds of the Ga–Ga bonds were perpendicular to the layer planes, and every third Ga–Ga bond was twisted to be almost parallel to that of the other two (Figure 3a). As a result, the monoclinic phase of GaTe had a direct band unlike the indirect bands in GaS and GaSe. This is more suitable for optoelectronic applications.

Multiple-layer GaTe with a monoclinic phase can be prepared via exfoliation because this phase is stable.[75,76] As a low-symmetry (C_{2h}^3) material, its in-plane anisotropic optical properties were studied. The anisotropy of the Raman intensity was strong, and its sensitively was dependent on the excitation laser energy, phonon energy, and GaTe thickness. However, the visible optical extinction showed a weak anisotropic response.[76] The photoresponse of monoclinic-phase GaTe nanosheets with more than five layers was investigated. The observations revealed a faster response and higher photoresponsivity than those of the MoS_2 photodetector.

Fonseca et al. doped Se in $GaSe_xTe_{1-x}$ alloys to obtain a metastable hexagonal phase. Here, the hexagonal phase was prepared when the Se content was above 20% (Figure 3b).[77] Cai et al. further indicated the presence of a mixed region, where both the phases could coexist, and two bandgaps for the same composition.[78] Zhao et al. observed that the metastable hexagonal phase may resist when the number of layers decreases

further to 1–3 because of the surface effect.[10] Raman spectra showed two A1 vibrational modes located at 129 and 144 cm^{-1}. A blue shift was observed as the number of layers decreased, owing to the surface contraction. This caused the frequency difference between the two peaks to decrease, which is similar to other 2D materials. However, there is a large gap between three and five layers, as shown in the figure. This indicates that four layers constitute the critical thickness for the phase transition from monoclinic to hexagonal crystal (Figure 3c–d). Gillan et al. reported that the decomposition of metal–organic precursors can directly produce hexagonal GaTe. However, further annealing at 500 °C altered the phase to monoclinic.[11] This work provides an important indication that temperature control may be a crucial factor for the synthesis of metastable 2D materials. Recently, Zhai et al. obtained hexagonal 2D GaTe via physical vapor deposition at a relatively low temperature. Here, the hexagonal phase transited to the monoclinic phase under irradiation with femtosecond laser.[79]

2.2.2. Ga_2O_3, Ga_2S_3

There are five polymorphs of bulk Ga_2O_3, namely, α, β, γ, δ, and ε. The two polar phases, β and γ phases, were particularly

**ADVANCED
SCIENCE NEWS**
www.advancedsciencenews.com

**ADVANCED
FUNCTIONAL
MATERIALS**
www.afm-journal.de

noteworthy in applications because of their remarkable pyro-electric, piezoelectric, and ferroelectric properties. β-Ga_2O_3 has a monoclinic structure and is the most stable phase. The meta-stable-phase γ-Ga_2O_3 had a defective spinel-type structure containing cation vacancies in tetrahedral and octahedral sites.[80]

All the 2D Ga_2O_3 films prepared by CVD were in the β phase.[81] Because of their wide bandgap ($\approx$4.8 eV), these are widely used in middle ultraviolet radiation detectors,[82] deep ultraviolet photodetectors,[83] and photocatalysis.[84] Oxidizing 2D GaSe[85] or gallium nitride (GaN)[86] with O_2 at high temperatures can also directly produce β-Ga_2O_3 nanosheets. The photodetector based on this 2D polycrystalline β-Ga_2O_3 shows a sensitive, fast, and stable photoresponse to 254 nm ultraviolet light.[85]

The hydrothermal technique is a common method to prepare γ-Ga_2O_3 nanosheets. These can enhance the photocatalytic efficiency and stability of water splitting compared with bulk γ-Ga_2O_3.[87] Other applications such as solar-blind photodetectors [88] and heterogeneous catalytic performances for thiophenes[89] were also based on hydrothermally prepared γ-Ga_2O_3.

Patil et al. reported a noteworthy work for controlling $\alpha/\beta/\gamma$-Ga_2O_3 on rGO by adjusting the ratio of GaOOH/GO before heat treatment in Ar. α-, β-, and γ-Ga_2O_3 on rGO were prepared by increasing the ratio from 6% to 14% and to 25%. When the ratio was 10%, all the phases of $\alpha/\beta/\gamma$ Ga_2O_3 were formed on rGO. This mixture phase composite showed significantly higher performance as an electrode in Li-ion batteries than others.[90] Recently, a new form of amorphous Ga_2O_3 layers was deposited on a flexible substrate at room temperature via radiofrequency magnetron sputtering and then fabricated into a bendable solar-blind photodetector.[91]

In 2D forms, few papers on Ga_2S_3 have been published. The thermal vapor sulfurization of the GaAs substrate can yield three layers of Ga_2S_3, with γ-Ga_2S_3 (cubic) as layer 1, polycrystalline γ-Ga_2S_3 as layer 2, and polycrystalline α-Ga_2S_3(monoclinic) at the top. A phase change from cubic to monoclinic Ga_2S_3 in layers 1 and 2 was observed during the peeling-off and rolling-up processes. This resulted in a significantly high ratio of mono-clinic microtubes.[92] Pure γ-phase 2D Ga_2S_3 was successfully synthesized via the CVD method. Its thickness was controllable from 9 to 60 nm with a lateral size of $\approx$10 μm.[93] When the thickness decreased to 3 nm, the crystallization was low because of its monolayered nature. This 2D γ-Ga_2S_3 exhibited a wide spectrum response range and remarkable photoelectric conversion, thereby producing a device with remarkable ultraviolet detection capability and a relatively fast response. Other compounds such as 2D Ga_2Se_3 and Ga_2Te_3 have not been explored.

3. Group IV–VI

The advantages of this group were their low cost and earth abundance compared with those of TMD and other groups. In this group, binary materials are mainly in the forms of MX and MX_2 (M = Si, Ge, Sn, Pb; X = O, S, Se, Te). Their bulk materials have been studied extensively for photovoltaics and photoelectrochemistry.[94] However, the 2D morphology of this group has been studied only in the past decade, and considerable work

has been based on simulation. This indicates the substantial potential for further developments.[95] Moreover, the rich phase engineering of 2D materials in this group needs to be clarified.

3.1. Sn–X (SnS_2, $SnSe_2$, SnS, SnSe, SnTe)

Binary tin chalcogenide compounds including SnX, SnX_2, Sn_2X_3, and Sn_3X_4 can have different stoichiometric ratios. From among these, 2D materials with SnX_2 and SnX forms have been reported. The SnX_2 form is similar to a hexagonal MoS_2 structure. Here, metal atoms are sandwiched between two layers of chalcogenide atoms. Single-layer SnS_2 is a hexagonal structure with the Sn ion coordinated to six S ions in an octahedral cage. The different stacking of the single-layer produced several poly types such as 4H and rhombohedral (18 R).[96] The hexagonal SnX_2 phase can be transformed into tin monochalcogenide by creating X vacancies using many methods such as temperature enhancement,[97] plasma treatment,[98] and electron beam irradiation.[99] There are more polytypes for SnX. However, only orthorhombic (Pnma), rock salt (Fm3m), and zinc blende (ZB; F43m) phases have been reported in 2D SnX.[100–103]

3.1.1. SnS_2

The phase labels 2H and 1T for SnX_2 in the published papers are occasionally confusing. 2H SnS_2 is named using Ramsdell notation for sp-metal chalcogenides. It is the Pm1 space, with the Sn metal in the octahedral coordination by the S atom. However, this structure is the 1T phase for the labeling of 2D MoS_2, as shown in **Figure 4**.[104] Meanwhile, the Sn atom is the trigonal prismatic coordination in 1T SnS_2, whereas 2H is the label for MoS_2 with this structure. Therefore, a few papers have also assigned a 1T value to the actual 2H SnX_2.[105–107] In this review, we use 2H for labeling this CdI_2-type structure in which Sn cations occupy all the octahedral sites in chalcogen anion layers. This method has been used in earlier works.

A simulation shows that the 2H phase is the ground state for the monolayer of SnS_2 (note: the label of 1T phase is used in this paper).[107] Bilayer SnS_2 can be in AA stacking (Sn atoms are lined up on Sn atoms) or AB stacking (S atoms are lined up on Sn atoms). In general, AA stacking is favorable for the bilayer system. However, AB stacking can become more stable than AA stacking under charging or loading pressures. Moreover, bilayer SnS_2 can transform to a semimetal from a semiconductor with a perpendicular electric field.

Monolayer 2H SnS_2 can be prepared via mechanical exfoliation.[108] Bulk 2H SnS_2 is an indirect semiconductor. Reducing the thickness does not alter the nature of the indirect bandgap (demonstrated by the PL experiment).[108] However, the bandgap changes from 2.18 to 2.4 eV when the thickness decreases to a monolayer. With this method, Song et al. reported the first field-effect transistors of monolayer 2H SnS_2 with high carrier mobility (50 cm^2 V^{-1} s^{-1}) and high I_{on} /I_{off} ratio (>100).[109] However, the thickness of the monolayer SnS_2 was measured to be 1.8 nm in this study. This disagrees with other reports owing to the different scanning modes.[108] Calculations predicted that monolayer SnS_2 will have an ultralow lattice thermal
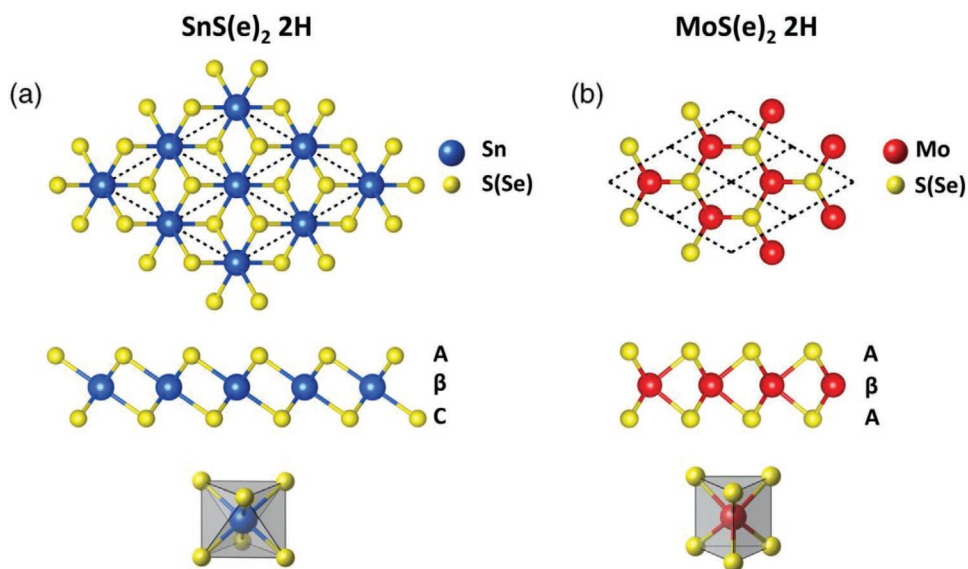
Figure 4. Atomic structure of a monolayer of a) SnS_2 ($SnSe_2$) and b) MoS_2 ($MoSe_2$), demonstrating the very different local atomic environments of the metallic atoms in the two compounds. a,b) Reproduced with permission.[105] Copyright 2016, American Physical Society.

conductivity and high carrier mobility. This indicates that monolayer 2H SnX_2 is a potential material for thermoelectric applications.[110] This observation was also predicted with multiple-layer SnS_2.[111] Herein, the power factor increased and thermal conductivity decreased as the thickness of the SnS_2 nanosheets decreased to approximately three layers, thereby achieving a high ZT value of 1.87.

There are many methods to prepare multiple-layer 2H SnS_2 for various applications. A thermosolvent was used to prepare multiple-layer SnS_2 (6–11 layers) for NO_2 gas sensors. It showed good selectivity and sensitivity (less than 30 ppb) owing to the good affinity of the NO_2 molecules toward SnS_2 surfaces and energy matching between the SnS_2 Fermi level and NO_2 molecular orbitals.[112] This method was also considered a straightforward and inexpensive approach for synthesizing large-scale SnS_2 nanoplates as anodes for Li-ion batteries.[113] These 2D SnS_2 nanoplates display superior physicochemical properties by shortening the Li-ion diffusion length and improving the electron transfer.[114] High-capacity, high-rate, and remarkably stable ion batteries were obtained by combining the SnS_2 nanosheets with conductive materials such as graphene[115] and conductive polymer (PANI).[116]

The hydrothermal treatment of tin foils also directly produced vertically aligned SnS_2 ultrathin nanosheet arrays. Such nanosheet arrays have wide applications as active materials for Li-ion batteries, catalysis, photoconduction, and field-emitting performance.[117] A vertical $Sn_{0.5}W_{0.5}S_2/SnS_2$ phase heterostructure was prepared using the hydrothermal method.[118] First, metallic $Sn_{0.5}W_{0.5}S_2$ nanosheets were prepared by alloying 2H-SnS_2 (1T in the paper) with 1T-WS_2. After deposition on SnS_2, charge carriers at the $Sn_{0.5}W_{0.5}S_2/SnS_2$ interface were rapidly transported for fast photodetectors. Recently, a gas sensor with suspended 2D SnS_2 of three layers was prepared through exfoliation. It showed high selectivity and ultrasensitivity for ammonia detection because of the rapid charge transport between ammonia molecules and these light active materials.[119]

CVD is the most popular method for preparing multiple-layer SnS_2. Large-size 2H SnS_2 (up to 150 μm) can be prepared with this method. Moreover, with this thickness, high-performance phototransistors,[120] and photodetectors[121] can be constructed. Their thickness and phases can be controlled[122] by growth parameters, and the photoresponse behavior is dependent on the thickness. When the substrate was modified with predefined seeds, a regular multiple-layer SnS_2 pattern deposited by the CVD method showed a short photocurrent response time of ≈5 μs.[123] The vertical growth of free-standing 2D SnS_2 nanosheets was also realized by this method for nonplanar photodetectors.[124] Recently, various shapes (hexagonal, triangular, windmill, dendritic, and coralloid) of SnS_2 nanosheets were prepared by controlling the growth conditions and substrate surfaces.[125] Importantly, selective phase growth of 2H or 1T was observed with the help of different salts. Herein, sodium halides favored the growth of the 2H phase, and potassium halides helped the growth of the 1T phase.

Other methods such as atomic layer deposition (ALD) at low temperatures and vapor transport have also been reported for synthesizing SnS_2 nanosheets with controllable thicknesses for photovoltaic cells and fiber lasers.[126] Recently, a scalable close-spaced sublimation method was developed to prepare vertically aligned 2H SnS_2 nanoflakes on transparent conductive substrates. The nanoflakes showed excellent optoelectronic and PEC properties.[127]

A new amorphous SnS_2 nanosheet was induced by doping with Zn/In through a hydrothermal method.[128] The amorphous layer increased the number of surface reaction sites with S vacancies and a gradient energy band. This promoted the oxygen evolution reaction (OER) dynamics and accelerated charge separation and transport, which eventually improved the PEC water splitting efficiency.

4H-SnS_2 nanosheets have also been reported as phototransistors for light detection.[108] Notably, Raman spectroscopy is a common method for characterizing layered SnS_2 (**Figure 5**).
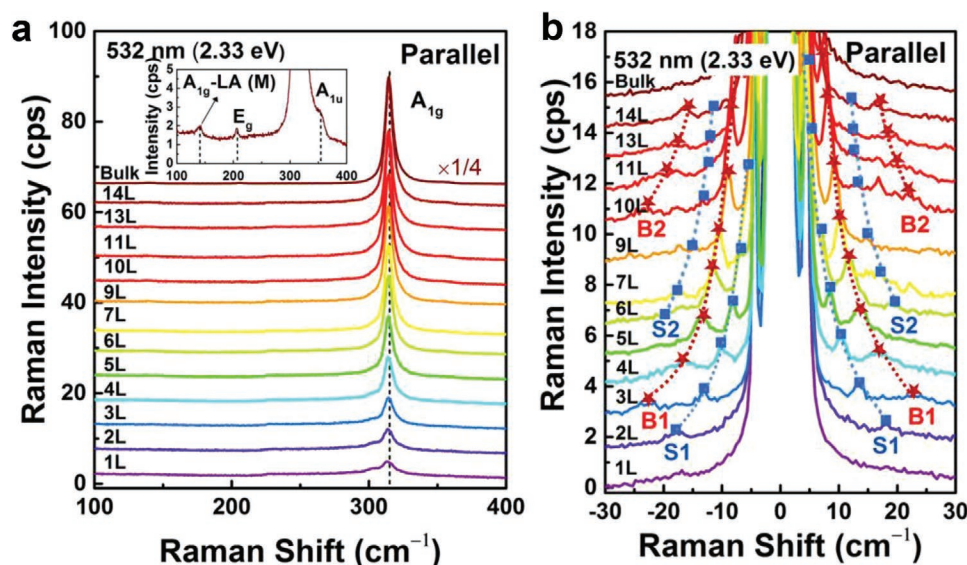
Figure 5. a) High-frequency modes and b) shear and breathing Raman modes of few-layer SnS_2 measured in parallel polarization. a,b) Reproduced with permission.[130] Copyright 2018, Springer Nature.

After exfoliation, the intensity of the Raman spectrum (peak at A1 + E mode) is proportional to the thickness. The E-mode can be used to discriminate the 2H (205 cm^{-1}) and 4H polytypes (200 and 214 cm^{-1}).[108] Sriv et al. comprehensively investigated the Raman spectrum in an intralayer (A1 and E) and interlayer modes.[129] The peak position of ≈314 cm^{-1} (A1 mode) did not change when the thickness of SnS_2 was tuned. However, the peak intensity decreased with as the thickness decreased, particularly from 1L to 3L. Moreover, the interlayer mode showed apparent peak shifts when the layer numbers were reduced. This is suitable for determining the thickness of SnS_2.

3.1.2. SnSe₂

Similar to SnS_2, $SnSe_2$ has been shown to have a hexagonal structure with a $SnSe_6$ octahedron, namely, 1T or 2H phase, in different studies.[104] 2H-phase $SnSe_2$ is the most stable phase and can be prepared by many methods. A low-pressure or low-temperature CVD technique was used to deposit few-layer $SnSe_2$ using a custom-prepared or low-melting-point precursor. This was because high temperatures decompose $SnSe_2$ into SnSe.[130,131] The CVD-prepared 2D $SnSe_2$ showed remarkable photodetector performance with high responsivity and a fast response.[131] Mechanically exfoliated mono- and few-layer 6H-SnSe₂ were characterized by Raman spectroscopy. The in-plane E_{1g} mode intensity was observed to be more suitable for layer number determination because this Raman mode intensity increases almost linearly with the number of layers.[132] However, the interlayer Raman modes E_g^2 and A_{1g}^2 are observed to be insensitive to temperature. Furthermore, studies on the effect of thickness on these Raman modes are few.[132] Similar to SnS_2, the characteristic of the indirect bandgap of $SnSe_2$ did not transform from bulk to monolayer. The bilayer $SnSe_2$ prepared by this method also displayed very fast photoresponsivity.[105] Recently, a simple ball-milling grind was used to prepare $SnSe_2$

nanoplates. Then, spark plasma sintering was used to press $SnSe_2$ nanoplates into pellets. During this process, preferential growth along the ab plane of the layered $SnSe_2$ structure was observed. These oriented pellets showed high thermoelectric performance.[133] Applying external pressure is an efficient method to improve the electrical conductivity of monolayer and bilayer $SnSe_2$ because of the variations in the Se–Sn antibonding states. This pressure-induced improvement in electrical conductivity enhanced the power factor for high thermoelectric performance.[134]

Phase-controlled synthesis of $SnSe_2$ and SnSe using a solution-based method has been reported.[135] During the solvothermal preparation, the addition of 1-dodecanethiol stabilized Sn^{4+}. This resulted in the formation of $SnSe_2$ rather than SnSe. Here, Sn^{4+} is typically reduced by oleylamine. SnSe and $SnSe_2$ nanosheets are potential candidates to replace the precious Pt metal as efficient catalysts in solar cells. Similarly, the phase-controlled synthesis of 2D $SnSe_2$, SeSe, or their mixture was realized by varying the concentration of the reducing agent, precursor ratio, and temperature.[136] As active materials for flexible, solid-state supercapacitors, pure $SnSe_2$ nanodiscs (168 Fg^{-1}) and SnSe nanosheets (228 Fg^{-1}) showed high capacitances, remarkable cycling stabilities, and good mechanical stabilities. These performance levels are comparable to or better than those of other reported materials. In addition, the rate capability of the $SnSe_2$ nanodiscs was significantly higher than that of the SnSe nanosheets. The thermosolvent process can also be used to prepare Cl-doped n-type $SnSe_2$ with a thickness of 3–5 nm.[137] Cl doping increases the n-type carrier concentration. This results in the enhancement of the power factor for thermoelectric devices. Furthermore, the thermal conductivity can be decreased to ≈0.67 W m^{-1} K^{-1} at room temperature because of phonon scattering in the layered anisotropic structure and nanoscale grain boundaries. The composites $SnSe_2$/rGO and $SnSe_2$/CNT prepared by the hydrothermal method showed a high rate performance as an anode for Li/Na-ion batteries.[138] This work also provided experimental and theoretical evidence

**ADVANCED
SCIENCE NEWS**

www.advancedsciencenews.com

**ADVANCED
FUNCTIONAL
MATERIALS**

www.afm-journal.de

for the mechanism of electrochemical sodium storage in $SnSe_2$. The electrochemical reaction was followed by X-ray diffraction (XRD) measurements. Herein, $SnSe_2$ underwent a hexanal crystal–amorphous–βSn + Na2Se-Na15Sn4 (orthorhombic) phase transformation. In addition, the reverse phase transformations during lithiation and delithiation were followed by in situ high-resolution transmission electron microscopy. The $SnSe_2$ nanoplate-graphene showed enhanced storage performances compared with pure $SnSe_2$ nanoplates or pure graphene.[139]

The superconductivity of $SnSe_2$ can be induced by pressure or using an electric double-layer transistor.[140] Electrical transport measurements and synchrotron XRD were used to characterize the metallization and superconductivity of pristine 1T-$SnSe_2$ under pressure. The results show that 1T-$SnSe_2$ was transformed from a semiconductor into a metal at 15.2 GPa and then, transited to a superconductor at 18.6 GPa. Under high pressure between 30.1 and 50.3 GPa, the superconductivity was robust with $T_c \approx 6.1$ K. High-pressure synchrotron XRD measurements established that there was no structural transition or phase decomposition of the $SnSe_2$ phase up to 46.0 GPa. A gate-induced interfacial superconductivity in 2D $SnSe_2$ demonstrated a superconducting transition temperature $T_c \approx 3.9$ K. The semiconductor–superconductor transition can also be realized in Li-intercalated 1T-$SnSe_2$, through electric field gating.[141] Here, the intercalated Li layer between the $SnSe_2$ layers provided electrons and increased the carrier density.

3.1.3. SnS, SnSe, SnTe

SnS has several polytype crystals. Its ground-state phase is *Pnma* (orthorhombic).[100] Ab initio molecular dynamics simulations showed that the metastable *Fm3m* phase (rock salt) can be thermodynamically stable at room temperature. However, the *Cmcm* phase (orthorhombic, high-temperature phase) can be stable only at high temperatures and can transit to the ground-state *Pnma* phase. This was demonstrated experimentally at 878 K. The *F43m*-phase (ZB) SnS was also predicted to be unstable thermodynamically and dynamically. Notably, the rock-salt phase of SnS was proposed to be misassigned as ZB in recent reports.[100] Similar to SnS, SnSe also has many polymorphs, namely, α, β, γ, δ, and ε. These polymorphs are indirect semiconductors, except for the ε phase. The calculated bandgaps (0.53, 2.32, 1.52, 1.56, and 1.76 eV for α-, β-, γ-, δ-, and ε-SnSe, respectively) of the various polymorphs of the SnSe monolayer overlapped within the visible spectrum. This indicated their potential for solar cell applications.[142]

The ground-state *Pnma*-phase 2D SnS is an indirect semiconductor regardless of its thickness.[103] Similar to SnS_2, the *Pnma*-phase 2D SnSb and the gap may be tuned by the layer thickness.[104,143] The liquid-phase exfoliation of commercial bulk SnS_2 can be used to prepare 2D SnS down to two layers with a thickness of ≈4 nm. When the thickness was reduced to two layers, the bandgap increased from ≈1.1 to ≈1.6 eV. Moreover, the bandgap of the monolayer was predicted to increase significantly to ≈2.5 eV.[103] The multiple-layer SnS prepared by this method also showed a remarkable nonlinear optical response.[144] The *Pnma*-phase SnS had a similar armchair

conformation with phosphorene and strong in-plane electronic anisotropy. The mobility difference along the zigzag and armchair directions can attain up to 1.7 times.[145] Their anisotropic electronic and optical properties are influenced substantially by strains. Application of in-plane compressive strains can reduce the bandgaps linearly, whereas tensile strains exert negligible impact.[146] However, unlike the unstable phosphorene, monolayer group-IV monochalcogenides can be super stable against oxidation in dry and humid conditions.[147]

The ground-state *Pnma*-phase SnS can also be prepared by removing S from SnS_2 by applying heat, plasma, and electron beam. High-energy electron irradiation using an electron beam[99] induced a progressive chalcogen loss to produce a mono- and dichalcogenide mixture, followed by a complete conversion to monochalcogenide. Irradiation conditions such as the electron exposure time and temperature may control the formation of SnX_2/SnX heterostructures. Furthermore, local electron irradiation can transform selected parts of a flake to monochalcogenides to form heterostructures. Elevated temperatures are favorable for the production of large-scale homogeneous high-quality ultrathin SnS (SnSe) during the electron irradiation processes for device applications. This process is similar to defect engineering in 2D materials using electron beams.[148] The structural transformation of SnX_2 was characterized by in situ luminescence.[149] Herein, S defects were introduced by electron beam irradiation, and the role of defects in the luminescence was examined by ab initio calculations. The phase transformation of SnS_2 to *Pnma* SnS by Ar plasma treatment was investigated recently.[98] An SnS–SnS_2 heterostructure was synthesized successfully by removing S atoms from the surface of SnS_2. As SnS is a p-type semiconductor and SnS_2 is an n-type semiconductor, a vertical p–n junction is formed for photocurrent generation under white light illumination.

A phase transition from hexagonal SnS_2 to orthorhombic SnS was also achieved by heating SnS_2 in Ar at 600 °C.[97] After annealing, the rGO/SnS composite showed a higher capacity for sodium-ion battery than rGO/SnS_2. Most importantly, this study indicated the phase transformation mechanism of SnS and SnS_2 during the charge and discharge processes. Thereby, it provided an approach to controlling the phases of SnS and SnS_2. Similarly, heating treatments can convert n-type $SnSe_2$ to p-type SnSe[150] and produce in-plane heterostructure p–n junctions at predefined locations.

There are two common methods to prepare 2D *Pnma* SnX directly: solution-based methods and vapor deposition. In organic solvents, monolayer *Pnma* SnSe with a lateral size of 300 nm was prepared by the thermosolvent method. The addition of the morphology control agent phenanthroline determined whether nanosheets or nanoflowers were formed. Their band structure and photoresponse properties were investigated further considering their substantial potential for optoelectronic applications.[151] Large *Pnma* SnS nanosheets were prepared by decomposing custom-made precursors. The as-prepared SnS showed a uniform morphology with a size of 7×3 μm and a thickness of 20 nm. These ultralarge, monodispersed SnS nanosheets exhibited noteworthy electrochemical properties including a capacity of 350 mAh g^{-1}.[152] Furthermore, the growth direction can be controlled by adjusting the capping agent usage to result in edge morphology anisotropy.[153] In

**ADVANCED
SCIENCE NEWS**

www.advancedsciencenews.com

**ADVANCED
FUNCTIONAL
MATERIALS**

www.afm-journal.de

other solvents such as water and EG, p-type, or Sn vacancy-engineered *Pnma*-phase SnSe/SnSn nanoplates were prepared without surfactant.[154] The nanostructures showed good electrical conductivity and high Seebeck coefficients, which resulted in high power factors.

In terms of vapor deposition, monodispersed square *Pnma* SnSe nanosheets with size controlled to 1–6 μm were prepared via vapor transport deposition. The thickness of the SnSe nanosheets varied from 6 to 40 nm. The 2D SnSe showed p-type conductivity and high photoresponsivity. This displays substantial potential for application in optoelectronics and energy harvesting.[155] *Pnma* SnS nanosheets prepared by CVD were also fabricated for high-performance photodetectors.[156] These experimental observations are in good agreement with theoretical calculations, which predicted that the 2D group-IV monochalcogenide MX would display an exceptional photoresponse and energy transfer efficiency with a visible spectrum because of the high efficiency of photoexcited electron–hole generation.[157] The *Pnma* phase of the SnS and SnSe flakes prepared by vapor deposition showed a temperature-dependent Raman response.[158,159] The A_g modes and B_{3g} peaks were linearly red-shifted as the temperature increased from 98 to 298 K. The SnSe nanoflake had a larger temperature coefficient than other 2D materials such as MoS_2, black phosphorus, and graphene.[158] Angle-dependent Raman spectroscopy characterized the in-plane anisotropy of the *Pnma* SnS nanosheets.[159] Furthermore, in-plane ferroelectricity was also observed in FET devices fabricated on ultrathin SnS films.[160] Notably, the polarization was also affected by whether the number of layers was odd or even, indicating that inversion symmetry plays an important role in this property. Recently, the vapor–liquid–solid (VLS) process was used to prepare SnS nanosheets with thickness controllable by the size of the gold seeds. The stability of the SnS nanosheets at high temperatures was studied using in situ TEM. Faster decomposition was observed along the [100] direction.[161]

The phase transition from *Pnma* to *Cmcm* is a two-step process. This is considered the main factor contributing to the high ZT of SnSe.[162] This phase transition was experimentally observed above 600 K. The two conduction bands' divergence and convergence were calculated. These optimized the Seebeck coefficient and carrier mobility, thereby resulting in an exceptional power factor. The maximum ZT (ZTmax) of ≈2.8 was achieved at 773 K after combination with a low thermal conductivity along the out-of-plane direction.[8]

However, there are no reports of 2D *Cmcm*-phase SnX because its instability. Nonetheless, the *Cmcm* structure was observed at low temperatures during the preparation of SnSe nanoparticles by the thermosolvent method. Further reaction at high temperature produced *Pnma*-phase SnSe.[12] This work provides important information for synthesizing another 2D *Cmcm*-phase SnX that is dynamically stable.[12]
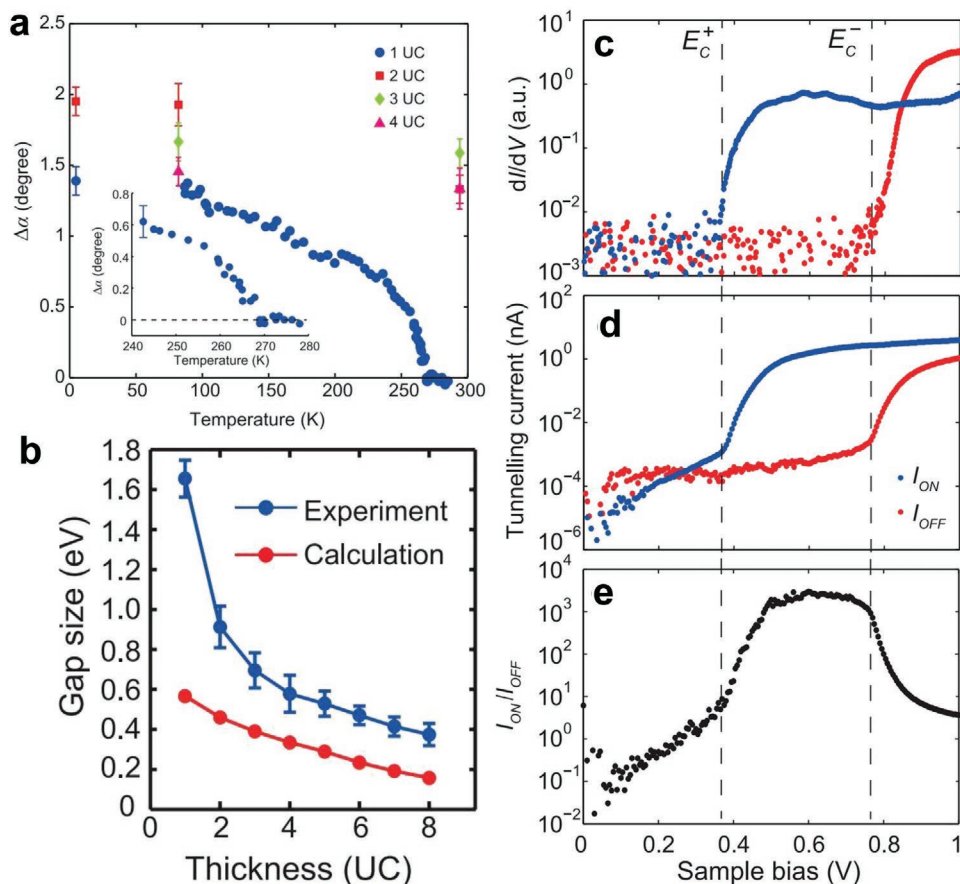
Cubic SnX can be in the *Fm3m* (rock salt) and *F43m* phases (ZB). Although the ZB phase was predicted to be unstable, the successful preparation of this phase was demonstrated by the intensity ratio of the peaks of (111) and (002). XRD pattern monitoring of this XRD peak intensity ratio is important to distinguish the two phases.[100] The colloidal synthesis of nano- and microcrystal particles at mild temperatures (thermosolvent,

150 °C) has successfully produced ZB SnS. However, the further reaction at 250 °C converted the ZB phase to the orthorhombic phase (*Pnma*).[163] The formation of an intermediate product of the mixture of ZB and orthorhombic phases during the preparation of 2D SnS by the thermosolvent method was verified by XRD characterization. After 30 min of annealing at 330 °C, the product consisted only of orthorhombic SnS nanoribbons. This indicates the transition from the metastable ZB phase to the stable orthorhombic phase.[164] The growth mechanism of 2D SnS nanosheets and the effect of ligands on the shape, size, thickness, and crystal structures were reported recently.[165] A similar phenomenon during the preparation of SnS films by the CVD method was also reported. Here, a tin thioureide complex was used as a precursor to produce SnS films with a controllable phase. Metastable ZB-SnS was prepared at low temperatures (below 300 °C) and characterized as a photovoltaic device. When the temperature was above 350 °C, orthorhombic α-SnS was present.[101]

Bulk SnTe has a rock-salt structure at room temperature. Furthermore, it is a p-type semiconductor with a narrow bandgap (≈0.2 eV).[166] A phase transition from cubic to rhombohedral occurs at the ferroelectric transition temperature Tc. The Tc for bulk SnTe is ≈100 K. The decrease in Sn vacancies increased the Curie temperature. In the layered SnTe, the Sn vacancies were suppressed substantially, and the defect density was significantly lower than that of the bulk material. This caused T_c to be 270 K (**Figure 6**a). A further study showed that the defect density of two- to four-layer SnTe is lower than that of a monolayer SnTe. Thus, a higher T_c was observed, which enabled the robust ferroelectricity of these layered SnTe at room temperature.[167] The ferroelectricity of 2D SnTe was characterized by scanning tunneling microscopy (STM) and scanning tunneling spectroscopy. SnTe nanosheets of different thicknesses were prepared on graphitized 6H-SiC(0001) substrates using a molecular beam epitaxial technique. The bandgap of SnTe can be increased from 0.2 to 1.6 eV when it is broken down to a monolayer. This is owing to quantum confinement (Figure 6b). Because of its high T_c, a three-layer SnTe was used to fabricate a nonvolatile ferroelectric random-access memory device. The threshold voltage and tunneling current were measured by STM, and the reading/writing process was recorded in two opposite directions of polarization. As a result, a high on/off ratio of 3000 was obtained with a bias voltage between 0.5 and 0.7 V (Figure 6c–e). However, the performance of the monolayer SnTe showed a low on/off ratio.

Similar ferroelectricity and phase transitions were predicted also in other monolayer group-IV monochalcogenides, via simulation.[15] The in-plane spontaneous polarization in these monochalcogenides was calculated. Their robust ferroelectricity and high Curie temperatures make them potential materials for ultrathin ferroelectric applications. Furthermore, T_c can be controlled over a wide range by strain.[168] The calculation results also helped predict that monolayer group-IV monochalcogenides would have piezoelectric properties that would be significantly better than those of most of the other piezoelectric materials. Their large piezoelectricity would enable the fabrication of electronic and piezotronic devices such as nanoscale sensors and controllers.[169]

**ADVANCED
SCIENCE NEWS**

www.advancedsciencenews.com

**ADVANCED
FUNCTIONAL
MATERIALS**

www.afm-journal.de

Figure 6. a) Temperature dependence of the distortion angle for the 1- to 4-unit cell (UC) SnTe films. (Inset a) The distortion angle near $T_c = 270$ K for the 1-UC film exhibiting the behavior of a second-order phase transition. b) Experimentally measured and DFT-calculated thickness dependence of the electronic band gap. c) Threshold voltages measured by STM (for a 3-UC film). d) Simulation of the reading process by STM in a 3-UC film. e) Dependence of the on/off ratio for a 3-UC film. a–e) Reproduced with permission.[168] Copyright 2016, American Association for the Advancement of Science.

3.2. Ge–X (GeS, GeSe, GeTe, GeS$_2$, GeSe$_2$)

3.2.1. GeS, GeSe, GeTe

In general, GeS and GeSe adopt orthorhombic structures (space group of *Pnma*) that are analogous to that of black phosphorus. This phase is stable and shows a chair conformation with high carrier mobility.[170] Recently, a new phase, namely, β-GeSe, was prepared.[171] The properties of monolayer β-GeSe were determined to be suitable for future optoelectronic applications.[172] The structure of α-GeSe and black phosphorus has six rings with a chair conformation, whereas that of β-GeSe has six rings with a boat conformation. β-GeSe was synthesized at high pressures and temperatures and was stable at room temperature because of a marginal decrease in the distance between the layers.[171]

Similar to GeSe, the β-GeTe phase was also predicted to have a boat conformation under high pressures[173] that is attained through a structural phase transition in the order $R3m$–$Fm\bar{3}m$–$Pnma$-boat–$P4/nmm$ with increasing pressure. In another study, the stability of GeTe in rhombohedral ($R3m$), face-centered cubic ($Fm3m$), and simple cubic ($Pm3m$) phases were investigated using the density functional theory (DFT).

The rhombohedral phase of GeTe can be dynamically stable at 0 GPa, whereas the $Fm3m$ and $Pm3m$ phases can be stable only at 3.1 and 33 GPa, respectively.[174] The cubic phase can also be realized by alloying GeTe with MnTe. In this phase, the rhombohedral-to-cubic phase transition temperature of GeTe shifts from 700 K to room temperature. The materials had an ultralow thermal conductivity, which enhanced ZT to 1.61 at 823 K with an optimized high hole carrier concentration.[16]

Unlike indirect 2D SnSe, single-layer and double-layer GeSe have direct bandgaps. The electrical properties of the GeSe monolayer are anisotropic and strain-sensitive.[175] The characteristic of the bandgap can be direct or indirect and controlled by uniaxial and biaxial strains. The bandgap energy can be tuned in a large range by marginal strains.[176] In another work, α-GeSe with different thicknesses was prepared by combining mechanical exfoliation and controllable laser irradiation in a high vacuum.[177] The critical thickness when the number of layers (N) is three was verified for the indirect-to-direct bandgap transition, which was established by experimental PL measurements and first-principle calculations.

Multiple-layer orthorhombic GeS nanosheets were prepared by mechanical exfoliation.[178] Optical properties such as PL and Raman spectra depend strongly on polarization. The PL

**ADVANCED
SCIENCE NEWS**
www.advancedsciencenews.com

**ADVANCED
FUNCTIONAL
MATERIALS**
www.afm-journal.de

intensity also shows a thickness-dependent behavior owing to surface defects.[179] When the exfoliation was performed in the liquid phase with the aid of tip ultrasonication, anhydrous NMP was observed to be the best solvent for preparing multiple-layer GeS nanosheets with different sizes and thicknesses.[180] The GeS nanosheets were observed to be stable at room temperature and showed remarkable electrochemical performance as an anode for Li-ion batteries.

Similar to GeS, few-layer α-GeSe nanosheets prepared by liquid-phase exfoliation were observed to be stable in ambient environments.[181] A blue shift in the signature Raman mode was observed when the GeSe thickness decreased owing to the reduction in the dielectric screening effect. The bandgap increased from 1.08 eV (bulk GeSe) to 1.53 eV (few-layer GeSe) because of the quantum confinement effect. Devices based on these materials show a fast photoresponse, which indicates the material's potential for optoelectronic applications. Orientation-dependent Raman spectroscopy was used to explore the anisotropy of the α-GeSe nanosheets prepared via exfoliation.[182–184] When the polarization of the incident laser is parallel to the armchair direction of GeSe, the peak at 188 cm^{-1} (Ag mode) attains the maximum intensity. The GeSe nanoflakes also showed anisotropic absorption spectra (400–950 nm). Polarization-sensitive photodetectors were fabricated based on this. A remarkable dichroic ratio of 2.16 was obtained with an optimized wavelength of 808 nm.[182] Other optical anisotropies of GeSe, such as reflection, extinction, and refraction, have also been studied recently.[185] As a common solution-based method, a thermosolvent was also used to prepare orthorhombic(α) single-crystal GeS (3–20 nm), GeSe (5–100 nm), and GeTe nanosheets (5–5.13 nm)[186] by slowing the growth along the polar axis.[187] Unexpectedly, although α-GeS nanosheets have been commonly prepared by vapor deposition (e.g., CVD and PVD),[188] it was the last method applied to prepare α-GeSe

nanosheets.[184,189] The as-prepared GeSe nanosheets had a rectangular shape because of the [010] growth direction. The phototransistors based on these nanosheets presented remarkable optoelectronic properties.

First-principle simulation results indicate that 2D group-IV tellurides are potential ferroelectric materials.[190] Considering GeTe as an example, 2D GeTe prefers an orthorhombic phase with an in-plane spontaneous polarization. The vertical electric field can tune the in-plane coercive field for reversing the polarization. Furthermore, the application of a tensile strain can increase the Curie temperature T_C of monolayer GeTe and improve the ferroelectric performance. The tunable ferroelectricity and anisotropic electric properties of monolayer β-GeSe have been reported in another work also.[17] Here, the Curie temperature of monolayer β-GeSe was estimated to be 212 K. It can be increased further above room temperature by applying a tensile strain of ≈1%.

The phase changes between amorphous and crystalline GeTe can be used as memory cells.[191] In this work, 2D GeTe with a thickness of 20 nm was deposited via magnetron sputtering. The heater size used to control the amorphous region was very small (20–60 nm), which resulted in fast recrystallization in a small switchable volume. The set pulse of this GeTe-based phase change memory can be reduced to 1 ns under optimized conditions.

Recently, a new 2D phase was reported in Ge$_4$Se$_3$Te. As shown in **Figure 7**, this new X–Ge–Ge–X structure appears to be flipping every second sheet of α-GeTe or shifting a half layer of GaSe and then, stacking it by van der Waals interactions. When adapted with the GeTe structure, a Ge atom is in a distorted octahedron formed with Te atoms and another Ge atom. This generates a new structure, which is also related to GeSe. Because the stacking sequences determine the polymorphs of GeSe, it is likely that this new structure is of similar rich
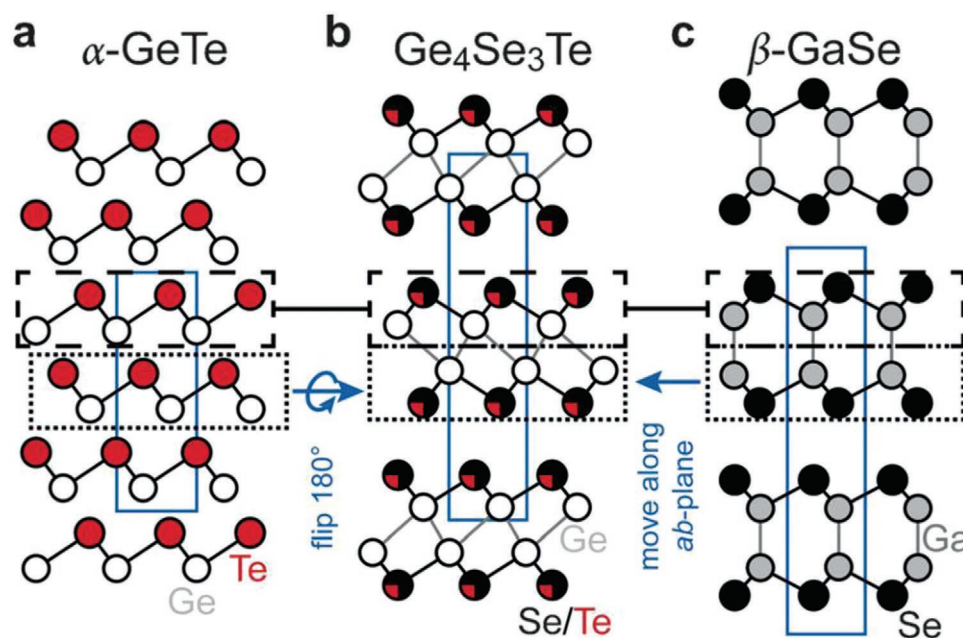
Figure 7. Comparison of the b) Ge$_4$Se$_3$Te crystal structure with the related structures of a) α-GeTe and c) β-GaSe. Structure of Ge$_4$Se$_3$Te as a result of flipping every second sheet of α-GeTe or shifting half layer of GaSe. a–c) Reproduced with permission.[193] Copyright 2017, Wiley-VCH.

**ADVANCED
SCIENCE NEWS**

www.advancedsciencenews.com

**ADVANCED
FUNCTIONAL
MATERIALS**

www.afm-journal.de

polymorphs. The unexpected and significantly stronger Ge–Ge contact is also in the structure. This can be explained by the lowering of the energy by the reshuffling of electrons from antibonding Ge–Te into bonding Ge–Ge contacts.[192]

3.2.2. GeS₂, GeSe₂

The structural unit of GeSe₂ is tetrahedra Ge(Se$_{1/2}$)4. This enables the formation of many porous and amorphous structures through the sharing of the corner units.[193] The difference between GeSe₂ and SiO₂ is the presence of edge-sharing polyhedral in the former, which increases the coordination number. The regular arrangement of the tetrahedral units can produce many crystalline structures including orthorhombic α-GeSe₂, monoclinic β-GeSe₂, hexagonal γ-GeSe₂, and tetragonal ($P4_2/nmc$, $I2d$, I, and P) phases. A new porous-phase δ-GeSe₂ also showed very low energy, and 2D mesoporous δ-phase GeX₂ superstructures (S, Se) were obtained with an organic template-directed growth at high temperatures.[194] The semiconductor β-GeSe₂ is the most stable phase and can transit to metallic γ-GeSe₂ through an increase in the pressure.[195] There are several methods to prepare 2D β-phase GeSe₂, including mechanical exfoliation,[196] CVD,[197,198] and CVT.[199] Most of the 2D GeSe₂ produced by these methods are composed of multiple layers and are stable under ambient conditions. These multiple-layer GeSe₂ nanosheets have a wide bandgap of 2.74 eV. Recently, monolayer β-GeSe₂ with a direct bandgap of 2.96 eV was reported.[200] β-phase GeS₂ and GeSe₂ nanosheets exhibit structural, vibrational, electrical, and optical anisotropies. Hence, they are suitable for designing high-performance photodetectors.[196,200,201] The 2D β-phase GeSe₂ can be transformed into α-GeSe₂ through irradiation with high intensity laser.[198] Other phases (such as the γ phase) in 2D form have not been reported, although bulk γ GeSe₂ has been obtained at high pressure.

Studies explaining 2D SnTe₂ and GeTe₂ are few. This is possibly owing to their instability while decomposing into Te and GeTe crystallites.[202] These 2D structures can exist only when tensile strain is introduced to stabilize the dynamical properties of the lattice.[203] An alternative approach to stabilizing the GeTe₂ monolayer, by inducing distortions with hydrogenation, was also proposed.[203]

3.3. Pb–X (PbS, PbSe)

Bulk PbS is a semiconductor with a direct bandgap of 0.41 eV. The most stable phase of PbS is the rock-salt structure. The pressure for the transition from the rock-salt phase to the orthorhombic phase ($Cmcm$) was observed to be ≈3 GPa. This transit pressure increases with an increase in temperature until 573 K. Beyond this, only the cubic phase exists regardless of the pressure.[204]

Rock-salt 2D PbS is generally prepared using solution-based methods. One method is based on oriented assembly. Herein, PbS nanoparticles or nanowires are attached to each other in a controlled manner with the assistance of capping agents.[205] Another method is the well-known thermosolvent method. Klinke et al. grew 2D PbS using various surface capping ligands[206]

and controlled the thickness from 4 to 20 nm by adjusting the amount of capping ligands.[207] In the preparation, shape control from particles to stripes and then to sheets was realized by tuning the usage of sulfide and chloroalkane.[208] These rock-salt PbS nanosheets showed high performance in FET applications, which can be either n- or p-type depending on the surface defects introduced.[209] Recently, this group also reported the spintronics of rock-salt PbS with an unusual selection mechanism of carrier excitation, which can be tuned by the gate voltage and thickness of the materials.[210] Apparent quantum confinement was observed when the thickness of PbS was reduced from 6 to 2 nm. This was demonstrated by the resulting PL and optical absorption.[211] Furthermore, the combination of the quantum confinement of two directions in rock-salt PbS nanoribbons improved the quantum yield. Thereby, photoluminescence quantum yield of over 30% was achieved in the infrared spectrum.[212] In another work, acetic acid produced from precursors was observed to hinder the reproducibility of PbS nanosheet formation. Rock-salt PbS and PbS/CdS nanosheets were prepared down to 2 nm using acetate-free precursors.[213]

Recently, PbS nanoplatelets in another phase and with an orthorhombic crystal structure were prepared using the thermosolvent decomposition method. A blue shift was observed in the absorption spectrum because of the thickness of 1.8–2.8 nm. The lateral size can be controlled by varying the reaction temperature, growth time, and capping ligands.[214] It is noteworthy that free-standing ultrathin 2D PbS nanocrystals prepared using the same method were assigned to the rock-salt phase in another work.[215] A comparison of the XRD results revealed that the crystal phase is more likely to be an orthorhombic phase. This material exhibits efficient and highly stable dielectric properties. The orthorhombic phase of ultrathin 2D PbS was verified further recently in a study where Pb(SCN)2 was used as the only precursor for thermosolvent decomposition. This may result in the preparation of 2D metal chalcogenides using other metal thiocyanate precursors.[216]

With respect to 2D PbSe, only the rock-salt phase was reported.[217] Similar to PbS, a solution-based method was used to prepare 2D PbSe with a controllable thickness from 2 to 6 nm. Furthermore, the thickness dependency of the bandgap was also observed by PL measurements. During the preparation, Pb–Cl–Pb bridges were observed to stabilize the 2D network by connecting neighboring PbSe QDs along (100) surfaces. A new strategy for cation exchange was recently developed, in which Pb^{2+} replaced Cd^{2+} in the CdSe nanoplates. This produced PbSe nanoplatelets with different thicknesses from three to six monolayers.[218]

3.4. Si–X (SiS, SiSe, SiTe)

All the reported 2D SiX materials are based on theoretical predictions. DFT calculations predicted the equally stable and indirect bandgap α-phase (orthorhombic) and β-phase (hexagonal) SiS monolayers.[219] The bandgaps with both the phases can be tuned by an in-layer strain. Because the SiS monolayers have a structure similar to that of phosphene, they can form a heterostructure with phosphene in the lateral and vertical directions. This enriches the structural and electronic properties. In

**ADVANCED
SCIENCE NEWS**

www.advancedsciencenews.com

**ADVANCED
FUNCTIONAL
MATERIALS**

www.afm-journal.de

addition to the α and β phases, 2D $Pma2$-SiS and metastable silicene sulfide were also predicted. These were observed to be more stable than α-SiS and β-SiS.[220] 2D $Pma2$-SiS exhibited good air stability. Moreover, the $Pma2$-phase SiS showed a direct semiconducting characteristic with good electronic and optoelectronic properties. Furthermore, the bandgap can be tuned by layer thickness or strain. Silicene sulfide has a $Cmmm$ symmetry and exhibits properties similar to those of 2D $Pma2$-SiS. Both of these are potential candidates for various optoelectronic and electronic applications because of their high light absorption, high carrier mobility, strong optical and electronic anisotropies, and good ambient environment stability.[220] However, another study showed that the ground state of SiS and SiSe monolayers exhibited $Pmma$ symmetry (orthorhombic). Moreover, they were observed to be stable up to 1000 K.[221] As nontoxic and earth-abundant elements, SiS and SiSe have been predicted to be potential thermoelectric materials with low thermal conductivity and high power factors.[221] These orthorhombic SiS and SiSe monolayers have also been predicted to be good candidates as anode materials for Li-ion batteries with theoretical specific capacities of 445.7 mAh g^{-1} for the SiS monolayer and 250.44 mAh g^{-1} for the SiSe monolayer.[222] The orthorhombic 2D SiSe monolayer can exhibit metal, indirect band, and direct bandgaps under different ranges of in-plane strain.[223]

There are two phases of SiTe monolayers: α (orthorhombic, $P3m1$) and β (trigonal). [224] The α-SiTe monolayer is stable in energy and is an indirect semiconductor. It can be transformed to a metal or direct semiconductor under applied strain. The β-SiTe monolayer shows only an indirect bandgap under strain. 2D β-SiTe was predicted to have a very high Seebeck coefficient of 2060 μV K^{-1} owing to the sharp DOS peak near the valence band edge. By combining the low thermal conductivity, 2D β-SiTe showed its potential as a high-temperature thermoelectric material with n- and p-type doping.[225] With a Si:Te stoichiometric ratio of 2:3, trigonal structure (P1c) Si$_2$Te$_3$ is a stable phase and is predicted to exhibit a high thermoelectric performance at high temperatures (1000 K).[226] It can be prepared by the vapor transfer process or VLS process with a vapor Te source and Si supplied from either powder or a substrate.[227,228] Many cations such as Li, Mg, Ge, and Cu can intercalate into the layer. This makes 2D Si$_2$Te$_3$ a potential chemically tunable platform for full-spectrum optical properties for optoelectronic applications.[229] 2D Si$_2$Te$_3$ undergoes a semiconductor-to-metal phase transition at ≈9.5 GPa, which can be further reduced to ≈7.5 GPa after Mg intercalation.[228]

DFT calculations indicated that covalency plays a more important role in small cation monochalcogenides such as SiX and GeX, and that the orthorhombic ($Pma2$) phase is favored.[230] In large cation monochalcogenides such as SnX and PdX, the Coulomb interaction becomes more important, thereby resulting in a distorted NaCl-type structure. This conclusion is in good agreement with those of other reports mentioned in the above summary. Moreover, group-IV monochalcogenide monolayers were predicted to be photostrictive (illumination-induced nonthermal strain) based on a converse piezoelectric effect in the photoexcited electronic states.[231]

Other phases such as 1T, bitetrahedral, and monoclinic 2D structures were predicted for group-IV dioxides MO$_2$ (SiO$_2$, GeO$_2$, SnO$_2$, and PbO$_2$). Furthermore, their formation energy, electronic properties, and potential applications were proposed.[232] Bitetrahedral SiO$_2$, monoclinic GeO$_2$, 1T SnO$_2$, and PbO$_2$ were stable, and only bitetrahedral SiO$_2$ had a direct bandgap. The bitetrahedral SiO$_2$ could function as a gate oxide for monolayer MoS$_2$ and phosphorene because of its suitable band offset (above 1 eV).

4. Group V–VI: Sb, Bi

In this family, 2D materials of the form M$_2$X$_3$ (mainly the compounds of M = Sb, Bi, and X = O, S, Se, Te) have been studied extensively. These 2D materials exhibit a strong QSH effect. Hence, research attention on these has increased significantly over the past few years. In particular, the QSH phase is a time-reversal invariant electronic state with a bulk electronic bandgap. It supports the charge and spin transport in gapless edge states.[233] In the QSH state, the bulk of the 2D electron system is insulating, and the edge states are helical. Each edge consists of forward-moving and backward-moving states with different spins. **Figure 8** demonstrates the fundamental concept of the QSH effect. The QSH state exists in nonmagnetic materials and also in the absence of an external magnetic field. This state is mainly associated with a Z$_2$ topological invariant, which differentiates it from an ordinary insulator.[233] Hence, QSH effects in materials cause their edge states to be topologically protected from back scattering. An extensive understanding of the QSH effect is required considering the future applications
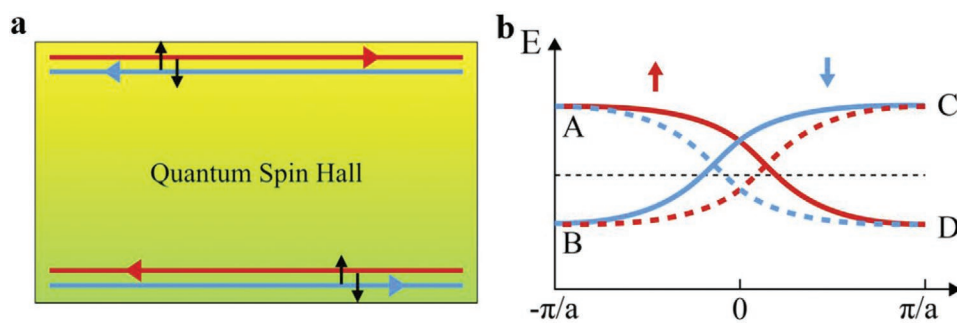
Figure 8. a) Sketch of the quantum spin Hall edge states. The red and blue lines are edge states. The arrows along the lines indicate the carriers' moving direction in such edge states. Here, the bulk is insulating, and the edge states are helical. Each edge contains both forward moving and backward moving edge states with different spins. b) Schematic band structure of the quantum spin Hall edges. Solid and dashed lines represent the top and bottom edges, respectively. a,b) Reproduced with permission.[235] Copyright 2015, Wiley-VCH.

**ADVANCED
SCIENCE NEWS**
www.advancedsciencenews.com

**ADVANCED
FUNCTIONAL
MATERIALS**
www.afm-journal.de

of topological quantum computing. First-principles calculations combined with photoemission spectroscopy have recently demonstrated the Z_2 topological properties of Bi_2Te_3 and Sb_2Te_3 and their derivatives.[18] However, specific theoretical and experimental studies for determining the various protected topological phases, phase transitions, and QSH effects of 2D materials belonging to the group V–VI family are still insufficient.

There are a few more theoretical approaches for the fundamental study of QSH phases in 2D materials. Tensor-entanglement-filtering renormalization is one of the most important approaches, where the symmetry group of the Lagrangian, that is, a fixed-point tensor, T_{inv} and G_{sym} can define the symmetry-breaking and topological phases illustrated by the 2D statistical Ising model, loop-gas model, and 1 + 1D quantum spin −1/2 and spin −1 models.[234] Such a (G_{sym}, T_{inv}) characterization has shown that the Haldane phase with a spin −1 chain is a topologically protected phase by the time-reversal, parity, and translation symmetries.[234] Pollmann et al. further studied the stability of the Haldane phase in integer-spin chains and found that the odd-S Haldane phase is a topologically protected nontrivial phase by any of the dihedral groups of π rotation, time-reversal, and link inversion symmetries.[235] Moreover, the Wess–Zumino–Witten model for Lie symmetry groups can be employed to determine the 2D interacting spin system with nontrivial Z_2 symmetry-protected topological order.[236] This model can potentially lead to a classification of symmetry-protected topological orders in interacting boson and fermion systems of any dimension. By considering these models as the motivational remarks, recent studies have been directed much specifically toward the determining of various protected topological phases, phase transitions, and QSH effects of a large family of 2D materials belonging to the group V–VI. This section focuses mainly on the progress in the determination of the stable topological phases and the phase-dependent scientific achievements with regard to the following individual compounds.

4.1. Bi–X (Bi_2O_3, Bi_2S_3, Bi_2Se_3, Bi_2Te_3)

4.1.1. Bi_2O_3

Bulk Bi_2O_3 exhibits many phases, including α, β, γ, δ, and ε, whereas 2D Bi_2O_3 shows α, β, γ, and δ phases.[237] The α (monoclinic) phase of Bi_2O_3 is the most stable phase, and its β (tetragonal) and γ (cubic, bcc) phases are metastable.[238] The growth of α-Bi_2O_3 ultrathin films has been achieved using ALD.[238] The α-Bi_2O_3 films synthesized by ALD can be transformed completely into γ-Bi_2O_3 at temperatures above 700 °C. It is noteworthy that the metastable γ phase can persist at room temperature. In a solution-based method, α-Bi_2O_3 is generally grown into a needle shape without using a template.[239] α-Bi_2O_3 nanosheets with a thickness of 10–20 nm were synthesized successfully using graphene oxide as a template. Moreover, α-Bi_2O_3 exhibits remarkable photocatalytic activity and durability in the photodegradation of methyl orange by visible light irradiation.[240] Recently, α-Bi_2O_3 monolayers have also been prepared from elemental liquid bismuth via a facile and scalable method.[241] Here, α-Bi_2O_3 nanosheets were exfoliated from the surface of liquid bismuth. In this method, the thickness of

similar nanosheets can also be controlled by the oxygen concentration during the exfoliation process. Compared with the bulk Bi_2O_3 with a bandgap of ≈2 eV, the monolayer α-Bi_2O_3 shows n-type semiconducting behavior and a direct bandgap of ≈3.5 eV. A photodetector device fabricated with this material exhibited ultrahigh UV responsivity and an inferred detectivity.

β-Bi_2O_3 single crystalline nanosheets can be prepared by the solvothermal method using alcohol as a solvent and calcination at a mild temperature (300–400 °C). The β phase of Bi_2O_3 has been observed to consist of many rectangular pores in the nanosheets with exposed reactive (001) facets. Moreover, the β phase of Bi_2O_3 exhibits potential for enhanced photocatalytic performance compared with α-Bi_2O_3.[242] Ionic doping into β-Bi_2O_3 nanosheets, i.e., 0.8 wt% Er^{3+} doping, can significantly improve the photocatalytic activity owing to the upconversion effect. Another straightforward technique for the calcination of bismuth precursor absorbed on FTO glass slides has also been demonstrated to be capable of synthesizing β-Bi_2O_3 nanoplates. Wang et al. introduced a calcination method for the formation of β-Bi_2O_3 nanoplates consisting of many nanopores, which were obtained after the calcination of a bismuth precursor at 350 °C.[243] However, the thickness of these nanoplates was significantly large (≈100 nm). A small size can be achieved by controlling the absorption of the precursor. In addition to the transition of α-Bi_2O_3 into γ-Bi_2O_3 nanosheets at high temperature, cubic γ-Bi_2O_3 nanosheets can also be grown on a carbon paper through a combination of hydrothermal and calcination methods.[244] Vertically aligned γ-Bi_2O_3 nanosheets on carbon paper showed a high capacity and remarkable capacity retention of 71.4% after 5000 cycles as an anode material in aqueous alkaline batteries.

Recently, ultrathin δ-Bi_2O_3 (≈3 nm) was prepared successfully on carbon cloth by the solvothermal method.[245] This material displayed a remarkable energy density as a supercapacitor with the help of poly(3,4-ethylenedioxythiophene) coating. This is because of the vertical and interconnected network architecture along the carbon cloth fiber, which provides a large surface area for the electrolyte. Furthermore, this material is flexible and suitable for designing other high-performance electrodes.[245]

4.1.2. Bi_2S_3

Thus far, all the reports on 2D Bi_2S_3 have shown its orthorhombic phases. However, the existence of a stable hexagonal phase at high pressures has also been predicted.[246] Orthorhombic Bi_2S_3 nanosheets were first synthesized by decomposing $Bi(S_2CNEt_2)_3$. During this process, the Bi_2S_3 nanorods were first formed and then underwent an attachment–recrystallization growth mechanism.[247] Chen et al. prepared Bi_2S_3 nanosheets down to 2.2 nm (2 layers) through a facile ethanol solvothermal process.[248] They observed that the crystalline orthorhombic phase can be developed effectively by increasing the reaction time. Furthermore, they fabricated a flexible photodetector device with the orthorhombic phase of 2D Bi_2S_3. This device showed a high responsivity and fast response in the visible–near-infrared light range. Subsequently, a solvothermal and stirring-assisted reductive exfoliation method was introduced to obtain a similar phase of 2D Bi_2S_3 with controllable thickness. The 2D Bi_2S_3 was observed

**ADVANCED
SCIENCE NEWS**
www.advancedsciencenews.com

**ADVANCED
FUNCTIONAL
MATERIALS**
www.afm-journal.de

to be highly suitable for use in high-performance photodetectors under ambient conditions and gas sensors.[249] Recently, it was observed that the sulfurization of Bi_2O_3 nanosheets can also directly produce orthorhombic Bi2S3 or their Bi_2O_3–Bi_2S_3 heterostructures. This heterostructure showed an improved capability for sodium storage compared with pure Bi_2S_3 and Bi_2O_3, owing to the enhanced charge transfer in the heterostructures.[250] With regard to the topological phase, a compressive pressure of ≈5.3 GPa can transform the stable layered phase of Bi_2S_3 into a topological insulator phase. Such a topological phase transition in the layered Bi_2S_3 was verified by the calculated band inversion, Z2 invariant numbers, and gapless surface states.[246] Moreover, the application of pressure can effectively enhance the strength of the spin–orbit interaction in Bi_2S_3, thereby causing an increased bandgap.[246]

4.1.3. Bi_2Se_3

Nielsen et al. first reported pressure-induced phase transitions in ordered and disordered Bi_2Te_2Se.[251] This study showed the phase transition of Bi_2Te_3 and Bi_2Se_3 from α to β and then to γ/δ as the pressure increased. Freestanding monolayer rhombohedral Bi_2Se_3 was prepared using the scalable interaction/exfoliation strategy. It showed an enhanced performance in harvesting thermoelectric energy. In particular, the surface distortion on similar free-standing Bi_2Se_3 caused an increase in the electrical conductivity and Seebeck coefficient, effective phonon scattering caused a decrease in thermal conductivity,

and finally, the entire process resulted in the enhancement of the thermal energy harvesting potential. An eight-fold higher ZT was achieved from the free-standing single-layer Bi_2Se_3 compared with the bulk material.[252] Unlike other preparation techniques, the ionic liquid solvothermal (ionothermal) technique (where the ionic liquid functions as an intercalating and stabilizing agent) was introduced to synthesize few-layer rhombohedral Bi_2Se_3.[253] A similar rhombohedral Bi_2Se_3 offers high mobility and scattering-resistant carriers owing to its unique surface morphology, which in turn showed high electrical conductivity and low thermal conductivity.[253] Furthermore, a microwave-assisted solvothermal method was used to prepare 2D rhombohedral Bi_2Se_3 with a controllable thickness using poly(N-vinyl-2-pyrrolidone) (PVP) as a stabilizer, as shown in **Figure 9**.[254] The quintuple layers (QLs) should be disassembled to obtain Bi_2Se_3 nanosheets, as shown in Figure 9a. Only bulk Bi_2Se_3 was prepared without using PVP. PVP could impede the stacking of the QLs. Bi_2Se_3 nanosheets with thicknesses of 13, 7, 4, and 1 nm were fabricated using this technique with the PVP/Bi_2Se_3 molar ratios of 0.0025, 0.0125, 0.025, and 0.05, respectively.[254] The compression of these nanosheets into cylinder-shaped bulk samples with the application of spark plasma sintering showed higher thermoelectric performance compared to bulk materials. This is evidenced by the broadened bandgap and optimized Fermi level. Xie et al. demonstrated the precipitation method for synthesizing very small (less than 50 nm) rhombohedral two-layer Bi_2Se_3.[255] In this method, PVP is used as a capping agent, which is suitable for in vivo applications. Similar synthesized Bi_2Se_3 showed a high photothermal
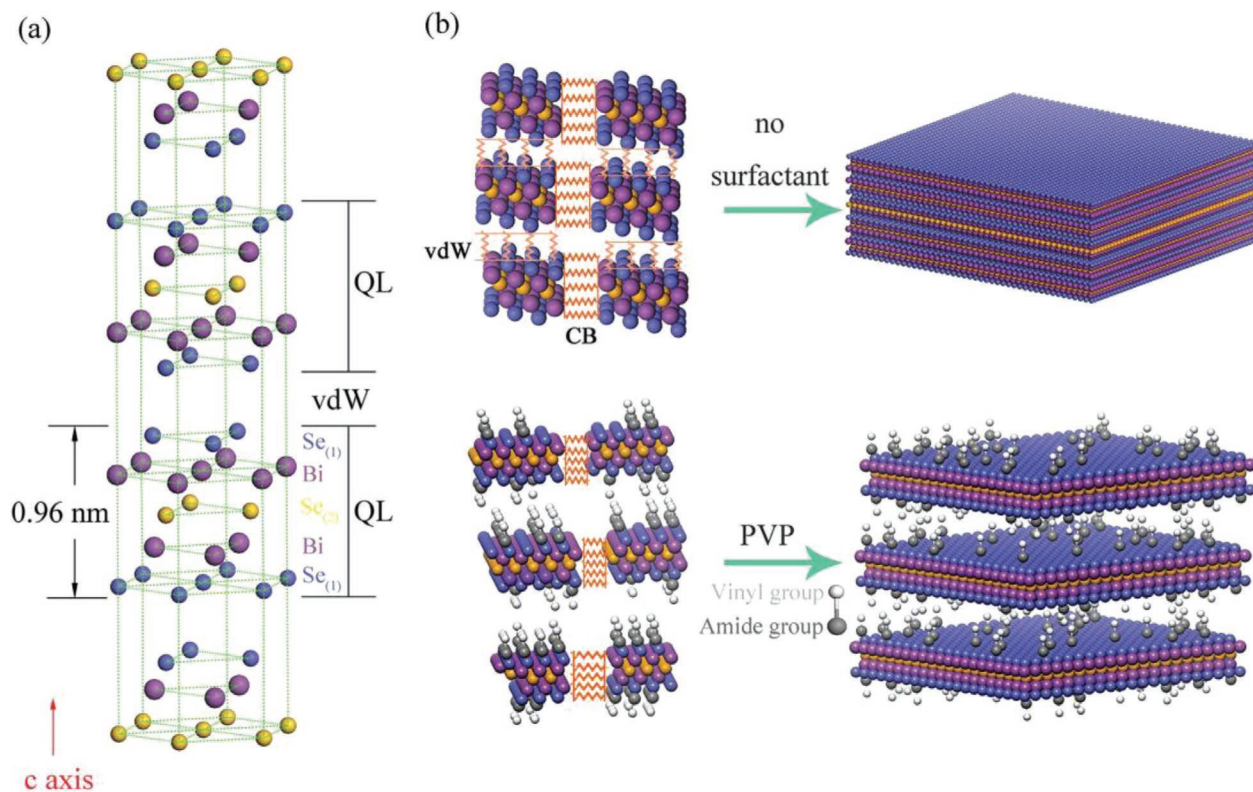
Figure 9. Scheme of a) Bi_2Se_3 rhombohedral crystal structure with Se–Bi–Se–Bi–Se layers (quintuple layers, QL) connected by the van der Waals force (vdW); b) morphology evolution of Bi_2Se_3 NSs prepared with and without PVP. CB: covalent bonding. a,b) Reproduced with permission.[256] Copyright 2015, Wiley-VCH.

**ADVANCED
SCIENCE NEWS**

www.advancedsciencenews.com

**ADVANCED
FUNCTIONAL
MATERIALS**

www.afm-journal.de

conversion efficiency of NIR absorption, making this material a good candidate for the hydrothermal therapy for cancer. Furthermore, Song et al. investigated the formation mechanisms of 2D rhombohedral Bi_2Se_3 and ternary $Bi_2(Se,Te)_3$ through in-situ XRD measurements. The formation mechanism was divided into three steps based on this investigation: nucleation, oriented attachment of the nuclei, and slow epitaxial growth.[256]

Bi_2Se_3 nanoplates intercalated with copper atoms showed a large enhancement in light transmission. This is in contrast to most bulk materials, where doping reduces the light transmission and electrical conductivity.[257] The intercalation-assisted chemical tuning effect of the substantial reduction of material absorption and the nanophotonic effect of zero-wave antireflection on the ultrasmall thickness of nanoplates resulted in this unusual behavior.[257] Hence, Bi_2Se_3 has the potential for various applications, such as transparent electrodes and tunable optoelectronic devices. Subsequently, the dual-element intercalation effect on 2D Bi_2Se_3 nanoribbons was demonstrated via a stepwise combination of disproportionation redox reactions and hydrazine reduction or carbonyl decomposition.[258] Intercalation is observed to be the critical ingredient for enhancing the capacity of energy storage devices from batteries to supercapacitors. It is also considered as an effective method to modify the properties of inherent materials.[258] The CVD method was also used suitably to synthesize microsized rhombohedral Bi_2Se_3 nanoribbons or nanoplatelets with a thickness of tens of nanometers.[259] Moreover, a universal solvothermal method using ethylene glycol as a solvent and reducing agent, and PVP as a stabilizing agent yielded hexagonal-shaped rhombohedral 2D$(Sb, Bi)_2(Se,Te)_3$.[260] Furthermore, a microwave-stimulated wet-chemistry method using tri-n-octylphosphine as a solvent was employed to prepare sulfur-doped rhombohedral Bi_2Te_3 and Bi_2Se_3 nanosheets. This synthesis technique was observed to be rapid and effective for scaling up n- and p-type nanosheets. Pellets formed by compressing these nanosheets also exhibited a very high ZT value (above one). This study showed that the Seebeck coefficient is highly sensitive to the sulfur doping level, which significantly alters the density of states near the Fermi level.[261] Although highly remarkable progress has been achieved in the synthesis of Bi_2Se_3 nanosheets, high-yield synthesis for realizing topological insulator behavior remains to be attained. Toward this direction, Kong et al. solvothermally synthesized uniform Bi_2Se_3 nanoplates with compensational Sb doping during synthesis. This resulted in a good control of the carrier concentration on Bi_2Se_3 and paved the way for the exploration of topological properties.[262]

Recently, other approaches (such as a top-down electrochemical exfoliation approach in aqueous solutions,[263] selective nucleation and growth at desired locations on a patterned mica substrate,[35] and molecular beam epitaxy on $Al_2O_3(0001)$ and amorphous SiO_2 (a-SiO_2) substrates[264]) have also been demonstrated to synthesize large-area and uniform Bi_2Se_3 and Bi_2Te_3. These can be transferred onto various substrates including the common transparency sheet. Guo et al. observed that Cu-intercalated 2D Bi_2Se_3 electrodes exhibit high uniformity and remarkable environmental stability. The high density of intercalated copper atoms significantly affected the electrical and optical performance of the Bi_2Se_3 electrodes. The intercalation improved the performance of the Bi_2Se_3 electrodes from 900 Ω sq^{-1} (68%) to 300 Ω sq^{-1} (82%) in the visible range and to 300 Ω sq^{-1} (91%) in the near-infrared region. Hence, copper intercalation in topological insulator grid nanostructures may expand their potential applications in high-performance optoelectronic devices, particularly in infrared optoelectronic devices.[265]

4.1.4. Bi_2Te_3

In a pressure-induced reversible process, many distinct structural phases such as rhombohedral (I), monoclinic (II, III), and cubic (IV) were observed in nanostructured Bi_2Te_3.[266] A facile solution-phase method was observed to be effective in synthesizing the nanostructure of Bi_2Te_3. Pressure-induced phase transformations from rhombohedral (I) through monoclinic (II, III) up to cubic (IV) was observed after the pressure was increased to 20.2 GPa.[266] Remarkably, this nanostructured Bi_2Te_3 transformed into a Bi–Te substitutional nonmetallic alloy at a pressure of 15.0 GPa. This is ≈10 GPa lower than that of its bulk counterpart. This reduced transition pressure is attributed to the synergistic effect, which involves a large volume collapse, and the unique 1D nanostructures with an intrinsic substitutional aspect that originates defects in the antisite $BiTe_2$. 2D Bi_2Te_3 nanosheets were also synthesized on a Si substrate via the surface-assisted CVT technique. Bi_2Te_3 nanosheets grow in the basal plane of the hexagonal Bi_2Te_3 structure and are typically a few nanometers in thickness.[267] The details available on the electronic and thermal properties of these 2D Bi_2Te_3 nanosheets are limited. Their important thermoelectric materials and topological applications also need to be investigated. Lu et al. addressed another two-step epitaxial growth of cylindrical strings of Bi_2Te_3 nanoplatelets using a high-temperature organic solution approach.[268] Similar nanoplatelets were grown on the surface of the Te rod along the c-axis in a top–bottom–top–bottom sequence. This method achieved the growth of single-crystal, defect-free, and hexagonal Bi_2Te_3 nanoplatelets. In this growth, the c-direction of the Bi_2Te_3 nanoplatelet and c-axis of the Te rod are always parallel to each other. Hence, after a size-selective posttreatment, the single component of 1D aligned strings of Bi_2Te_3 nanoplatelets can be refined and isolated by separating and removing the individual Bi_2Te_3 nanoplatelets. These 1D nanostructures containing phase boundaries on nanofacets can be used effectively in the design of low-dimensional thermoelectric building blocks. These blocks have the potential to achieve a high thermoelectric ZT and noteworthy topological properties. Recently, Jiang et al. reported the development of vertical out-of-plane and planar in-plane Bi-based TI nanoplates (including Bi_2Te_3 and Bi_2Se_3) on a mica substrate using the CVD method.[269] Here, the vertical TI nanoplates exhibited a strong tendency to assemble into a 1D array. This effect can be attributed to the directional interfacial stress between the nanoplates and underlying Bi_2O_3 buffer layer. Furthermore, Goyal et al. reported "graphene-like" mechanically exfoliated single-crystal Bi_2Te_3 films.[270] These showed a decrease in the room-temperature in-plane thermal conductivity of the stacks by a factor of ≈2.4, compared with the bulk counterpart. This reduction in thermal conductivity while retaining the electrical properties resulted in a large increase in the thermoelectric figure of merit.

ADVANCED
SCIENCE NEWS
www.advancedsciencenews.com

ADVANCED
FUNCTIONAL
MATERIALS
www.afm-journal.de

4.2. Sb–X (Sb$_2$O$_3$, Sb$_2$S$_3$, Sb$_2$Se$_3$, Sb$_2$Te$_3$)

4.2.1. Sb$_2$O$_3$

Sb$_2$O$_3$ exhibits two polymorphs: a cubic α phase and an orthorhombic β phase with bandgaps of 4 and 3.3 eV.[271] α-phase Sb$_2$O$_3$ is a potential anodic material for rechargeable batteries owing to its high capacity and abundance of natural deposits. With regard to its synthesis, Zhou et al. reported a solvothermal reaction for the facile synthesis of a densely packed Sb$_2$O$_3$ nanosheet–graphene aerogel composite.[272] This Sb$_2$O$_3$/graphene composite displayed a reversible capacity of 657.9 mAh g^{-1} even after 100 cycles at 0.1 A g^{-1}. It also exhibited a remarkable rate capacity of 356.8 mAh g^{-1} at 5.0 A g^{-1}. The higher electrochemical performance of this composite is attributed to the synergistic effects of densely packed Sb$_2$O$_3$ nanosheets and graphene airgel. During the hydrothermal process, the addition of different types of amines controlled the phases owing to the steric effect. The use of tetramethylethylenediamine favored the formation of the α phase. Meanwhile, the β phase was prepared conveniently by adding ethylenediamine and 1,2-diaminocyclohexane.[273]

Similar to phosphorene, Sb$_2$O$_3$ has also opened up substantial scopes in the 2D monolayer family. Sb$_2$O$_3$ is a 2D topological insulator with a large global bandgap of 177 meV.[274] This material has a nontrivial Z$_2$ topological invariant in the bulk and topological states on the edge. Moreover, these tunable direct bandgaps, which cover a wide range (0–2.28 eV), are of high importance for solar cell and photodetector applications.

4.2.2. Sb$_2$S$_3$

For 2D Sb$_2$S$_3$, only crystalline orthorhombic and amorphous phases were reported. The colloidal synthesis of amorphous a-Sb$_2$S$_3$ (III) nanostructures via a mixture solution of different long-chain primary amines was demonstrated by Wang et al.[275] These organic amines function as a template for the 2D growth of a-Sb$_2$S$_3$ (III) through the coordination of metal cations with the amine group. Thermal analysis revealed that the amorphous–crystalline phase transformation is accompanied by the desorption and/or decomposition of organic surfactant molecules and S loss. These Sb$_2$S$_3$ nanostructures exhibited photoelectronic properties in an indium tin oxide (ITO)/Sb$_2$S$_3$/ITO model device, namely, a fast temporal photoresponse and photoswitch capability. Orthorhombic Sb$_2$S$_3$ can be prepared by various methods such as the solvothermal method,[276,277] liquid exfoliation,[278,279] and electrochemical lithium intercalation.[280] The Sb$_2$S$_3$ nanosheets can be grown directly on graphene with enhanced catalytic properties owing to the synergism of the superior conductivity of graphene and the 2D nanostructures of Sb2S3.[276] In the one-step high-shear exfoliation using an ethanol/water solvent, water promotes exfoliation by a lower diffusion barrier along the [010] direction of Sb$_2$S$_3$, whereas ethanol functions as the carbon source for in situ carbonization.[278] This few-layer Sb$_2$S$_3$ can minimize the volume expansion during passivation and shorten the ion transport pathways. The latter enhances the rate capability of potassium-ion batteries.[278] Subsequently, Zhu et al. demonstrated the development of flower-like Sb$_2$S$_3$

structures through a simple and convenient polyol reflux process.[281] When tested as an anode for sodium-ion batteries, this material delivered a high reversible capacity of 835.3 mAh g^{-1} at 50 mA g^{-1} after 50 cycles and maintained a capacity of 641.7 mAh g^{-1} at 200 mA g^{-1} after 100 cycles. This indicates a remarkable cycle performance and a superior rate capability. The high rate capability is a result of the shortened diffusion paths for Na ions and electrons. The stable cycling behavior can be attributed to the accommodation of the strain generated during cycling. For Li–S batteries, Sb$_2$S$_3$ nanosheets effectively reduced the shuttling effect of soluble polysulfides with binding strengths of 1.33–2.14 eV to entrap Li$_2$S$_x$. Moreover, these nanosheets achieved a low-energy barrier of 189 meV for Li diffusion, yielding a significantly improved specific capacity.[280]

4.2.3. Sb$_2$Se$_3$

Orthorhombic Sb$_2$Se$_3$ nanosheets were grown by liquid-phase exfoliation with the help of freezing.[282–284] There are two strategies for the freezing process: slow freezing with gentle sonication and fast freezing with vigorous sonication. In the slow freezing process, water is first pumped into interribbon voids with the help of shearing stress. Then, the volume expansion from liquid water to ice induced by freezing produces a strong force to separate the layers of the Sb$_2$Se$_3$ sheets.[282] In the liquid nitrogen process, large Sb$_2$Se$_3$ powders are broken into small fragments. The subsequent sonication can effectively exfoliate the layer structures.[284] Surface modification of PVP enables the development of Sb$_2$Se$_3$ nanosheets with high biocompatibility and therapeutic biosafety for in vitro and in vivo applications such as photothermal therapy, antibacterial infections, and photoacoustic imaging.[283–285] A 2D amorphous Sb$_2$Se$_3$/C composite was prepared using a simple ball-milling process.[286] As an anode for Li- and Na-ion batteries, this material exhibited remarkable electrochemical capabilities such as high reversible capacities, long cycle life, and high rate capabilities.

4.2.4. Sb$_2$Te$_3$

The amorphous and crystalline states of Sb$_2$Te$_3$ (rhombohedral) nanosheets have been reported. The hydrothermal method is the most commonly used method for preparing Sb$_2$Te$_3$ nanosheets.[287] While applying this method, Saltzmann et al. observed different amorphous intermediates along the reaction path to the final Sb$_2$Te$_3$ hexagonal platelets.[288] In situ nanomanipulator measurements on this Sb$_2$Te$_3$ revealed the electrical phase-change switching properties of Sb$_2$Te$_3$ hexagonal platelets.[288] Microwaves can assist the solvothermal process in producing Sb$_2$Te$_3$ nanosheets effectively. Furthermore, a graphene–Sb$_2$Te$_3$ heterostructure can be obtained by adding graphene to the solution.[289] Combing solvothermal and carbonization techniques can prepare Sb$_2$Te$_3$/C nanoplates that exhibit good electrochemical performance as anode materials for alkali battery systems.[290] The electrochemical reaction mechanism between Sb$_2$Te$_3$ and Li was investigated thoroughly using ex situ XRD.[291] Apart from hydrothermal methods to synthesize Sb$_2$Te$_3$ nanosheets, solution-based methods have also been reported. For example, Wang et al. reported a room-temperature preparation

by reducing $BiCl_3$ and orthotelluric acid with hydrazine in the presence of thioglycolic acid to control the thickness from 3 to 40 nm. Moreover, Schulz et al. demonstrated the size-selective synthesis of hexagonal Sb_2Te_3 nanoplates by the thermal decomposition of the single-source precursor bis(diethylstibino) telluride $(Et_2Sb)_2Te$.[292] These Sb_2Te_3 nanosheets are thermoelectric materials with a high ZT. In particular, the high density of states, increased phonon scattering, and reduced lattice thermal conductivity in nanostructuring thermoelectric materials promote factorial enhancements in ZT.[293]

5. Group III–V

Monolayer group III–V binary compounds (M = B, Al, Ga, In; X = N, P) can have a planar or buckled structure. The prediction shows that compounds formed with first-row elements, i.e., B, and N, are planar stable, whereas those formed with the other elements tend to be bulked. All these are semiconductors with a bandgap determined by the constituent atoms.[294]

5.1. X–N (BN, AlN, GaN)

Most reports involve 2D BN with a hexagonal structure (h-BN), which is an isomorph of graphene with a similar layer structure. 2D h-BN has high chemical stability,[295] high thermal stability and conductivity,[296] good mechanical strength,[297] and high transparency.[298] For a long time, mono- and few-layer h-BN have been prepared using various methods such as mechanical/liquid exfoliation techniques and chemical and physical depositions.[299] Zhang et al. summarized their synthesis, properties, and applications in an informative review.[300]

A new phase, amorphous 2D-BN, was also successfully prepared on various substrates such as metals, ceramics, and polymers, and on other 2D materials including graphene and few-layer MoS_2, by utilizing a low-temperature (<200 °C) pulsed laser deposition method.[301] The dielectric constant and breakdown voltage measurements for various thicknesses of the ultrathin amorphous BN material were higher than those of the previously reported CVD h-BN.[302]
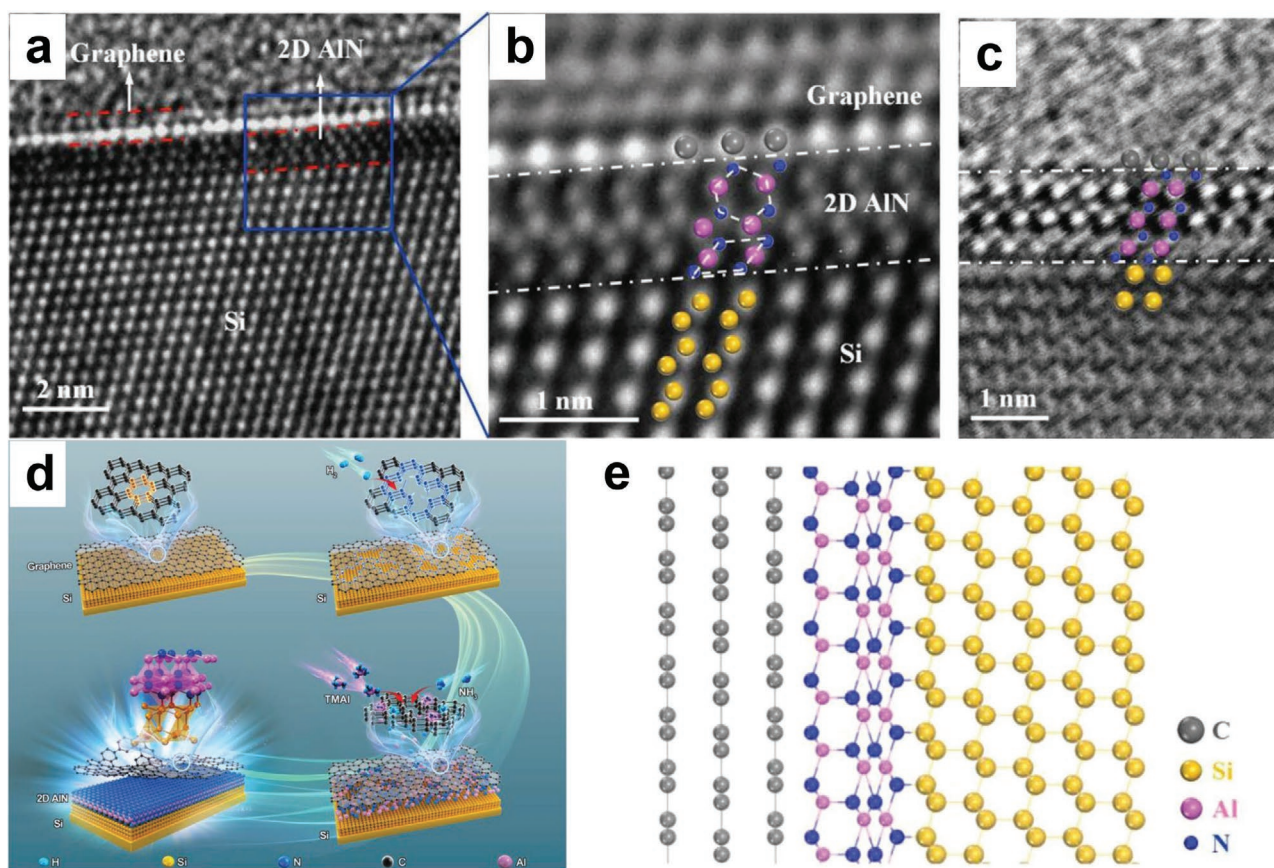
AlN nanosheets have a hexagonal crystal structure (wurtzite) with a wide bandgap of 6.2 eV. They show remarkable insulating properties, high thermal conductivity, high chemical and thermal stability, and high dielectric permittivity. Therefore, they are suitable for use as gate dielectrics.[303] Organic and inorganic (MoS_2) field-effect transistors fabricated with AlN as a gate dielectric showed high performance in terms of stability, on/off ratio, operation voltage, and saturation mobility.[303,304] Furthermore, a theoretical calculation predicted that 2D AlN is also a good candidate for Li^+/Na^+ ion batteries, gas sensors, and piezoelectricity.[305] ALD, PVD, and vapor phase transport are the main methods for preparing 2D AlN directly.[303,304,306] Recently, atomically thin hexagonal AlN with a widened bandgap of 9.2 eV was produced successfully by a selective thermal evaporation process and metal-organic chemical vapor deposition (MOCVD).[307,308] The growth process of 2D AlN in graphene/Si heterostructures is shown in **Figure 10**. The structure of graphene and passivated dangling bonds between

graphene and Si substrates were broken with the help of hydrogenation. This opened the path for AlN growth into the interlayer (Figure 10d). Three layers of graphene are required because the structure of graphene with one to two layers can be damaged by hydrogenation, and a thicker graphene cannot open the path for AlN precursor atoms into the interlayer. The crystal structure of 2D AlN transformed from the $R3m$ structure to the $P63mc$ structure owing to a lattice mismatch between Si and AlN (19%). This was verified by the atomistic model constructed and calculated with DFT (Figure 10e).[308]

Bulk GaN has a wurtzite structure and is a direct semiconductor with a wide bandgap.[309] At the early stage of its predicted 2D form, the hexagonal phase is stable with a honeycomb structure.[284] A theoretical study showed that a few-layer h-GaN became unstable and spontaneously reconstructed into a 3D structure with hexagonal in-plane albeit covalent interlayer bonds that form alternating octagonal and square rings.[310] An indirect-to-direct transformation was observed during the reconstruction. Further study showed that this so-GaN is robust and stable at high temperatures. Furthermore, the stability of a single layer of this squareoctagonal structure (such as Haeckelite) was verified,[311] and its magnetic and electronic properties were investigated. This study showed that adatom adsorption and cation–anion vacancies can modify their electronic and magnetic properties. However, the first successfully prepared 2D GaN was a hexagonal phase, in which graphene played a critical role in stabilizing the 2D buckled structure.[312] 2D GaN was prepared via a migration-enhanced encapsulated growth (MEEG) technique (**Figure 11**). The proposed MEEG process for 2D GaN growth in graphene follows three steps. First, the trimethylgallium precursor decomposes into a gallium atom and is adsorbed on the graphene surface. Second, the gallium atoms intercalate and diffuse into the interface of graphene and the substrate. Finally, the confined gallium atoms transform into 2D GaN by ammonolysis. This method is expected to be highly effective for preparing other 2D group-III nitride semiconductors.[312] Similarly, the 2D GaN growth mechanism was also demonstrated using plasma-enhanced MOCVD. Here, the use of plasma transformed the phase from the trigonal structure to the hexagonal structure as well as controlled the layers. This resulted in the variation of the bandgap from 4.18 to 4.65 eV.[313] Owing to the low melting point of gallium, surface-confined nitridation on liquid gallium was carried out to prepare microsized single-crystal 2D GaN. It exhibited blue shifts and enhanced photoluminescence emission.[314] In another method, a nitrogen neutral beam produced by passing N_2 plasma through an aperture plate was used as a nitrogen source for synthesizing GaN at room temperature. Polycrystal wurtzite GaN nanosheets mixed with the rock-salt phase were obtained on a selective area that exhibited a typical photoluminescence spectrum.[315]

5.2. XP (BP, AlP, GaP, InP, InP₃)

Bulk BP has many phases such as ZB, rock salt, and β-Sn.[316] Recently, a 2D hexagonal BP (h-BP) was predicted to be a planar and graphene-like structure with a direct bandgap of 0.9 eV.[317,318] The substitution of B or P with group III–IV–V elements was systematically studied and considered an

**ADVANCED
SCIENCE NEWS**
www.advancedsciencenews.com

**ADVANCED
FUNCTIONAL
MATERIALS**
www.afm-journal.de

Figure 10. Cross-sectional TEM images of AlN layers sandwiched between graphene and Si substrates at a) low-magnification and b) high magnification; c) annular bright-field (ABF)-scanning transmission electron microscopy (STEM) image; d) schematic growth of 2D AlN layers sandwiched between graphene and Si substrates; e) schematic diagram of 2D AlN layers sandwiched between graphene and Si substrates. a–e) Reproduced with permission.[310] Copyright 2019, Wiley-VCH.

effective method to modify the electronic structure of the h-BP monolayer, such as the n/p type and bandgap.[319] First-principle studies have shown that the *h*-BP monolayer is effective as an anode material for alkali-based batteries with an extraordinary storage capacity of 1283 mAh/g or as an anchoring material for Li–S batteries.[317,320] The semiconductor metal transforms with Li, Na, and K interactions, which endows it with good electrical conductivity for use as an anode material.[321]

Hexagonal AlP and GaP monolayers were also predicted as graphene-like structures. Their electronic and optical properties were observed to have high mechanosensitivity.[322] Their energy gaps were altered with an applied strain, in accordance with a second-order polynomial equation. Moreover, the optical absorption spectra of these materials exhibited blue and redshifts corresponding to compressive and tensile strains. The experimentally prepared 2D InP with a flag shape was realized by VLS growth and is a wurtzite structure.[323] During the growth of InP nanowires, the nanowire tip was asymmetrically dissolved into the catalyst and then unpinned with Au particles. Then, epitaxial growth occurred along a nanowire facet. This technique opened the way for the synthesis of 2D nanomembranes with a crystal structure determined by a 1D nanowire sidewall template. These nanoflags exhibited room-temperature and linearly polarized PL perpendicular to the elongation direction of the nanoflag. The tip geometry enabled a significant

enhancement in the electric field intensity, which can be applied to nonlinear effects and as a nanoantenna.

InP_3 is another 2D form of the In-P system, according to a theoretical study. There are two phases of the InP_3 monolayer: β (hexagonal, $Pm1$) and δ (monoclinic, $P1$).[324] β-InP_3 has an indirect bandgap of 1.14 eV and high electron mobility. P-type doping or defect engineering may induce tunable magnetism and half-metallicity in the β-InP_3 monolayer, and electron or high-concentration hole doping can cause a semiconductor–metal transition.[325] The Seebeck coefficient of β-InP_3 was predicted to be 2.0(1.95) mV K^{-1} with p (n)-type doping. This would result in a high ZT of 2.06 at room temperature.[326] Furthermore, the β-InP_3 monolayer showed extraordinary optical absorption in the entire visible solar spectrum. This makes it a potential candidate for nanoscale electronic, photovoltaic, and spintronic applications.[325] As a layer material, 2D β-InP_3 was also predicted to be suitable for Li(Na)-ion batteries with ultrafast charge/discharge capability, high stability, and reversibility.[327] The δ-InP_3 monolayer was determined to be a semiconductor with an indirect bandgap of 0.51 eV and exhibited anisotropy with a tunable bandgap under applied strain. This phase was determined to be stable at room temperature, and the exfoliation energy of the δ-InP_3 monolayer was 40% lower than that of the β-InP_3 monolayer. Furthermore, it was indicated that the metal substrate favors the formation of the δ-InP_3

**ADVANCED
SCIENCE NEWS**
www.advancedsciencenews.com

**ADVANCED
FUNCTIONAL
MATERIALS**
www.afm-journal.de
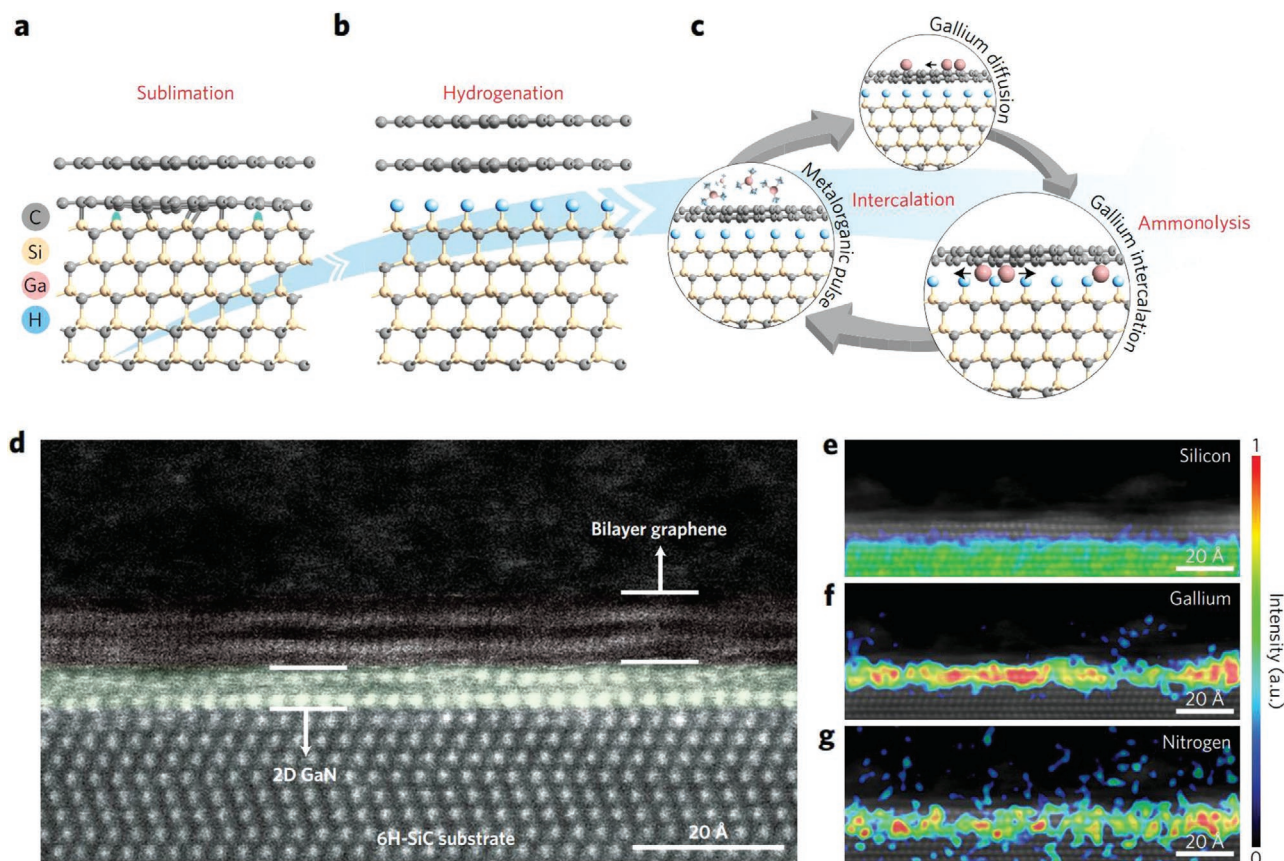
Figure 11. a–c) Schematic of the migration-enhanced encapsulated growth processes that result in the formation of 2D GaN. d) HAADF-STEM cross-section of 2D GaN consisting of two sublayers of gallium between bilayer graphene and SiC(0001). Elemental EDX mapping of e) silicon, f) gallium, and g) nitrogen in 2D GaN. a–g) Reproduced with permission.[314] Copyright 2016, Springer Nature.

monolayer.[324] Finally, the calculation values of the absorption of different gases on the δ-InP$_3$ monolayer indicated the superior sensing performance of this material.

6. Group IV–V

In general, two polytypes of 2D group IV–V materials (M = Si, Ge, Sn; X = N, P, As) were predicted: monoclinic (*Cm*) and hexagonal (*Pm*2) phases.[328] The formation energies of 2D group IV–V compounds were calculated for the two phases (**Figure 12**). The value of 200 meV/atom was considered the formation energy threshold for free-standing 2D materials.[329] According to the calculation, the monoclinic structure was more stable for As, Sb, and Bi compounds, whereas the hexagonal structure was more stable for P compounds. The band energy levels of the nine potentially stable compounds with the two phases are also given to demonstrate that these materials are good candidates for water splitting. In addition to the compounds shown in Figure 12, single-layer hexagonal group-IV nitrides were predicted as stable indirect semiconductors. Their bandgaps showed an almost linear response for the strain, which is suitable for mechanical sensors.[330] However, in other studies, P compounds also showed the most stable monoclinic phase. For example, bulk SiP is an indirect semiconductor with a bandgap of 1.69 eV and was successfully prepared

experimentally. According to this calculation, the stable phase of monolayer SiP was monoclinic (different from a previous study) and was thermodynamically and dynamically stable even at 900 K. The bandgap of the monolayer transited to a direct bandgap of 2.59 eV from the indirect bulk.[331] In the following, we discuss the reported 2D group IV–V materials and their phases individually.

6.1. Ge–X (GeAs, GeAs$_2$, GeP, GeP$_2$, GeP$_3$, Ge$_3$P$_2$)

6.1.1. GeAs, GeAs$_2$

Ge–As compounds are of two stoichiometric ratios: GeAs and GeAs$_2$. For 2D GeAs, the monoclinic phase has been experimentally observed to be the most stable. The other hexagonal phase was predicted to be dynamically stable.[332] Based on the simulation, the monolayer hexagonal GeAs is an indirect semiconductor (2.08 eV) and transforms into a direct semiconductor (1.6 eV) under in-plane strain. The H21 phase was preferred when these stacked with each other via van der Waals interactions. This phase showed high chemical stability, high charge carrier mobility, and broad electrochemical windows.

The experimental preparation of the monoclinic-monolayer and few-layer GeAs (*C2/m*) using a mechanical or liquid-phase exfoliation method has been reported.[333,334] The crystal

**ADVANCED
SCIENCE NEWS**
www.advancedsciencenews.com

**ADVANCED
FUNCTIONAL
MATERIALS**
www.afm-journal.de
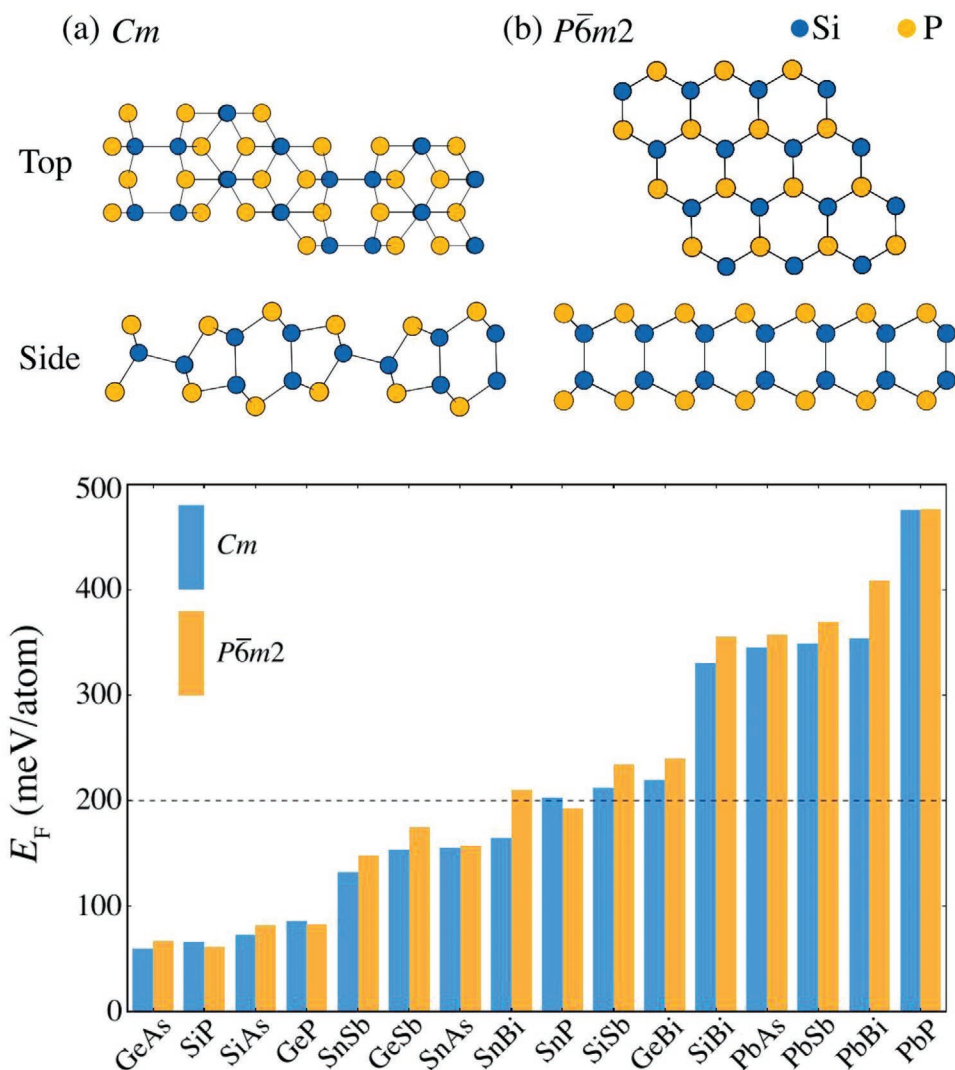
Figure 12. (Up) Crystal structures of 2D SiP in (a) *Cm* crystal structure and b) *Pm*2 crystal structure. (Down) Formation energies of the 16 2D IV–V compounds in the investigation relative to their most stable bulk competing phases. Several compositions fall within the 200 meV atom^{-1} formation energy threshold observed for free-standing 2D materials. a,b) Reproduced with permission.[330] Copyright 2016, AIP Publishing.

orientations and in-plane anisotropic optical and electrical properties were characterized well by azimuth-dependent reflectance difference microscopy, angle-resolved Raman spectra, and electrical transport measurements. Compared with the indirect bandgap of 0.65 eV for the bulk material, the bandgap of the monolayer GeAs showed a large blue shift to 2.1 eV and turned into a direct semiconductor. Few-layer GeAs showed quasi-direct bandgaps of 1.3, 1.1, and 1.0 eV for 2L, 3L, and 4L, respectively. This enables various applications such as high-performance optoelectronic nanodevices and PEC water splitting, because of the coverage of the visible range of the bandgap. Field-effect transistors and infrared photodetectors based on few-layer monoclinic GeAs showed a high on-off ratio and fast photoresponse to 1.6 μm radiation.[333]

Orthorhombic (*Pbam*) GeAs$_2$ (which is another layer structure with a different stoichiometry of Ge and As) was also predicted to be a good material for thermoelectric applications.[335] 2D GeAs$_2$ is expected to display more desirable properties and to be obtained by the exfoliation method.

6.1.2. GeP, GeP$_2$, GeP$_3$, Ge$_3$P$_2$

The study of Ge–P binary compounds is complex because of their different Ge/P stoichiometric ratios, e.g., GeP, GeP$_2$, GeP$_3$, and Ge$_3$P$_2$.[336,337] Two phases of 2D GeP were predicted: the more stable layered monoclinic phase and the less stable hexagonal phase.[332,338] The monolayers of these phases are indirect semiconductors with a bandgap of 2.31 eV (monoclinic) and 2.08 eV (hexagonal). The monoclinic GeP monolayer underwent an indirect-to-direct band transform with the application of tension along the *a* and *b* directions. The bilayer of monoclinic GeP has four parallel paths along the *b* direction. Therefore, the Li-ion can diffuse significantly faster than in graphite. Many phases were predicted for bilayers and multiple layers of hexagonal GeP based on the stacking angles. Among these, H21 is the most stable stacking in the bilayer hexagonal phase.[332,336] The Li-ion diffusion in this phase is comparable to that in graphite.[332] It is noteworthy that hexagonal GeP exhibited a thickness-dependent semiconductor-to-metal transition with a critical layer number of six.[336]

**ADVANCED
SCIENCE NEWS**
www.advancedsciencenews.com

**ADVANCED
FUNCTIONAL
MATERIALS**
www.afm-journal.de

The experimental preparation of monoclinic GeP nanosheets by mechanical and liquid-based exfoliations was reported recently.[339,340] A bandgap of 2.3 eV for monolayer GeP was verified by the experimental results. Furthermore, the electrical properties of the GeP nanosheets were dependent on the thickness.[340] A photoanode device with GeP nanosheets was fabricated and showed good performance of PEC water splitting. Devices fabricated with mechanically exfoliated GeP provided fundamental anisotropic information of the nanosheets, such as strong anisotropy of phonon vibration, high in-plane anisotropic conductance, and photoresponsivity.[339]

Two stable phases of 2D GeP_2 were predicted: tetragonal and orthorhombic. The orthorhombic GeP_2 monolayer displays very high electron mobility with a suitable bandgap for the photocatalysis of CO_2 and water splitting.[336,341] The tetragonal GeP_2 monolayer and bilayer are indirect semiconductors with bandgaps of 2.72 and 2.32 eV, respectively. The orthorhombic GeP_2 monolayer and bilayer have quasi-direct bandgaps of 1.98 and 1.8 eV, respectively. The 2D orthorhombic phase shows higher stability than the 2D tetragonal phase.

GeP_3 bulk material is a crystal with a layer structure (rhombohedral, Rm) and exhibits metal properties. It has been prepared successfully for a long time. The rhombohedral GeP_3 was observed to be semiconductors with indirect bandgaps of 0.55 and 0.43 eV when broken down to one and two layers, respectively. Furthermore, it is chemically, mechanically, and dynamically stable.[342] Cleavage energies were also calculated. These results established the possibility of exfoliation from the bulk material.[343] Rhombohedral layered GeP_3 was prepared by a solid-state method. It showed stable capacity retention when used as anode materials for Li and Na batteries in a study on multiple-step phase-change reaction mechanisms during ion insertion/extraction.[344] In addition, 2D GeP_3 was predicted to be effective as an anode material for non-Li-ion batteries such as Na^+, K^+, Ca^{2+}, Mg^{2+}, and Al^{3+}.[345–347] When it functioned as a catalyst, the Gibbs free energy of hydrogen adsorption on the GeP_3 monolayer (0.024 eV) was calculated to be more desirable than that of the Pt catalyst.[347] Applying an external strain can further optimize the adsorption state of H. Moreover, the charge transfer from GeP_3 to graphene can significantly improve the electrical conductivity and enhance the electrocatalytic activity.[346] Another monoclinic-phase ($C2/m$) GeP_3 monolayer was also proposed. It has higher stability than the rhombohedral phase. Furthermore, hole doping converted the $C2/m$ GeP_3 monolayer from nonmagnetic to ferromagnetic.[336]

Recently, 2D Ge_3P_2 with two new phases, orthorhombic ($Cmmm$) and tetragonal ($P4/mbm$), was proposed to be dynamically, thermally, and mechanically stable based on first-principles calculations.[337] $Cmmm$-Ge_3P_2 and $P4/mbm$-Ge_3P_2 are indirect semiconductors with bandgaps of 1.62 and 1.89 eV, respectively. Their bandgaps can be adjusted effectively by applying external strains. Furthermore, their electron mobilities are comparable to those of graphene, which makes these a potential candidate for electronic and optoelectronic applications.

6.2. Sn–X (SnP₃, SnN₃)

Similar to GeP_3, bulk SnP_3 is a crystal with a layered structure (rhombohedral, Rm) and shows metallic properties. The

cleavage energies of monolayer SnP_3 were calculated to be in the range of 0.57–1.17 J m^{-2}. This indicated the feasibility of producing monolayer SnP_3 through exfoliation.[348,349] The optimized lattice in monolayer SnP_3 alters the bond lengths and bond angles. This results in the shrinkage of the lattice and contributes to the metal-to-semiconductor transition. The monolayer SnP_3 is an indirect semiconductor with various predicted bandgaps ranging from 0.67 to 0.83 eV in different studies. Applying strains can tune the bandgap and result in an indirect–direct bandgap and semiconductor–metal transitions. 2D SnP_3 shows high stability and remarkable electronic and optical properties such as high carrier mobility and good light absorption. Similar to monolayer GeP_3, Na adsorption transfers the semiconducting SnP_3 to a metallic state with good electrical conductivity for use as a potential anode for Na-ion batteries.[349]

It is noteworthy that monolayer SnN_3 was prepared by replacing P in monolayer SnP_3 with N. The corresponding formation energy was calculated to be -220 meV.[350] After lattice optimization, monolayer SnN_3 showed a hexagonal lattice with the symmetry group $Pm1$ and was a stable indirect semiconductor with a bandgap of 1.965 eV. An indirect-to-direct bandgap transition can be obtained by applying biaxial strains. The light absorption coefficient in the visible region was significantly higher than that of the SnP_3, MoS_2, and g-C_3N_4 monolayers. The calculated electrostatic potentials of CB and VB were 0.40 eV higher than those of the HER and 0.34 eV lower than that of the OER. This indicates their capability for photocatalytic water splitting.

6.3. Si–N (SiN₂, HSiN, Si₃N₄)

In general, the crystals of dinitrides have a rock-salt structure (Pa) with a wide bandgap for SiN_2 and a smaller bandgap for CN_2 and GeN_2.[351] A new pentastructure was predicted for the 2D phase,[352] and its thermal transport properties were studied. The thermal conductivity of penta-SiN_2 is dependent on the strain and can be enhanced by an order of magnitude because of the structural transition from buckled to planar. This 2D pentagonal structure is good for applications such as thermoelectrics, thermal circuits, and nanoelectronics. Recently, hexagonal HSiN was predicted by calculations.[353] The stable H-SiN nanosheet had a 2D hexagonal grid of Si and N atoms. The Si dangling bonds were passivated by H atoms, which were placed alternately on the two sides of the sheet. H-SiN nanotubes were also obtained by rolling up these sheets. These stable H-SiN nanosheets and tubes have a direct bandgap and are suitable for nanoscale optical and photonic devices.

As the most thermodynamically stable stoichiometry of silicon nitride, bulk Si_3N_4 has been commercially available because of its hardness. There are three phases of Si_3N_4: α (trigonal), β (hexagonal), and γ (cubic)-Si_3N_4.[354] γ-Si3N4 can be prepared only at high pressure and temperature. The phase engineering of α- and β-Si_3N_4 has been well established.[355] In terms of 2D materials, only α-Si3N4 was reported. α-Si_3N_4 nanosheets with a microlateral size and thickness of 1.5–4 nm were prepared by the reaction of Si vapor with N_2 gas at high temperature.[356] The high temperature and high N_2 flow rates favored the formation of nanosheets rather than nanowires by causing an increase in the growth rate along the [0001] direction

**ADVANCED
SCIENCE NEWS**

www.advancedsciencenews.com

**ADVANCED
FUNCTIONAL
MATERIALS**

www.afm-journal.de

to those along the [100] and [110] directions. A similar method to produce an α-Si$_3$N$_4$ nanobelt with SiO$_2$/Si and SiO as precursors was also reported.[357,358] An alumina-assisted VLS growth mechanism was proposed for the growth of a nanobelt with controllable width and thickness.[358] Furthermore, Al doping in the α-Si$_3$N$_4$ nanobelt was considered to contribute to the optical properties. The optical and electronic properties of the α-Si$_3$N$_4$ nanobelt were also studied by DFT calculations. Herein, the orientations and surface passivation determined the stability of the α-Si$_3$N$_4$ nanobelt as well as its electronic properties such as band characteristics (direct, indirect, and metallic).[359]

7. Group V–V

Although pure 2D group-V element materials such as phosphorene have been extensively studied and realized experimentally, most studies on 2D binary group V–V compounds relied on theoretical predictions. First-principle studies show that the binary group V–V monolayer can be stable in the black-phosphorus-like α phase and blue-phosphorus-like β phase.[360] The formation energies of a few binary monolayers such as α- and β-AsP, SbP, and SbAs were lower than those of pure elements. This indicated their high stability. Other compound monolayers in the α and β phases are thermodynamically and dynamically stable. This indicates the feasibility of experimentally realizing monolayer binary group V–V compounds. In general, the α phase is more stable in nitrogen-containing compounds than the β phase. The most stable δ-phosphorene-like phase was also proposed.[360,361] The bandgaps of these monolayers lie in the range from infrared to visible light (0.49–3.26 eV), implying possible optoelectronic applications.[360,362,363] The bandgap may be indirect or direct depending on the phases and element combinations. In general, δ-phase (except PN) compounds are direct semiconductors, whereas β-phase compounds display an indirect bandgap. However, the α phase was under debate. Therefore, indirect and direct bandgaps were predicted.[360,361] The structure and electronic properties of these compounds can be tuned by the application of strain. This adjusts the bandgap energy of these monolayers as well as induces metal-indirect semiconductors, indirect–direct gap, and semiconductor-topological insulator transitions.[360,361,364] The β-phase group V–V binary monolayers were particularly studied as photocatalysts for water splitting because of their small carrier masses, high electron mobility, suitable bandgaps, and band edge alignments.[362] Under hole doping, the β-phase group V–V binary monolayers became half-metallic with magnetism, and their Curie temperatures were significantly higher than room temperature.[365] Furthermore, α-phase group V–V binary monolayers may be suitable for piezoelectricity and ferroelectricity.[366,367] The piezoelectric coefficients of α-phase monolayers were calculated to be one or two orders of magnitude higher than those of the β-phase monolayers.[366]

7.1. AsP

Many phases have been predicted for AsP monolayers: α, β, γ, δ, and ε phases. Among these, the α and β phases are the most stable.[368] In general, the ground state of the phosphorous monolayer is the α phase and that of arsenic is the β phase. Therefore, As$_x$P$_{1-x}$ compounds undergo a phase transition from α to β when x attains 0.07. Simultaneously, a direct-to-indirect band transform occurs.[369] However, the experimental results show that multiple-layer As$_x$P$_{1-x}$ with a different composition (x: 0–0.83) is in the α phase.[370] α-phase AsP has been well studied experimentally and theoretically in terms of electronic structure, carrier mobility, and lattice thermal conductivity. With the 1:1 stoichiometric mixture of P and As, the 2D α-AsP monolayer displayed a highly anisotropic behavior under strain. It also showed a super-high carrier mobility > 10 000 cm^2 V^{-1} s^{-1} in a subphase α3, which is an order of magnitude larger than that of α-phosphorene.[371] The thermal conductivities were also reduced significantly compared with α-phosphorene because of the substitution of phosphorous atoms with the heavy arsenic atoms.[372] In addition, its remarkable mechanical flexibility shows its good potential for application in flexible devices.[373]

Multiple-layer α-AsP can be prepared by mechanical exfoliation and molecular beam deposition with different compositions.[370,374] Notably, the increase in the arsenic content in α-As$_x$P$_{1-x}$ causes an increase in the size of its unit cell and makes it more difficult to be exfoliated. The bandgaps can also be reduced by increasing the arsenic content, which would result in tunable optical properties. Polarization-resolved infrared absorption and Raman scattering studies showed the anisotropic optical properties of α-As$_x$P$_{1-x}$, indicating its potential applications in electronic and optoelectronic devices. The photodetectors were fabricated with multiple-layer α-AsP for mid-infrared light. At room temperature, the detectivity was an order of magnitude higher than that of commercially available mid-wave infrared detectors.[375] Fabrication with an α-AsP/MoS$_2$ heterostructure further improved the dark current noise performance and the specific detectivity.[376]

Blue β-AsP monolayers with an As:P stoichiometric ratio of 1:1 were investigated at different As and P positions.[377] It is noteworthy that they proposed a series of novel and energetically favored structures by taking two or three As/P atoms together, rather than uniformly distributing As and P in the monolayer. P–P and As–As bonds were formed adjacent to the As–P bond. The lowest-energy AsP monolayer, I-AsP, showed a quasi-direct bandgap (2.41 eV). It can transit to a direct gap under tensile strain. The high electronic mobility and absorption coefficients indicate a unique photovoltaic material for application in solar cells.[377]

7.2. NP, SbP

Three stable phases are predicted for the NP monolayer: α, β, and γ. These are indirect semiconductors, and their bandgaps can be tuned effectively by in-plane strain. The α and β phases are more stable than the γ phase, as established by the formation energy. In addition, the stacking sequence plays an important role in determining the bandgap of multiple-layer NPs with α and β phases.[378] The conduction and valence band edges of the γ-NP monolayer match well with the chemical potential of H$^+$/H$_2$ and O$_2$/H$_2$O, indicating good photocatalysis for water splitting.[379]

Partially substituting two phosphorus atoms with antimony in violet phosphorus produced layered P$_{20.56}$Sb$_{0.44}$ with a thickness down to a few nanometers. The material has high

**ADVANCED
SCIENCE NEWS**
www.advancedsciencenews.com

**ADVANCED
FUNCTIONAL
MATERIALS**
www.afm-journal.de
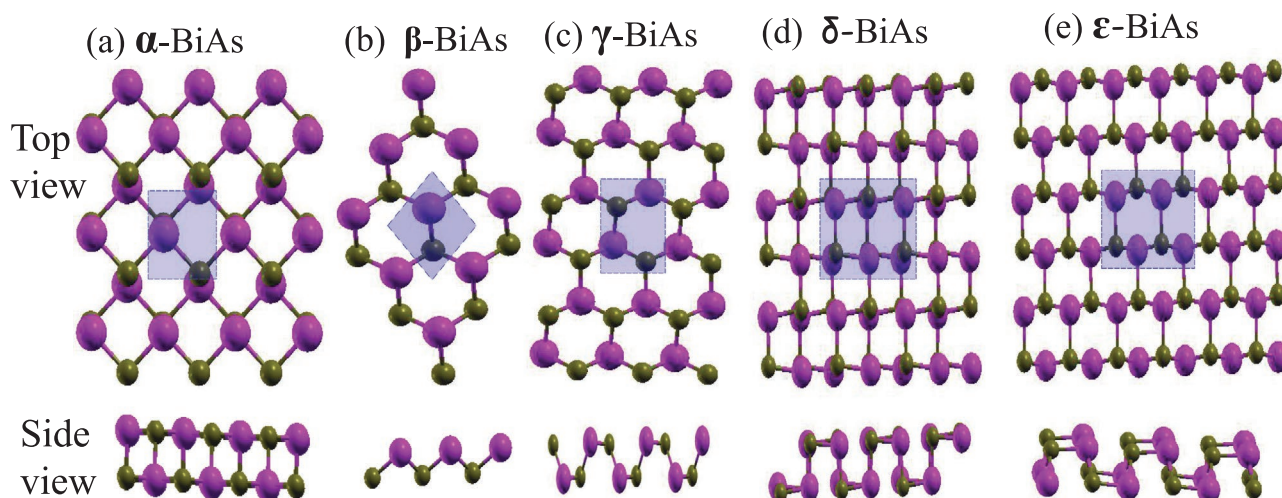
Figure 13. Top and side views of equilibrium structures for the polymorphs of BiAs: a) α-BiAs, b) β-BiAs, c) γ-BiAs, d) δ-BiAs, and e) ε-BiAs. The shaded regions are shown to be unit cells of the polymorphs. Bi: big pink spheres. As: small green spheres. a–e) Reproduced with permission.[383] Copyright 2018, American Chemical Society.

stability and can be cut into a desired shape by a laser. It is a direct semiconductor with a bandgap of 1.67 eV and could be fabricated into field-effect transistors. These exhibited a strong photoresponse, good mobility values, and high on/off current ratio.[380]

7.3. BiAs, SbAs

Five phases have been predicted for 2D BiAs: α, β, γ, δ, and ε (**Figure 13**).[381] The α-BiAs and γ-BiAs have four atoms per unit cell (Figure 13a,c), whereas δ-BiAs and ε-BiAs have eight atoms per unit cell (Figure 13d,e). β-BiAs is the most stable phase and has a hexagonal structure with two atoms per unit cell. Other BiAs polymorphs are dynamically stable. The calculation indicated that α-BiAs (1.27 eV), β-BiAs (1.02 eV), and γ-BiAs (1.01 eV) are direct bandgap semiconductors, whereas δ-BiAs and ε-BiAs are indirect semiconductors. Under strain, β-BiAs undergoes a phase transition to a semimetal and then to a topological insulator.

Similar to BiAs, five phases were predicted for SbAs by DFT: α, β, γ, δ, and ε-SbAs.[382] The α-SbAs has a layer structure similar to that of phosphorene with anisotropic properties. Moreover, the β-SbAs honeycomb monolayer is similar to that of silicene or germanene. Other phases such as γ-, δ-, and ε-SbAs have rectangular unit cells that contain four, eight, and eight atoms per unit cell. α-SbAs (0.22 eV) and γ-SbAs (0.82 eV) were observed to be direct semiconductors, whereas others were indirect semiconductors. β-SbAs was the most stable phase and displayed an indirect bandgap under standard conditions. It is noteworthy that the β-SbAs monolayer can be transformed to a direct band semiconductor under a marginal strain, and then to a topological insulator with a large strain.[382,383] The electronic and magnetic properties of the β-SbAs monolayer can also be adjusted by defect engineering. The [384] β-SbAs monolayer also showed a lower lattice thermal conductivity than that of pure As or Sb

monolayers. This was because phonon-point defect scattering in the β-SbAs alloy induced a short phonon lifetime.[385] The properties of the α-γ – and ε-SbAs monolayers under strain were also predicted. Herein, a semiconductor-to-metal phase transition may occur (–4% strain for α and –8% strain for γ and ε). Moreover, these materials may exhibit highly flexible mechanical properties and ultrahigh carrier mobility for various potential applications such as flexible electronic and optoelectronic devices.[386] In addition to the As:Sb stoichiometric ratio of 1:1, the composition of As_xSb_{18-x} can be altered to determine the electronic properties.[387] For example, the direct bandgap feature occurred in α-As_xSb_{18-x} ($4 \leq \gamma \leq 13$, except $x = 7, 8$) and β-As_xSb_{18-x} ($x = 7, 8$). Furthermore, more substructures with an adjustable bandgap and carrier effective mass were proposed by combining the α and β phases with the arrangement of As/Sb atoms (two As/Sb atoms are in the same sublayer or in different sublayers).[387]

7.4. BiSb

The β-BiSb monolayer with a stoichiometric ratio of 1:1 has been mainly studied theoretically. It is a direct bandgap semiconductor with parabolic conduction band features near the Fermi level. The β-BiSb monolayer exhibited giant Rashba spin splitting, which can be tuned effectively by applying a biaxial strain.[388] The Rashba spin splitting was predicted to induce 1D thermoelectric properties with a remarkable enhancement of the power factor.[389] The β-BiSb monolayer was predicted to exhibit a QSH state as a topological insulator under biaxial tensile strain.[390] The topological insulator properties of 2D BiSb were realized by measuring the temperature-dependent conductivity of the epitaxial-grown 2D $Bi_{1-x}Sb_x$ film with controllable compositions.[391] Owing to the quantum size effect, the TL region of the 2D $Bi_{1-x}Sb_x$ film was observed to be up to $x \approx 0.35$, which is outside the bulk TL region of $0.07 < x < 0.22$.[392]

**ADVANCED
SCIENCE NEWS**

www.advancedsciencenews.com

**ADVANCED
FUNCTIONAL
MATERIALS**

www.afm-journal.de

8. Conclusion and Outlook

This review summarizes the multiple phases in 2D materials based on main group element compounds. It focused on their crystal structures, stability, synthesis methods, electronic and optical properties, and various applications. For structural motifs, a few unstable bulk phases of these materials can be stabilized by breaking them down into their 2D geometric form. Moreover, new phases and new noteworthy properties have been explored with few 2D materials, and similar possibilities have been predicted in many 2D materials. The improved traditional solution-based chemical and vapor-based physical methods are the dominant ones their synthesis. Furthermore, certain new methodologies have emerged, particularly for materials without a layered structure. The properties and traditional applications of these multiphase materials have been widely investigated, such as the photoresponse of group III–VI-based materials and thermoelectric properties of group V–VI based materials. Meanwhile, new applications have also been investigated, wherein the strain-induced property transition and ion-batteries based on layer intercalation are popular. A few of the other new properties and applications rely mainly on theoretical predictions.

However, the phase exploration of these materials is still at very early stages and will remain a significant challenge in the near future. First, the emergence of new stable 2D phases from unstable bulk materials is still underexplored, and the critical layers (thickness) for their stability have been studied inadequately. Surface modifications, contact with an electron donor or acceptor (substrates), and special treatments (such as plasma and electron beams) would substantially solve the stability issues of various phases of 2D materials. These have not been studied for many materials. Second, the properties of this material family in the 2D form need to be explored further. For example, bulk In–Se compounds are popular materials for thermoelectric applications. However, there is no indication of the suitability of the phase control of 2D In–Se for this application. Third, the experimental synthesis of 2D materials with new phases is highly desired to verify theoretical predictions, particularly for existing conflicting conclusions. For example, is the α-phase group V–V monolayer an indirect or direct bandgap semiconductor? The synthesis of group V–V monolayer has not been realized experimentally. In addition, the new proposed phases and new properties that have been predicted need to be demonstrated with real materials. Finally, new property measurement methods need to be established, particularly for strain-induced property measurements. The strain-induced direct–indirect transition, semiconductor–semimetal/metal/TI transition, bandgap shifting, and ferroelectricity, among others, are all potential applications these 2D materials.

Conflict of Interest

The authors declare no conflict of interest.

[1] a) S. Balendhran, S. Walia, H. Nili, Z. Ou Jian, S. Zhuiykov, B. Kaner Richard, S. Sriram, M. Bhaskaran, K. Kalantar-zadeh, *Adv. Funct. Mater.* **2013**, *23*, 3952; b) F. Bonaccorso, L. Colombo, G. H. Yu, M. Stoller, V. Tozzini, A. C. Ferrari, R. S. Ruoff, V. Pellegrini, *Science* **2015**, *347*, 1246501; c) T. Low, A. Chaves, J. D. Caldwell, A. Kumar, N. X. Fang, P. Avouris, T. F. Heinz, F. Guinea, L. Martin-Moreno, F. Koppens, *Nat. Mater.* **2017**, *16*, 182; d) L. M. Wang, W. L. Chen, D. D. Zhang, Y. P. Du, R. Amal, S. Z. Qiao, J. W. Bf, Z. Y. Yin, *Chem. Soc. Rev.* **2019**, *48*, 5310; e) Y. P. Du, Z. Y. Yin, J. X. Zhu, X. Huang, X. J. Wu, Z. Y. Zeng, Q. Y. Yan, H. Zhang, *Nat. Commun.* **2012**, *3*, 7; f) Z. Y. Zeng, Z. Y. Yin, X. Huang, H. Li, Q. Y. He, G. Lu, F. Boey, H. Zhang, *Angew. Chem., Int. Ed.* **2011**, *50*, 11093; g) M. Tebyetekerwa, J. Zhang, K. Liang, T. Duong, G. P. Neupane, L. L. Zhang, B. Q. Liu, T. N. Truong, R. Basnet, X. J. Qiao, Z. Y. Yin, Y. R. Lu, D. Macdonald, H. T. Nguyen, *Adv. Mater.* **2019**, *31*, 8; h) H. Li, G. Lu, Z. Y. Yin, Q. Y. He, H. Li, Q. Zhang, H. Zhang, *Small* **2012**, *8*, 682; i) Z. Y. Yin, H. Li, H. Li, L. Jiang, Y. M. Shi, Y. H. Sun, G. Lu, Q. Zhang, X. D. Chen, H. Zhang, *ACS Nano* **2012**, *6*, 74; j) Z. Y. Yin, Z. Y. Zeng, J. Q. Liu, Q. Y. He, P. Chen, H. Zhang, *Small* **2013**, *9*, 727.

[2] H. Guang, C. Zhi-Gang, D. John, Z. Jin, *Small* **2014**, *10*, 2747.

[3] F. Wang, Z. X. Wang, L. Yin, R. Q. Cheng, J. J. Wang, Y. Wen, T. A. Shifa, F. M. Wang, Y. Zhang, X. Y. Zhan, J. He, *Chem. Soc. Rev.* **2018**, *47*, 6296.

[4] L. Debbichi, O. Eriksson, S. Lebègue, *J. Phys. Chem. Lett.* **2015**, *6*, 3098.

[5] a) J. J. Wang, J. Wang, H. C. Du, L. Lu, P. C. Schmitz, J. Reindl, A. M. Mio, C. L. Jia, E. Ma, R. Mazzarello, M. Wuttig, W. Zhang, *Chem. Mater.* **2018**, *30*, 4770; b) A. D. Oyedele, S. Z. Yang, L. B. Liang, A. A. Puretzky, K. Wang, J. J. Zheng, P. Yu, P. R. Pudasaini, A. W. Ghosh, Z. Liu, C. M. Rouleau, B. G. Sumpter, M. F. Chisholm, W. Zhou, P. D. Rack, D. B. Geohegan, K. Xiao, *J. Am. Chem. Soc.* **2017**, *139*, 14090.

[6] a) N. Uddin, H. Y. Zhang, Y. P. Du, G. H. Jia, S. B. Wang, Z. Y. Yin, *Adv. Mater.* **2020**, *32*, 1905739; b) Z. Q. Liu, N. Li, C. Su, H. Y. Zhao, L. L. Xu, Z. Y. Yin, J. Li, Y. P. Du, *Nano Energy* **2018**, *50*, 176; c) R. He, J. A. Yan, Z. Y. Yin, Z. P. Ye, G. H. Ye, J. Cheng, J. Li, C. H. Lui, *Nano Lett.* **2016**, *16*, 1404.

[7] G. Almeida, S. Dogan, G. Bertoni, C. Giannini, R. Gaspari, S. Perissinotto, R. Krahne, S. Ghosh, L. Manna, *J. Am. Chem. Soc.* **2017**, *139*, 3005.

[8] C. Chang, M. H. Wu, D. S. He, Y. L. Pei, C. F. Wu, X. F. Wu, H. L. Yu, F. Y. Zhu, K. D. Wang, Y. Chen, L. Huang, J. F. Li, J. Q. He, L. D. Zhao, *Science* **2018**, *360*, 778.

ADVANCED
SCIENCE NEWS
www.advancedsciencenews.com

ADVANCED
FUNCTIONAL
MATERIALS
www.afm-journal.de

[9] X. Tao, Y. Gu, *Nano Lett.* **2013**, *13*, 3501.

[10] Q. Zhao, T. Wang, Y. Miao, F. Ma, Y. Xie, X. Ma, Y. Gu, J. Li, J. He, B. Chen, S. Xi, L. Xu, H. Zhen, Z. Yin, J. Li, J. Ren, W. Jie, *Phys. Chem. Chem. Phys.* **2016**, *18*, 18719.

[11] E. G. Gillan, A. R. Barron, *Chem. Mater.* **1997**, *9*, 3037.

[12] W. J. Baumgardner, J. J. Choi, Y.-F. Lim, T. Hanrath, *J. Am. Chem. Soc.* **2010**, *132*, 9519.

[13] Z. Zhu, X. Cai, S. Yi, J. Chen, Y. Dai, C. Niu, Z. Guo, M. Xie, F. Liu, J.-H. Cho, Y. Jia, Z. Zhang, *Phys. Rev. Lett.* **2017**, *119*, 106101.

[14] W. J. Ding, J. B. Zhu, Z. Wang, Y. F. Gao, D. Xiao, Y. Gu, Z. Y. Zhang, W. G. Zhu, *Nat. Commun.* **2017**, *8*, 8.

[15] R. Fei, W. Kang, L. Yang, *Phys. Rev. Lett.* **2016**, *117*, 097601.

[16] Z. Zheng, X. Su, R. Deng, C. Stoumpos, H. Xie, W. Liu, Y. Yan, S. Hao, C. Uher, C. Wolverton, M. G. Kanatzidis, X. Tang, *J. Am. Chem. Soc.* **2018**, *140*, 2673.

[17] S. Guan, C. Liu, Y. H. Lu, Y. G. Yao, S. A. Yang, *Phys. Rev. B* **2018**, *97*, 8.

[18] D. Hsieh, Y. Xia, D. Qian, L. Wray, F. Meier, J. H. Dil, J. Osterwalder, L. Patthey, A. V. Fedorov, H. Lin, A. Bansil, D. Grauer, Y. S. Hor, R. J. Cava, M. Z. Hasan, *Phys. Rev. Lett.* **2009**, *103*, 4.

[19] K. Osamura, Y. Murakami, Y. Tomiie, *J. Phys. Soc. Jpn.* **1966**, *21*, 1848.

[20] J. Ye, S. Soeda, Y. Nakamura, O. Nittono, *Jpn. J. Appl. Phys.* **1998**, *37*, 4264.

[21] S. Demirci, N. Avazli, E. Durgun, S. Cahangirov, *Phys. Rev. B* **2017**, *95*, 8.

[22] a) V. Zolyomi, N. D. Drummond, V. I. Fal'ko, *Phys. Rev. B* **2014**, *89*, 8; b) J. Jalilian, M. Safari, *Phys. Lett. A* **2017**, *381*, 1313.

[23] K. Imai, K. Suzuki, T. Haga, Y. Hasegawa, Y. Abe, *J. Cryst. Growth* **1981**, *54*, 501.

[24] E. Petroni, E. Lago, S. Bellani, D. W. Boukhvalov, A. Politano, B. Gürbulak, S. Duman, M. Prato, S. Gentiluomo, R. Oropesa-Nuñez, J. K. Panda, P. S. Toth, A. E. D. Castillo, V. Pellegrini, F. Bonaccorso, *Small* **2018**, *14*, 1800749.

[25] H. W. Hu, Y. L. Sun, M. S. Chai, D. Xie, J. Ma, H. W. Zhu, *Appl. Phys. Lett.* **2019**, *114*, 4.

[26] W. Feng, W. Zheng, W. Cao, P. Hu, *Adv. Mater.* **2014**, *26*, 6587.

[27] S. Lei, L. Ge, S. Najmaei, A. George, R. Kappera, J. Lou, M. Chhowalla, H. Yamaguchi, G. Gupta, R. Vajtai, A. D. Mohite, P. M. Ajayan, *ACS Nano* **2014**, *8*, 1263.

[28] W. Mudd Garry, A. Svatek Simon, T. Ren, A. Patanè, O. Makarovsky, L. Eaves, H. Beton Peter, D. Kovalyuk Zakhar, V. Lashkarev George, R. Kudrynskyi Zakhar, I. Dmitriev Alexandr, *Adv. Mater.* **2013**, *25*, 5714.

[29] M. J. Dai, H. Y. Chen, F. K. Wang, Y. X. Hu, S. Wei, J. Zhang, Z. G. Wang, T. Y. Zhai, P. A. Hu, *ACS Nano* **2019**, *13*, 7291.

[30] D. A. Bandurin, A. V. Tyurnina, G. L. Yu, A. Mishchenko, V. Zólyomi, S. V. Morozov, R. K. Kumar, R. V. Gorbachev, Z. R. Kudrynskyi, S. Pezzini, Z. D. Kovalyuk, U. Zeitler, K. S. Novoselov, A. Patanè, L. Eaves, I. V. Grigorieva, V. I. Fal'ko, A. K. Geim, Y. Cao, *Nat. Nanotechnol.* **2017**, *12*, 223.

[31] K. Yuan, R. Y. Yin, X. Q. Li, Y. M. Han, M. Wu, S. L. Chen, S. Liu, X. L. Xu, K. Watanabe, T. Taniguchi, D. A. Muller, J. J. Shi, P. Gao, X. S. Wu, Y. Ye, L. Dai, *Adv. Funct. Mater.* **2019**, *29*, 1904032.

[32] W. J. Huang, L. Gan, H. Q. Li, Y. Ma, T. Y. Zhai, *Chem. - Eur. J.* **2018**, *24*, 15678.

[33] Q. Y. Hao, H. Yi, H. M. Su, B. Wei, Z. Wang, Z. Z. Lao, Y. Chai, Z. C. Wang, C. H. Jin, J. F. Dai, W. J. Zhang, *Nano Lett.* **2019**, *19*, 2634.

[34] R. B. Jacobs-Gedrim, M. Shanmugam, N. Jain, C. A. Durcan, M. T. Murphy, T. M. Murray, R. J. Matyi, R. L. Moore, B. Yu, *ACS Nano* **2014**, *8*, 514.

[35] J. Zhou, Q. Zeng, D. Lv, L. Sun, L. Niu, W. Fu, F. Liu, Z. Shen, C. Jin, Z. Liu, *Nano Lett.* **2015**, *15*, 6400.

[36] J. O. Island, S. I. Blanter, M. Buscema, H. S. J. van der Zant, A. Castellanos-Gomez, *Nano Lett.* **2015**, *15*, 7853.

[37] J. Quereda, R. Biele, G. Rubio-Bollinger, N. Agrait, R. D'Agosta, A. Castellanos-Gomez, *Adv. Opt. Mater.* **2016**, *4*, 1939.

[38] a) W. Feng, W. Zheng, F. Gao, X. S. Chen, G. B. Liu, T. Hasan, W. W. Cao, P. A. Hu, *Chem. Mater.* **2016**, *28*, 4278; b) S. Wan, Y. Li, W. Li, X. Mao, W. Zhu, H. Zeng, *Nanoscale* **2018**, *10*, 14885; c) F. Xue, W. Hu, K.-C. Lee, L.-S. Lu, J. Zhang, H.-L. Tang, A. Han, W.-T. Hsu, S. Tu, W.-H. Chang, C.-H. Lien, J.-H. He, Z. Zhang, L.-J. Li, X. Zhang, **2018**, *28*, 1803738; d) X. Wang, A. Y. Cui, F. F. Chen, L. P. Xu, Z. G. Hu, K. Jiang, L. Y. Shang, J. H. Chu, *Small* **2019**, *15*, 1903106.

[39] L. Hu, X. Huang, *RSC Adv.* **2017**, *7*, 55034.

[40] J. Liu, S. T. Pantelides, *2D Mater.* **2019**, *6*, 025001.

[41] B. Nilanthy, R. S. Christopher, F. S. Emily, S. Jakub, G. Dean, W. M. Garry, M. Oleg, R. K. Zakhar, D. K. Zakhar, E. Laurence, P. Amalia, H. B. Peter, *2D Mater.* **2016**, *3*, 025030.

[42] Z. Q. Zheng, J. D. Yao, B. Wang, Y. B. Yang, G. W. Yang, J. B. Li, *ACS Appl. Mater. Interfaces* **2017**, *9*, 43830.

[43] F. Zhang, Z. Wang, J. Dong, A. Nie, J. Xiang, W. Zhu, Z. Liu, C. Tao, *ACS Nano* **2019**, *13*, 8004.

[44] W. Feng, F. Gao, Y. Hu, M. Dai, H. Liu, L. Wang, P. Hu, *ACS Appl. Mater. Interfaces* **2018**, *10*, 27584.

[45] C. Julien, A. Chevy, D. Siapkas, *Phys. Status Solidi A* **1990**, *118*, 553.

[46] Q. Wang, L. Yang, S. Zhou, X. Ye, Z. Wang, W. Zhu, M. D. McCluskey, Y. Gu, *J. Phys. Chem. Lett.* **2017**, *8*, 2887.

[47] a) A. M. Rasmussen, S. T. Teklemichael, E. Mafi, Y. Gu, M. D. McCluskey, *Appl. Phys. Lett.* **2013**, *102*, 062105; b) Y. L. Huang, C. W. Huang, J. Y. Chen, Y. H. Ting, K. C. Lu, Y. L. Chueh, W. W. Wu, *ACS Nano* **2014**, *8*, 9457.

[48] B. Nilanthy, D. S. Elisabeth, F. S. Emily, R. K. Zakhar, D. K. Zakhar, E. Laurence, P. Amalia, H. B. Peter, *2D Mater.* **2018**, *5*, 035026.

[49] C.-H. Ho, Y.-C. Chen, *RSC Adv.* **2013**, *3*, 24896.

[50] C. Shuo, L. Xuemei, Q. Xvsheng, W. Xia, S. Khurram, Z. Xianghua, X. Yang, F. Xianping, *Small* **2017**, *13*, 1604033.

[51] X. Tan, J. Zhou, Q. Yang, *CrystEngComm* **2011**, *13*, 2792.

[52] a) P. Pistor, J. M. M. Alvarez, M. Leon, M. di Michiel, S. Schorr, R. Klenk, S. Lehmann, *Acta Crystallogr., Sect. B: Struct. Sci., Cryst. Eng. Mater.* **2016**, *72*, 410; b) K. H. Park, K. Jang, S. U. Son, *Angew. Chem., Int. Ed.* **2006**, *45*, 4608.

[53] C. Y. Wei, W. Guo, J. Q. Yang, H. M. Fan, J. Zhang, W. J. Zheng, *RSC Adv.* **2014**, *4*, 50456.

[54] a) S. Acharya, M. Dutta, S. Sarkar, D. Basak, S. Chakraborty, N. Pradhan, *Chem. Mater.* **2012**, *24*, 1779; b) W. Huang, L. Gan, H. Yang, N. Zhou, R. Wang, W. Wu, H. Li, Y. Ma, H. Zeng, T. Zhai, *Adv. Funct. Mater.* **2017**, *27*, 1702448.

[55] Y. Tian, L. G. Wang, H. Q. Tang, W. W. Zhou, *J. Mater. Chem. A* **2015**, *3*, 11294.

[56] a) J. D. Yao, Z. X. Deng, Z. Q. Zheng, G. W. Yang, *ACS Appl. Mater. Interfaces* **2016**, *8*, 20872; b) M. Safdar, Z. Wang, M. Mirza, C. Jiang, J. He, *J. Mater. Chem.* **2012**, *22*, 19228; c) P. M. Reshmi, A. G. Kunjomana, K. A. Chandrasekharan, *Cryst. Res. Technol.* **2011**, *46*, 153.

[57] a) M. Safdar, Z. Wang, M. Mirza, F. K. Butt, Y. Wang, L. Sun, J. He, *J. Mater. Chem. A* **2013**, *1*, 1427; b) S. H. Zhang, J. Y. Zhang, B. S. Liu, X. B. Jia, G. F. Wang, H. X. Chang, *Sci. Rep.* **2019**, *9*, 7.

[58] a) P. D. C. King, T. D. Veal, F. Fuchs, C. Y. Wang, D. J. Payne, A. Bourlange, H. Zhang, G. R. Bell, V. Cimalla, O. Ambacher, R. G. Egdell, F. Bechstedt, C. F. McConville, *Phys. Rev. B* **2009**, *79*, 205211; b) A. Walsh, J. L. F. Da Silva, S.-H. Wei, C. Körber, A. Klein, L. F. J. Piper, A. DeMasi, K. E. Smith, G. Panaccione, P. Torelli, D. J. Payne, A. Bourlange, R. G. Egdell, *P R Letters* **2008**, *100*, 167402.

[59] H. Dong, Z. Chen, L. Sun, L. Zhou, Y. Ling, C. Yu, H. H. Tan, C. Jagadish, X. Shen, *J. Phys. Chem. C* **2009**, *113*, 10511.

[60] J. Wang, J. Su, H. Chen, X. Zou, G.-D. Li, *J. Mater. Chem. C* **2018**, *6*, 4156.

**ADVANCED
SCIENCE NEWS**
www.advancedsciencenews.com

**ADVANCED
FUNCTIONAL
MATERIALS**
www.afm-journal.de

[61] a) Y. Cao, X. Huang, Y. Wu, Y.-C. Zou, J. Zhao, G.-D. Li, X. Zou, *RSC Adv.* **2015**, *5*, 60541; b) X. Wang, J. Su, H. Chen, G.-D. Li, Z. Shi, H. Zou, X. Zou, *ACS Appl. Mater. Interfaces* **2017**, *9*, 16335.

[62] a) G. Han, Z.-G. Chen, C. Sun, L. Yang, L. Cheng, Z. Li, W. Lu, Z. M. Gibbs, G. J. Snyder, K. Jack, J. Drennan, J. Zou, *CrystEngComm* **2014**, *16*, 393; b) G. Han, Z. G. Chen, L. Yang, L. Cheng, J. Drennan, J. Zou, *Cryst. Growth Des.* **2013**, *13*, 5092.

[63] G. Han, Z. G. Chen, L. Yang, L. Cheng, K. Jack, J. Drennan, J. Zou, *Appl. Phys. Lett.* **2013**, *103*, 5.

[64] L. Debbichi, O. Eriksson, S. Lebègue, *Ann. Phys.* **2014**, *526*, 402.

[65] a) C. Zhesheng, G. Karim, B. Mohamed, B. Johan, S. Abhay, *Nanotechnology* **2013**, *24*, 415708; b) Y. Zhou, Y. Nie, Y. Liu, K. Yan, J. Hong, C. Jin, Y. Zhou, J. Yin, Z. Liu, H. Peng, *ACS Nano* **2014**, *8*, 1485.

[66] a) H. R. Jappor, M. A. Habeeb, *Curr. Appl. Phys.* **2018**, *18*, 673; b) J. Late Dattatray, B. Liu, J. Luo, A. Yan, H. S. S. R. Matte, M. Grayson, C. N. R. Rao, P. Dravid Vinayak, *Adv. Mater.* **2012**, *24*, 3549; c) P. A. Hu, Z. Z. Wen, L. F. Wang, P. H. Tan, K. Xiao, *ACS Nano* **2012**, *6*, 5988; d) P. Hu, L. Wang, M. Yoon, J. Zhang, W. Feng, X. Wang, Z. Wen, J. C. Idrobo, Y. Miyamoto, D. B. Geohegan, K. Xiao, *Nano Lett.* **2013**, *13*, 1649; e) Y. B. Zhou, B. Deng, Y. Zhou, X. B. Ren, J. B. Yin, C. H. Jin, Z. F. Liu, H. L. Peng, *Nano Lett.* **2016**, *16*, 2103; f) S. Lei, L. Ge, Z. Liu, S. Najmaei, G. Shi, G. You, J. Lou, R. Vajtai, P. M. Ajayan, *Nano Lett.* **2013**, *13*, 2777; g) X. F. Li, M. W. Lin, A. A. Puretzky, J. C. Idrobo, C. Ma, M. F. Chi, M. Yoon, C. M. Rouleau, KravchenkoII, D. B. Geohegan, K. Xiao, *Sci. Rep.* **2014**, *4*, 9; h) M. Mahjouri-Samani, R. Gresback, M. K. Tian, K. Wang, A. A. Puretzky, C. M. Rouleau, G. Eres, I. N. Ivanov, K. Xiao, M. A. McGuire, G. Duscher, D. B. Geohegan, *Adv. Funct. Mater.* **2014**, *24*, 6365; i) Y. Cao, K. Cai, P. Hu, L. Zhao, T. Yan, W. Luo, X. Zhang, X. Wu, K. Wang, H. Zheng, *Sci. Rep.* **2015**, *5*, 8130.

[67] T. Jia, H.-R. Fuh, D. Chen, M. Abid, M. Abid, D. Zhang, B. Sarker Anas, J. Cho, M. Choi, S. Chun Byong, H. Xu, C. Ó Coileáin, H. Liu, C.-R. Chang, H.-C. Wu, *Adv. Electron. Mater.* **2018**, *4*, 1700447.

[68] A. Harvey, C. Backes, Z. Gholamvand, D. Hanlon, D. McAteer, H. C. Nerl, E. McGuire, A. Seral-Ascaso, Q. M. Ramasse, N. McEvoy, S. Winters, N. C. Berner, D. McCloskey, J. F. Donegan, G. S. Duesberg, V. Nicolosi, J. N. Coleman, *Chem. Mater.* **2015**, *27*, 3483.

[69] X. Zhou, J. X. Cheng, Y. B. Zhou, T. Cao, H. Hong, Z. M. Liao, S. W. Wu, H. L. Peng, K. H. Liu, D. P. Yu, *J. Am. Chem. Soc.* **2015**, *137*, 7994.

[70] a) L. Plucinski, R. L. Johnson, B. J. Kowalski, K. Kopalko, B. A. Orlowski, Z. D. Kovalyuk, G. V. Lashkarev, *Phys. Rev. B* **2003**, *68*, 125304; b) W. An, F. Wu, H. Jiang, G. S. Tian, X. Z. Li, *J. Chem. Phys.* **2014**, *141*, 084701.

[71] W. Jie, X. Chen, D. Li, L. Xie, Y. Y. Hui, S. P. Lau, X. Cui, J. Hao, *Angew. Chem., Int. Ed.* **2015**, *54*, 1185.

[72] L. Fang, Q. Yuan, H. Fang, X. Gan, J. Li, T. Wang, Q. Zhao, W. Jie, J. Zhao, *Adv. Opt. Mater.* **2018**, *6*, 1800698.

[73] Y. Yang, H. Du, Q. Xue, X. Wei, Z. Yang, C. Xu, D. Lin, W. Jie, J. Hao, *Nano Energy* **2019**, *57*, 566.

[74] a) H. Cai, B. Chen, G. Wang, E. Soignard, A. Khosravi, M. Manca, X. Marie, S. L. Y. Chang, B. Urbaszek, S. Tongay, *Adv. Mater.* **2017**, *29*, 7; b) A. Gouskov, J. Camassel, L. Gouskov, *Prog. Cryst. Growth Charact. Mater.* **1982**, *5*, 323.

[75] F. Liu, H. Shimotani, H. Shang, T. Kanagasekaran, V. Zólyomi, N. Drummond, V. I. Fal'ko, K. Tanigaki, *ACS Nano* **2014**, *8*, 752.

[76] S. Huang, Y. Tatsumi, X. Ling, H. Guo, Z. Wang, G. Watson, A. A. Puretzky, D. B. Geohegan, J. Kong, J. Li, T. Yang, R. Saito, M. S. Dresselhaus, *ACS Nano* **2016**, *10*, 8964.

[77] J. J. Fonseca, M. K. Horton, K. Tom, J. Yao, W. Walukiewicz, O. D. Dubon, *Chem. Mater.* **2018**, *30*, 4226.

[78] H. Cai, B. Chen, M. Blei, S. L. Y. Chang, K. Wu, H. Zhuang, S. Tongay, *Nat. Commun.* **2018**, *9*, 1927.

[79] Y. W. Yu, M. Ran, S. S. Zhou, R. Y. Wang, F. Y. Zhou, H. Q. Li, L. Gan, M. Q. Zhu, T. Y. Zhai, *Adv. Funct. Mater.* **2019**, *29*, 8.

[80] S. Yoshioka, H. Hayashi, A. Kuwabara, F. Oba, K. Matsunaga, I. Tanaka, *J. Phys.: Condens. Matter* **2007**, *19*, 346211.

[81] L. Dai, X. L. Chen, X. N. Zhang, A. Z. Jin, T. Zhou, B. Q. Hu, Z. Zhang, *J. Appl. Phys.* **2002**, *92*, 1062.

[82] X. Q. Zheng, J. Lee, S. Rafique, L. Han, C. A. Zorman, H. P. Zhao, P. X. L. Feng, in *30th IEEE Int. Conf. on Micro Electro Mechanical Systems*, IEEE, New York **2017**, p. 209.

[83] R. J. Zou, Z. Y. Zhang, Q. Liu, J. Q. Hu, L. W. Sang, M. Y. Liao, W. J. Zhang, *Small* **2014**, *10*, 1848.

[84] H. Yang, R. Shi, J. Yu, R. Liu, R. Zhang, H. Zhao, L. Zhang, H. Zheng, *J. Phys. Chem. C* **2009**, *113*, 21548.

[85] W. Feng, X. Wang, J. Zhang, L. Wang, W. Zheng, P. Hu, W. Cao, B. Yang, *J. Mater. Chem. C* **2014**, *2*, 3254.

[86] Z. R. Dai, Z. W. Pan, Z. L. Wang, *J. Phys. Chem. B* **2002**, *106*, 902.

[87] X. Y. Zhang, Z. Zhang, J. Liang, Y. G. Zhou, Y. C. Tong, Y. Wang, X. X. Wang, *J. Mater. Chem. A* **2017**, *5*, 9702.

[88] Y. Teng, L. X. Song, A. Ponchel, Z. K. Yang, J. Xia, *Adv. Mater.* **2014**, *26*, 6238.

[89] Z. Yang, L. X. Song, Y. Q. Wang, M. M. Ruan, Y. Teng, J. Xia, J. Yang, S. S. Chen, F. Wang, *J. Mater. Chem. A* **2018**, *6*, 2914.

[90] S. B. Patil, I. Y. Kim, J. L. Gunjakar, S. M. Oh, T. Eom, H. Kim, S. J. Hwang, *ACS Appl. Mater. Interfaces* **2015**, *7*, 18679.

[91] S. J. Cui, Z. X. Mei, Y. H. Zhang, H. L. Liang, X. L. Du, *Adv. Opt. Mater.* **2017**, *5*, 1700454.

[92] H. F. Liu, K. K. A. Antwi, N. L. Yakovlev, H. R. Tan, L. T. Ong, S. J. Chua, D. Z. Chi, *ACS Appl. Mater. Interfaces* **2014**, *6*, 3501.

[93] N. Zhou, L. Gan, R. S. Yang, F. K. Wang, L. Li, Y. C. Chen, D. H. Li, T. Y. Zhai, *ACS Nano* **2019**, *13*, 6297.

[94] L. A. Burton, T. J. Whittles, D. Hesp, W. M. Linhart, J. M. Skelton, B. Hou, R. F. Webster, G. O'Dowd, C. Reece, D. Cherns, D. J. Fermin, T. D. Veal, V. R. Dhanak, A. Walsh, *J. Mater. Chem. A* **2016**, *4*, 1312.

[95] a) X. Zhou, Q. Zhang, L. Gan, H. Q. Li, J. Xiong, T. Y. Zhai, *Adv. Sci.* **2016**, *3*, 20; b) C. Chowdhury, S. Karmakar, A. Datta, *J. Phys. Chem. C* **2017**, *121*, 7615.

[96] a) B. Palosz, W. Steurer, H. Schulz, *Acta Crystallogr., Sect. B: Struct. Sci.* **1990**, *46*, 449; b) R. S. Mitchell, Y. Fujiki, Y. Ishizawa, *J. Cryst. Growth* **1982**, *57*, 273; c) R. S. Mitchell, Y. Fujiki, Y. Ishizawa, *Nature* **1974**, *247*, 537.

[97] T. F. Zhou, W. K. Pang, C. F. Zhang, J. P. Yang, Z. X. Chen, H. K. Liu, Z. P. Guo, *ACS Nano* **2014**, *8*, 8323.

[98] J. H. Kim, S. J. Yun, H. S. Lee, J. Zhao, H. Bouzid, Y. H. Lee, *Sci. Rep.* **2018**, *8*, 7.

[99] E. Sutter, Y. Huang, H. P. Komsa, M. Ghorbani-Asl, A. V. Krasheninnikov, P. Sutter, *Nano Lett.* **2016**, *16*, 4410.

[100] L. A. Burton, A. Walsh, *J. Phys. Chem. C* **2012**, *116*, 24262.

[101] I. Y. Ahmet, M. S. Hill, A. L. Johnson, L. M. Peter, *Chem. Mater.* **2015**, *27*, 7680.

[102] W. C. Jin, S. Vishwanath, J. P. Liu, L. Y. Kong, R. Lou, Z. W. Dai, J. T. Sadowski, X. Y. Liu, H. H. Lien, A. Chaney, Y. M. Han, M. Cao, J. Z. Ma, T. Qian, S. C. Wang, M. Dobrowolska, J. Furdyna, D. A. Muller, K. Pohl, H. Ding, J. I. Dadap, H. G. Xing, R. M. Osgood, *Phys. Rev. X* **2017**, *7*, 9.

[103] J. R. Brent, D. J. Lewis, T. Lorenz, E. A. Lewis, N. Savjani, S. J. Haigh, G. Seifert, B. Derby, P. O'Brien, *J. Am. Chem. Soc.* **2015**, *137*, 12689.

[104] J. M. Gonzalez, I. I. Oleynik, *Phys. Rev. B* **2016**, *94*, 125443.

[105] P. Yu, X. C. Yu, W. L. Lu, H. Lin, L. F. Sun, K. Z. Du, F. C. Liu, W. Fu, Q. S. Zeng, Z. X. Shen, C. H. Jin, Q. J. Wang, Z. Liu, *Adv. Funct. Mater.* **2016**, *26*, 137.

[106] E. Lifshitz, Z. Chen, L. Bykov, *J. Phys. Chem.* **1993**, *97*, 238.

[107] C. Bacaksiz, S. Cahangirov, A. Rubio, R. T. Senger, F. M. Peeters, H. Sahin, *Phys. Rev. B* **2016**, *93*, 125403.

ADVANCED
SCIENCE NEWS
www.advancedsciencenews.com

ADVANCED
FUNCTIONAL
MATERIALS
www.afm-journal.de

[108] Y. Huang, E. Sutter, J. T. Sadowski, M. Cotlet, O. L. A. Monti, D. A. Racke, M. R. Neupane, D. Wickramaratne, R. K. Lake, B. A. Parkinson, P. Sutter, *ACS Nano* **2014**, *8*, 10743.

[109] H. S. Song, S. L. Li, L. Gao, Y. Xu, K. Ueno, J. Tang, Y. B. Cheng, K. Tsukagoshi, *Nanoscale* **2013**, *5*, 9666.

[110] A. Shafique, A. Samad, Y.-H. Shin, *Phys. Chem. Chem. Phys.* **2017**, *19*, 20677.

[111] J. Li, J. Shen, Z. Ma, K. Wu, *Sci. Rep.* **2017**, *7*, 8914.

[112] J. Z. Ou, W. Ge, B. Carey, T. Daeneke, A. Rotbart, W. Shan, Y. Wang, Z. Fu, A. F. Chrimes, W. Wlodarski, S. P. Russo, Y. X. Li, K. Kalantar-zadeh, *ACS Nano* **2015**, *9*, 10313.

[113] Y. P. Du, Z. Y. Yin, X. H. Rui, Z. Y. Zeng, X. J. Wu, J. Q. Liu, Y. Y. Zhu, J. X. Zhu, X. Huang, Q. Y. Yan, H. Zhang, *Nanoscale* **2013**, *5*, 1456.

[114] J. W. Seo, J. T. Jang, S. W. Park, C. J. Kim, B. W. Park, J. W. Cheon, *Adv. Mater.* **2008**, *20*, 4269.

[115] a) B. Qu, C. Ma, G. Ji, C. Xu, J. Xu, Y. S. Meng, T. Wang, J. Y. Lee, *Adv. Mater.* **2014**, *26*, 3854; b) B. Luo, Y. Fang, B. Wang, J. S. Zhou, H. H. Song, L. J. Zhi, *Energy Environ. Sci.* **2012**, *5*, 5226; c) Z. J. Zhang, H. L. Zhao, J. J. Fang, X. W. Chang, Z. L. Li, L. N. Zhao, *ACS Appl. Mater. Interfaces* **2018**, *10*, 28533.

[116] G. Wang, J. Peng, L. Zhang, J. Zhang, B. Dai, M. Zhu, L. Xia, F. Yu, *J. Mater. Chem. A* **2015**, *3*, 3659.

[117] H. Zhong, G. Yang, H. Song, Q. Liao, H. Cui, P. Shen, C.-X. Wang, *J. Phys. Chem. C* **2012**, *116*, 9319.

[118] X. S. Wang, Z. W. Wang, J. D. Zhang, X. Wang, Z. P. Zhang, J. L. Wang, Z. H. Zhu, Z. Y. Li, Y. Liu, X. F. Hu, J. W. Qiu, G. H. Hu, B. Chen, N. Wang, Q. Y. He, J. Z. Chen, J. X. Yan, W. Zhang, T. Hasan, S. Z. Li, H. Li, H. Zhang, Q. Wang, X. Huang, W. Huang, *Nat. Commun.* **2018**, *9*, 11.

[119] H. W. Chen, Y. T. Chen, H. Zhang, D. W. Zhang, P. Zhou, J. Huang, *Adv. Funct. Mater.* **2018**, *28*, 8.

[120] X. Zhou, Q. Zhang, L. Gan, H. Q. Li, T. Y. Zhai, *Adv. Funct. Mater.* **2016**, *26*, 4405.

[121] G. L. Ye, Y. J. Gong, S. D. Lei, Y. M. He, B. Li, X. Zhang, Z. H. Jin, L. L. Dong, J. Lou, R. Vajtai, W. Zhou, P. M. Ajayan, *Nano Res.* **2017**, *10*, 2386.

[122] a) R. J. Chang, H. J. Tan, X. C. Wang, B. Porter, T. X. Chen, Y. W. Sheng, Y. Q. Zhou, H. F. Huang, H. Bhaskaran, J. H. Warner, *ACS Appl. Mater. Interfaces* **2018**, *10*, 13002; b) X. Jia, C. Tang, R. Pan, Y. Long, C. Gu, J. Li, *ACS Appl. Mater. Interfaces* **2018**, *10*, 18073; c) H. D. Zhang, Y. Balaji, A. N. Mehta, M. Heyns, M. Caymax, I. Radu, W. Vandervorst, A. Delabie, *J. Mater. Chem. C* **2018**, *6*, 6172.

[123] G. Su, V. G. Hadjiev, P. E. Loya, J. Zhang, S. Lei, S. Maharjan, P. Dong, P. M. Ajayan, J. Lou, H. Peng, *Nano Lett.* **2015**, *15*, 506.

[124] G. B. Liu, Z. H. Li, X. S. Chen, W. Zheng, W. Feng, M. J. Dai, D. C. Jia, Y. Zhou, P. A. Hu, *Nanoscale* **2017**, *9*, 9167.

[125] a) G. L. Shao, X. X. Xue, X. L. Zhou, J. Xu, Y. Y. Jin, S. Y. Qi, N. Liu, H. G. Duan, S. S. Wang, S. S. Li, M. Ouzounian, T. S. Hu, J. Luo, S. Liu, Y. X. Feng, *ACS Nano* **2019**, *13*, 8265; b) R. J. Chang, Y. W. Sheng, T. X. Chen, N. Mkhize, Y. Lu, H. Bhaskaran, J. H. Warner, *ACS Appl. Nano Mater.* **2019**, *2*, 4222.

[126] a) J.-H. Ahn, M.-J. Lee, H. Heo, J. H. Sung, K. Kim, H. Hwang, M.-H. Jo, *Nano Lett.* **2015**, *15*, 3703; b) N. Lee, G. Lee, H. Choi, H. Park, Y. Choi, H. Seo, H. Ju, S. Kim, O. Sul, J. Lee, S. B. Lee, H. Jeon, *Nanotechnology* **2019**, *30*, 9; c) M. Mattinen, P. J. King, L. Khriachtchev, K. Meinander, J. T. Gibbon, V. R. Dhanak, J. Raisanen, M. Ritala, M. Leskela, *Small* **2018**, *14*, 1800547; d) W. J. Liu, M. L. Liu, X. T. Wang, T. Shen, G. Q. Chang, M. Lei, H. X. Deng, Z. M. Wei, Z. Y. Wei, *ACS Appl. Nano Mater.* **2019**, *2*, 2697.

[127] B. Giri, M. Masroor, T. Yan, K. Kushnir, A. D. Carl, C. Doiron, H. C. Zhang, Y. Y. Zhao, A. McClelland, G. A. Tompsett, D. W. Wang, R. L. Grimm, L. V. Titova, P. M. Rao, *Adv. Energy Mater.* **2019**, *9*, 1901236.

[128] L. X. Meng, S. Y. Wang, F. R. Cao, W. Tian, R. Long, L. Li, *Angew. Chem., Int. Ed.* **2019**, *58*, 6761.

[129] T. Sriv, K. Kim, H. Cheong, *Sci. Rep.* **2018**, *8*, 10194.

[130] L. Lee, C. W. Chen, A. Manikandan, S. H. Lee, Z. M. M. Wang, Y. L. Chueh, *Nano Energy* **2018**, *44*, 419.

[131] X. Zhou, L. Gan, W. M. Tian, Q. Zhang, S. Y. Jin, H. Q. Li, Y. Bando, D. Golberg, T. Y. Zhai, *Adv. Mater.* **2015**, *27*, 8035.

[132] W. Zhou, Z. Yu, H. Song, R. Fang, Z. Wu, L. Li, Z. Ni, W. Ren, L. Wang, S. Ruan, *Phys. Rev. B* **2017**, *96*, 035401.

[133] Y. B. Luo, Y. Zheng, Z. Z. Luo, S. Q. Hao, C. F. Du, Q. H. Liang, Z. Li, K. A. Khor, K. Hippalgaonkar, J. W. Xu, Q. Y. Yan, C. Wolverton, M. G. Kanatzidis, *Adv. Energy Mater.* **2018**, *8*, 6.

[134] D. Zou, C. Yu, Y. Li, Y. Ou, Y. Gao, *R. Soc. Open Sci.* **2018**, *5*, 171827.

[135] P. Ramasamy, P. Manivasakan, J. Kim, *CrystEngComm* **2015**, *17*, 807.

[136] a) C. L. Zhang, H. H. Yin, M. Han, Z. H. Dai, H. Pang, Y. L. Zheng, Y. Q. Lan, J. C. Bao, J. M. Zhu, *ACS Nano* **2014**, *8*, 3761; b) Y. Zhang, Y. Liu, K. H. Lim, C. C. Xing, M. Y. Li, T. Zhang, P. Y. Tang, J. Arbiol, J. Llorca, K. M. Ng, M. Ibanez, P. Guardia, M. Prato, D. Cadavid, A. Cabot, *Angew. Chem., Int. Ed.* **2018**, *57*, 17063.

[137] S. Saha, A. Banik, K. Biswas, *Chem. - Eur. J.* **2016**, *22*, 15634.

[138] a) F. Zhang, C. Xia, J. Zhu, B. Ahmed, H. Liang, D. B. Velusamy, U. Schwingenschlögl, H. N. Alshareef, *Adv. Energy Mater.* **2016**, *6*, 1601188; b) H. W. Chen, B. E. Jia, X. S. Lu, Y. C. Guo, R. Hu, R. Khatoon, L. Jiao, J. X. Leng, L. Q. Zhang, J. G. Lu, *Chem. - Eur. J.* **2019**, *25*, 9973.

[139] a) J. Choi, J. Jin, I. G. Jung, J. M. Kim, H. J. Kim, S. U. Son, *Chem. Commun.* **2011**, *47*, 5241; b) S. Kim, Z. P. Yao, J. M. Lim, M. C. Hersam, C. Wolverton, V. P. Dravid, K. He, *Adv. Mater.* **2018**, *30*, 10.

[140] a) Y. H. Zhou, B. W. Zhang, X. L. Chen, C. C. Gu, C. An, Y. Zhou, K. M. Cai, Y. F. Yuan, C. H. Chen, H. Wu, R. R. Zhang, C. Y. Park, Y. M. Xiong, X. W. Zhang, K. Y. Wang, Z. R. Yang, *Adv. Electron. Mater.* **2018**, *4*, 7; b) J. W. Zeng, E. Liu, Y. J. Fu, Z. Y. Chen, C. Pan, C. Y. Wang, M. Wang, Y. J. Wang, K. Xu, S. H. Cai, X. X. Yan, Y. Wang, X. W. Liu, P. Wang, S. J. Liang, Y. Cui, H. Y. Hwang, H. T. Yuan, F. Miao, *Nano Lett.* **2018**, *18*, 1410.

[141] a) Y. P. Song, X. W. Liang, J. G. Guo, J. Deng, G. Y. Gao, X. L. Chen, *Phys. Rev. Mater.* **2019**, *3*, 7; b) H. L. Wu, S. Li, M. Susner, S. Kwon, M. Kim, T. Haugan, B. Lv, *2D Mater.* **2019**, *6*, 8.

[142] B. Ul Haq, S. AlFaify, R. Ahmed, F. K. Butt, A. Laref, M. Shkir, *Phys. Rev. B* **2018**, *97*, 12.

[143] J. D. Dwyer, E. J. Diaz, T. E. Webber, A. Katzenberg, M. A. Modestino, E. S. Aydil, *Nanotechnology* **2019**, *30*, 245705.

[144] L. Wu, Z. Xie, L. Lu, J. Zhao, Y. Wang, X. Jiang, Y. Ge, F. Zhang, S. Lu, Z. Guo, J. Liu, Y. Xiang, S. Xu, J. Li, D. Fan, H. Zhang, *Adv. Opt. Mater.* **2018**, *6*, 1700985.

[145] Z. Tian, C. L. Guo, M. X. Zhao, R. R. Li, J. M. Xue, *ACS Nano* **2017**, *11*, 2219.

[146] L. Huang, F. G. Wu, J. B. Li, *J. Chem. Phys.* **2016**, *144*, 114708.

[147] Y. Guo, S. Zhou, Y. Z. Bai, J. J. Zhao, *ACS Appl. Mater. Interfaces* **2017**, *9*, 12013.

[148] X. X. Zhao, J. Kotakoski, J. C. Meyer, E. Sutter, P. Sutter, A. V. Krasheninnikov, U. Kaiser, W. Zhou, *MRS Bull.* **2017**, *42*, 667.

[149] P. Sutter, H. P. Komsa, A. V. Krasheninnikov, Y. Huang, E. Sutter, *Appl. Phys. Lett.* **2017**, *111*, 262102.

[150] Z. Tian, M. X. Zhao, X. X. Xue, W. Xia, C. L. Guo, Y. F. Guo, Y. X. Feng, J. M. Xue, *ACS Appl. Mater. Interfaces* **2018**, *10*, 12831.

[151] L. Li, Z. Chen, Y. Hu, X. W. Wang, T. Zhang, W. Chen, Q. B. Wang, *J. Am. Chem. Soc.* **2013**, *135*, 1213.

[152] Y. J. Zhang, J. Lu, S. L. Shen, H. R. Xu, Q. B. Wang, *Chem. Commun.* **2011**, *47*, 5226.

[153] F. Li, M. M. Ramin Moayed, E. Klein, R. Lesyuk, C. Klinke, *J. Phys. Chem. Lett.* **2019**, *10*, 993.

[154] a) G. Han, S. R. Popuri, H. F. Greer, J. W. G. Bos, W. Z. Zhou, A. R. Knox, A. Montecucco, J. Siviter, E. A. Man, M. Macauley,

D. J. Paul, W. G. Li, M. C. Paul, M. Gao, T. Sweet, R. Freer, F. Azough, H. Baig, N. Sellami, T. K. Mallick, D. H. Gregory, *Angew. Chem., Int. Ed.* **2016**, *55*, 6433; b) H. Q. Yang, X. Y. Wang, H. Wu, B. Zhang, D. D. Xie, Y. J. Chen, X. Lu, X. D. Han, L. Miao, X. Y. Zhou, *J. Mater. Chem. C* **2019**, *7*, 3351.

[155] S. L. Zhao, H. A. Wang, Y. Zhou, L. Liao, Y. Jiang, X. Yang, G. C. Chen, M. Lin, Y. Wang, H. L. Peng, Z. F. Liu, *Nano Res.* **2015**, *8*, 288.

[156] G. Liu, Y. Li, B. Li, H. Tian, C. Fan, Y. Zhang, Z. Hua, M. Wang, H. Zheng, E. Li, *J. Mater. Chem. C* **2018**, *6*, 10036.

[157] a) P. Zhao, H. C. Yang, J. W. Li, H. Jin, W. Wei, L. Yu, B. B. Huang, Y. Dai, *J. Mater. Chem. A* **2017**, *5*, 24145; b) L. C. Gomes, A. Carvalho, *Phys. Rev. B* **2015**, *92*, 085406.

[158] S. Luo, X. Qi, H. Yao, X. Ren, Q. Chen, J. Zhong, *J. Phys. Chem. C* **2017**, *121*, 4674.

[159] J. Xia, X.-Z. Li, X. Huang, N. Mao, D.-D. Zhu, L. Wang, H. Xu, X.-M. Meng, *Nanoscale* **2016**, *8*, 2063.

[160] Y. Bao, P. Song, Y. Liu, Z. Chen, M. Zhu, I. Abdelwahab, J. Su, W. Fu, X. Chi, W. Yu, W. Liu, X. Zhao, Q.-H. Xu, M. Yang, K. P. Loh, *Nano Lett.* **2019**, *19*, 5109.

[161] E. Sutter, J. Wang, P. Sutter, *Chem. Mater.* **2019**, *31*, 2563.

[162] A. Dewandre, O. Hellman, S. Bhattacharya, A. H. Romero, G. K. H. Madsen, M. J. Verstraete, *Phys. Rev. Lett.* **2016**, *117*, 6.

[163] a) Z. T. Deng, D. R. Han, Y. Liu, *Nanoscale* **2011**, *3*, 4346; b) E. C. Greyson, J. E. Barton, T. W. Odom, *Small* **2006**, *2*, 368.

[164] Z. Deng, D. Cao, J. He, S. Lin, S. M. Lindsay, Y. Liu, *ACS Nano* **2012**, *6*, 6197.

[165] F. Li, M. M. Ramin Moayed, F. Gerdes, S. Kull, E. Klein, R. Lesyuk, C. Klinke, *J. Mater. Chem. C* **2018**, *6*, 9410.

[166] J. O. Dimmock, I. Melngailis, A. J. Strauss, *Phys. Rev. Lett.* **1966**, *16*, 1193.

[167] K. Chang, J. Liu, H. Lin, N. Wang, K. Zhao, A. Zhang, F. Jin, Y. Zhong, X. Hu, W. Duan, Q. Zhang, L. Fu, Q.-K. Xue, X. Chen, S.-H. Ji, *Science* **2016**, *353*, 274.

[168] S. Barraza-Lopez, T. P. Kaloni, S. P. Poudel, P. Kumar, *Phys. Rev. B* **2018**, *97*, 14.

[169] a) R. X. Fei, W. B. Li, J. Li, L. Yang, *Appl. Phys. Lett.* **2015**, *107*, 5; b) M. Mehboudi, B. M. Fregoso, Y. Yang, W. Zhu, A. van der Zande, J. Ferrer, L. Bellaiche, P. Kumar, S. Barraza-Lopez, *Phys. Rev. Lett.* **2016**, *117*, 5; c) L. C. Gomes, A. Carvalho, A. H. C. Neto, *Phys. Rev. B* **2015**, *92*, 8.

[170] F. Li, X. H. Liu, Y. Wang, Y. F. Li, *J. Mater. Chem. C* **2016**, *4*, 2155.

[171] F. O. von Rohr, H. W. Ji, F. A. Cevallos, T. Gao, N. P. Ong, R. J. Cava, *J. Am. Chem. Soc.* **2017**, *139*, 2771.

[172] Y. F. Xu, H. Zhang, H. Z. Shao, G. Ni, J. Li, H. L. Lu, R. J. Zhang, B. Peng, Y. Y. Zhu, H. Y. Zhu, C. M. Soukoulis, *Phys. Rev. B* **2017**, *96*, 11.

[173] H. L. Yu, Y. Chen, *J. Phys. Chem. C* **2018**, *122*, 15673.

[174] H. L. Kagdada, P. K. Jha, P. Spiewak, K. J. Kurzydlowski, *Phys. Rev. B* **2018**, *97*, 10.

[175] G. Shi, E. Kioupakis, *Nano Lett.* **2015**, *15*, 6926.

[176] Y. H. Hu, S. L. Zhang, S. F. Sun, M. Q. Xie, B. Cai, H. B. Zeng, *Appl. Phys. Lett.* **2015**, *107*, 4.

[177] H. Q. Zhao, Y. L. Mao, X. Mao, X. Shi, C. S. Xu, C. X. Wang, S. M. Zhang, D. H. Zhou, *Adv. Funct. Mater.* **2018**, *28*, 10.

[178] R. K. Ulaganathan, Y.-Y. Lu, C.-J. Kuo, S. R. Tamalampudi, R. Sankar, K. M. Boopathi, A. Anand, K. Yadav, R. J. Mathew, C.-R. Liu, F. C. Chou, Y.-T. Chen, *Nanoscale* **2016**, *8*, 2284.

[179] D. Z. Tan, H. E. Lim, F. J. Wang, N. B. Mohamed, S. Mouri, W. J. Zhang, Y. Miyauchi, M. Ohfuchi, K. Matsuda, *Nano Res.* **2017**, *10*, 546.

[180] D. Lam, K. S. Chen, J. Kang, X. L. Liu, M. C. Hersam, *Chem. Mater.* **2018**, *30*, 2245.

[181] Y. Ye, Q. Guo, X. Liu, C. Liu, J. Wang, Y. Liu, J. Qiu, *Chem. Mater.* **2017**, *29*, 8361.

[182] X. T. Wang, Y. Y. Li, L. Huang, X. W. Jiang, L. Jiang, H. L. Dong, Z. M. Wei, J. B. Li, W. P. Hu, *J. Am. Chem. Soc.* **2017**, *139*, 14976.

[183] X. Zhou, X. Hu, B. Jin, J. Yu, K. Liu, H. Li, T. Zhai, **2018**, *5*, 1800478.

[184] J. Liu, Y. Zhou, Y. Lin, M. Li, H. Cai, Y. Liang, M. Liu, Z. Huang, F. Lai, F. Huang, W. Zheng, *ACS Appl. Mater. Interfaces* **2019**, *11*, 4123.

[185] Y. Yang, S.-C. Liu, Y. Wang, M. Long, C.-M. Dai, S. Chen, B. Zhang, Z. Sun, Z. Sun, C. Hu, S. Zhang, L. Tong, G. Zhang, D.-J. Xue, J.-S. Hu, *Adv. Opt. Mater.* **2019**, *7*, 1801311.

[186] a) D. D. Vaughn, R. J. Patel, M. A. Hickner, R. E. Schaak, *J. Am. Chem. Soc.* **2010**, *132*, 15170; b) P. Ramasamy, D. Kwak, D. H. Lim, H. S. Ra, J. S. Lee, *J. Mater. Chem. C* **2016**, *4*, 479.

[187] M. R. Buck, A. J. Biacchi, E. J. Popczun, R. E. Schaak, *Chem. Mater.* **2013**, *25*, 2163.

[188] a) E. Sutter, B. Zhang, M. H. Sun, P. Sutter, *ACS Nano* **2019**, *13*, 9352; b) C. Li, L. Huang, G. P. Snigdha, Y. F. Yu, L. Y. Cao, *ACS Nano* **2012**, *6*, 8868; c) C. Y. Lan, C. Li, Y. Yin, H. Y. Guo, S. Wang, *J. Mater. Chem. C* **2015**, *3*, 8074.

[189] X. Hu, P. Huang, K. Liu, B. Jin, X. Zhang, X. Zhang, X. Zhou, T. Zhai, *ACS Appl. Mater. Interfaces* **2019**, *11*, 23353.

[190] W. Wan, C. Liu, W. Xiao, Y. Yao, *Appl. Phys. Lett.* **2017**, *111*, 132904.

[191] G. Bruns, P. Merkelbach, C. Schlockermann, M. Salinga, M. Wuttig, T. D. Happ, J. B. Philipp, M. Kund, *Appl. Phys. Lett.* **2009**, *95*, 043108.

[192] M. Kupers, P. M. Konze, S. Maintz, S. Steinberg, A. M. Mio, O. Cojocaru-Miredin, M. Zhu, M. Muller, M. Luysberg, J. Mayer, M. Wuttig, R. Dronskowski, *Angew. Chem., Int. Ed.* **2017**, *56*, 10204.

[193] a) D. E. Aspnes, J. C. Phillips, K. L. Tai, P. M. Bridenbaugh, *Phys. Rev. B* **1981**, *23*, 816; b) L. Properzi, A. Di Cicco, L. Nataf, F. Baudelet, T. Irifune, *Sci. Rep.* **2015**, *5*, 9.

[194] L. Chen, P. J. Klar, W. Heimbrodt, N. Oberender, D. Kempe, M. Froba, *Appl. Phys. Lett.* **2000**, *77*, 3965.

[195] M. Fuentes-Cabrera, H. Wang, O. F. Sankey, *J. Phys.: Condens. Matter* **2002**, *14*, 9589.

[196] Y. S. Yang, S. C. Liu, W. Yang, Z. B. Li, Y. Wang, X. Wang, S. S. Zhang, Y. Zhang, M. S. Long, G. M. Zhang, D. J. Xue, J. S. Hu, L. J. Wan, *J. Am. Chem. Soc.* **2018**, *140*, 4150.

[197] X. Zhou, X. Hu, S. Zhou, Q. Zhang, H. Li, T. Zhai, *Adv. Funct. Mater.* **2017**, *27*, 1703858.

[198] B. Mukherjee, E. S. Tok, C. H. Sow, *J. Appl. Phys.* **2013**, *114*, 10.

[199] B. Mukherjee, Z. B. Hu, M. R. Zheng, Y. Q. Cai, Y. P. Feng, E. S. Tok, C. H. Sow, *J. Mater. Chem.* **2012**, *22*, 24882.

[200] Y. Yan, W. Xiong, S. Li, K. Zhao, X. Wang, J. Su, X. Song, X. Li, S. Zhang, H. Yang, X. Liu, L. Jiang, T. Zhai, C. Xia, J. Li, Z. Wei, **2019**, *7*, 1900622.

[201] Y. Yang, S.-C. Liu, X. Wang, Z. Li, Y. Zhang, G. Zhang, D.-J. Xue, J.-S. Hu, *Adv. Funct. Mater.* **2019**, *29*, 1900411.

[202] K. Cao, D. Ferizovic, M. Munoz, *J. Appl. Phys.* **2008**, *104*, 5.

[203] J. J. Wang, I. Ronneberger, L. Zhou, L. Lu, V. L. Deringer, B. Y. Zhang, L. Tian, H. C. Du, C. L. Jia, X. F. Qian, M. Wuttig, R. Mazzarello, W. Zhang, *Nanoscale* **2018**, *10*, 7363.

[204] X. L. Zhou, D. W. He, S. M. Wang, H. K. Wang, J. Z. Zhang, Y. S. Zhao, *J. Appl. Phys.* **2013**, *113*, 5.

[205] a) S. Acharya, B. Das, U. Thupakula, K. Ariga, D. D. Sarma, J. Israelachvili, Y. Golan, *Nano Lett.* **2013**, *13*, 409; b) C. Schliehe, B. H. Juarez, M. Pelletier, S. Jander, D. Greshnykh, M. Nagel, A. Meyer, S. Foerster, A. Kornowski, C. Klinke, H. Weller, *Science* **2010**, *329*, 550.

[206] T. Bielewicz, E. Klein, C. Klinke, *Nanotechnology* **2016**, *27*, 355602.

[207] T. Bielewicz, S. Dogan, C. Klinke, *Small* **2015**, *11*, 826.

[208] T. Bielewicz, M. M. Ramin Moayed, V. Lebedeva, C. Strelow, A. Rieckmann, C. Klinke, *Chem. Mater.* **2015**, *27*, 8248.

[209] M. M. Ramin Moayed, T. Bielewicz, H. Noei, A. Stierle, C. Klinke, *Adv. Funct. Mater.* **2018**, *28*, 1706815.

**ADVANCED
SCIENCE NEWS**
www.advancedsciencenews.com

**ADVANCED
FUNCTIONAL
MATERIALS**
www.afm-journal.de

[210] M. M. R. Moayed, T. Bielewicz, M. S. Zollner, C. Herrmann, C. Klinke, *Nat. Commun.* **2017**, *8*, 7.

[211] G. B. Bhandari, K. Subedi, Y. F. He, Z. F. Jiang, M. Leopold, N. Reilly, H. P. Lu, A. T. Zayak, L. F. Sun, *Chem. Mater.* **2014**, *26*, 5433.

[212] A. D. Antu, Z. F. Jiang, S. M. Premathilka, Y. T. Tang, J. J. Hu, A. Roy, L. F. Sun, *Chem. Mater.* **2018**, *30*, 3697.

[213] H. T. Zhang, B. H. Savitzky, J. Yang, J. T. Newman, K. A. Perez, B. R. Hyun, L. F. Kourkoutis, T. Hanrath, F. W. Wise, *Chem. Mater.* **2016**, *28*, 127.

[214] A. H. Khan, R. Brescia, A. Polovitsyn, I. Angeloni, B. Martin-Garcia, I. Moreels, *Chem. Mater.* **2017**, *29*, 2883.

[215] A. H. Khan, S. Pal, A. Dalui, J. Pradhan, D. D. Sarma, S. Acharya, *Chem. Mater.* **2017**, *29*, 1175.

[216] Q. A. Akkerman, B. Martín-García, J. Buha, G. Almeida, S. Toso, S. Marras, F. Bonaccorso, U. Petralanda, I. Infante, L. Manna, *Chem. Mater.* **2019**, *31*, 8145.

[217] W.-K. Koh, N. K. Dandu, A. F. Fidler, V. I. Klimov, J. M. Pietryga, S. V. Kilina, *J. Am. Chem. Soc.* **2017**, *139*, 2152.

[218] T. Galle, M. Samadi Khoshkhoo, B. Martin-Garcia, C. Meerbach, V. Sayevich, A. Koitzsch, V. Lesnyak, A. Eychmüller, *Chem. Mater.* **2019**, *31*, 3803.

[219] Z. Zhu, J. Guan, D. Liu, D. Tománek, *ACS Nano* **2015**, *9*, 8284.

[220] J. H. Yang, Y. Y. Zhang, W. J. Yin, X. G. Gong, B. I. Yakobson, S. H. Wei, *Nano Lett.* **2016**, *16*, 1110.

[221] J.-H. Yang, Q. Yuan, H. Deng, S.-H. Wei, B. I. Yakobson, *J. Phys. Chem. C* **2017**, *121*, 123.

[222] S. Karmakar, C. Chowdhury, A. Datta, *J. Phys. Chem. C* **2016**, *120*, 14522.

[223] Y. L. Mao, J. Ben, J. M. Yuan, J. X. Zhong, *Chem. Phys. Lett.* **2018**, *705*, 12.

[224] Y. Chen, Q. Sun, P. Jena, *J. Mater. Chem. C* **2016**, *4*, 6353.

[225] Q. Wang, R. Quhe, Z. Guan, L. Wu, J. Bi, P. Guan, M. Lei, P. Lu, *RSC Adv.* **2018**, *8*, 21280.

[226] R. Juneja, T. Pandey, A. K. Singh, *Chem. Mater.* **2017**, *29*, 3723.

[227] a) J. Kwak, K. Thiyagarajan, A. Giri, U. Jeong, *J. Mater. Chem. C* **2019**, *7*, 10561; b) S. Keuleyan, M. J. Wang, F. R. Chung, J. Commons, K. J. Koski, *Nano Lett.* **2015**, *15*, 2285.

[228] V. L. Johnson, A. Anilao, K. J. Koski, *Nano Res.* **2019**, *12*, 2373.

[229] M. J. Wang, G. Lahti, D. Williams, K. J. Koski, *ACS Nano* **2018**, *12*, 6163.

[230] M. H. Wu, S. H. Wei, L. Huang, *Phys. Rev. B* **2017**, *96*, 6.

[231] R. Haleoot, C. Paillard, T. P. Kaloni, M. Mehboudi, B. Xu, L. Bellaiche, S. Barraza-Lopez, *Phys. Rev. Lett.* **2017**, *118*, 6.

[232] A. K. Singh, B. C. Revard, R. Ramanathan, M. Ashton, F. Tavazza, R. G. Hennig, *Phys. Rev. B* **2017**, *95*, 155426.

[233] C. L. Kane, E. J. Mele, *Phys. Rev. Lett.* **2005**, *95*, 4.

[234] Z. C. Gu, X. G. Wen, *Phys. Rev. B* **2009**, *80*, 23.

[235] F. Pollmann, E. Berg, A. M. Turner, M. Oshikawa, *Phys. Rev. B* **2012**, *85*, 9.

[236] X. Chen, Z. X. Liu, X. G. Wen, *Phys. Rev. B* **2011**, *84*, 13.

[237] a) F. D. Hardcastle, I. E. Wachs, *J. Solid State Chem.* **1992**, *97*, 319; b) N. Cornei, N. Tancret, F. Abraham, O. Mentré, *Inorg. Chem.* **2006**, *45*, 4886.

[238] Y. D. Shen, Y. W. Li, W. M. Li, J. Z. Zhang, Z. G. Hu, J. H. Chu, *J. Phys. Chem. C* **2012**, *116*, 3449.

[239] S. Schmidt, E. T. Kubaski, D. P. Volanti, T. Sequinel, V. D. N. Bezzon, A. Beltrán, S. M. Tebcherani, J. A. Varela, *Inorg. Chem.* **2015**, *54*, 10184.

[240] D. Xie, Q. M. Su, J. Zhang, G. H. Du, B. S. Xu, *J. Mater. Sci.* **2014**, *49*, 218.

[241] K. A. Messalea, B. J. Carey, A. Jannat, N. Syed, M. Mohiuddin, B. Y. Zhang, A. Zavabeti, T. Ahmed, N. Mahmood, E. Della Gaspera, K. Khoshmanesh, K. Kalantar-Zadeh, T. Daeneke, *Nanoscale* **2018**, *10*, 15615.

[242] H. Liu, M. Luo, J. C. Hu, T. F. Zhou, R. Chen, J. L. Li, *Appl. Catal., B* **2013**, *140–141*, 141.

[243] Y. Wang, L. X. Jiang, D. Tang, F. Y. Liu, Y. Q. Lai, *RSC Adv.* **2015**, *5*, 65591.

[244] H. B. Zheng, H. D. Li, M. H. Yu, M. Zhang, Y. X. Tong, F. L. Cheng, X. H. Lu, *J. Mater. Chem. A* **2017**, *5*, 25539.

[245] S. Z. Zheng, Y. Fu, L. J. Zheng, Z. Y. Zhu, J. Chen, Z. Q. Niu, D. C. Yang, *J. Mater. Chem. A* **2019**, *7*, 5530.

[246] M. Yang, Y. Z. Luo, M. G. Zeng, L. Shen, Y. H. Lu, J. Zhou, S. J. Wang, I. K. Sou, Y. P. Feng, *Phys. Chem. Chem. Phys.* **2017**, *19*, 29372.

[247] H. Zhang, J. Huang, X. Zhou, X. Zhong, *Inorg. Chem.* **2011**, *50*, 7729.

[248] G. H. Chen, Y. Q. Yu, K. Zheng, T. Ding, W. L. Wang, Y. Jiang, Q. Yang, *Small* **2015**, *11*, 2848.

[249] a) R. M. Clark, J. C. Kotsakidis, B. Weber, K. J. Berean, B. J. Carey, M. R. Field, H. Khan, J. Z. Ou, T. Ahmed, C. J. Harrison, I. S. Cole, K. Latham, K. Kalantar-zadeh, T. Daeneke, *Chem. Mater.* **2016**, *28*, 8942; b) W. Huang, C. Xing, Y. Wang, Z. Li, L. Wu, D. Ma, X. Dai, Y. Xiang, J. Li, D. Fan, H. Zhang, *Nanoscale* **2018**, *10*, 2404.

[250] W. Luo, F. Li, Q. Li, X. Wang, W. Yang, L. Zhou, L. Mai, *ACS Appl. Mater. Interfaces* **2018**, *10*, 7201.

[251] M. B. Nielsen, P. Parisiades, S. R. Madsen, M. Bremholm, *Dalton Trans.* **2015**, *44*, 14077.

[252] Y. Sun, H. Cheng, S. Gao, Q. Liu, Z. Sun, C. Xiao, C. Wu, S. Wei, Y. Xie, *J. Am. Chem. Soc.* **2012**, *134*, 20294.

[253] M. K. Jana, K. Biswas, C. N. R. Rao, *Chem. - Eur. J.* **2013**, *19*, 9110.

[254] M. Hong, Z. G. Chen, L. Yang, G. Han, J. Zou, *Adv. Electron. Mater.* **2015**, *1*, 9.

[255] H. Xie, Z. Li, Z. Sun, J. Shao, X.-F. Yu, Z. Guo, J. Wang, Q. Xiao, H. Wang, Q.-Q. Wang, H. Zhang, P. K. Chu, *Small* **2016**, *12*, 4136.

[256] J. C. Song, F. Xia, M. Zhao, Y. L. Zhong, W. Li, K. P. Loh, R. A. Caruso, Q. L. Bao, *Chem. Mater.* **2015**, *27*, 3471.

[257] J. Yao, K. J. Koski, W. D. Luo, J. J. Cha, L. B. Hu, D. S. Kong, V. K. Narasimhan, K. F. Huo, Y. Cui, *Nat. Commun.* **2014**, *5*, 7.

[258] K. P. Chen, F. R. Chung, M. J. Wang, K. J. Koski, *J. Am. Chem. Soc.* **2015**, *137*, 5431.

[259] L. D. Alegria, M. D. Schroer, A. Chatterjee, G. R. Poirier, M. Pretko, S. K. Patel, J. R. Petta, *Nano Lett.* **2012**, *12*, 4711.

[260] G. Zhang, W. Wang, X. Lu, X. Li, *Cryst. Growth Des.* **2009**, *9*, 145.

[261] R. J. Mehta, Y. Zhang, C. Karthik, B. Singh, R. W. Siegel, T. Borca-Tasciuc, G. Ramanath, *Nat. Mater.* **2012**, *11*, 233.

[262] D. S. Kong, K. J. Koski, J. J. Cha, S. S. Hong, Y. Cui, *Nano Lett.* **2013**, *13*, 632.

[263] A. Ambrosi, Z. Sofer, J. Luxa, M. Pumera, *ACS Nano* **2016**, *10*, 11442.

[264] N. Bansal, M. R. Cho, M. Brahlek, N. Koirala, Y. Horibe, J. Chen, W. D. Wu, Y. D. Park, S. Oh, *Nano Lett.* **2014**, *14*, 1343.

[265] Y. F. Guo, J. Y. Zhou, Y. J. Liu, X. Zhou, F. R. Yao, C. W. Tan, J. X. Wu, L. Lin, K. H. Liu, Z. F. Liu, H. L. Peng, *Adv. Mater.* **2017**, *29*, 8.

[266] G. J. Xiao, K. Wang, L. Zhu, X. Tan, Y. C. Qiao, K. Yang, Y. M. Ma, B. B. Liu, W. T. Zheng, B. Zou, *J. Phys. Chem. C* **2015**, *119*, 3843.

[267] Y. Zhao, R. W. Hughes, Z. Su, W. Zhou, D. H. Gregory, *Angew. Chem., Int. Ed.* **2011**, *50*, 10397.

[268] W. Lu, Y. Ding, Y. Chen, Z. L. Wang, J. Fang, *J. Am. Chem. Soc.* **2005**, *127*, 10112.

[269] Y. Jiang, X. Zhang, Y. Wang, N. Wang, D. West, S. B. Zhang, Z. Zhang, *Nano Lett.* **2015**, *15*, 3147.

[270] V. Goyal, D. Teweldebrhan, A. A. Balandin, *Appl. Phys. Lett.* **2010**, *97*, 3.

[271] A. Matsumoto, Y. Koyama, A. Togo, M. Choi, I. Tanaka, *Phys. Rev. B* **2011**, *83*, 10.

[272] J. Zhou, B. Y. Yan, J. Yang, Y. Yang, W. Zhou, H. Lan, H. Wang, L. Guo, *Nanoscale* **2018**, *10*, 9108.

[273] F. Behnoudnia, H. Dehghani, *RSC Adv.* **2014**, *4*, 39672.

[274] S. L. Zhang, W. H. Zhou, Y. D. Ma, J. P. Ji, B. Cai, S. Y. A. Yang, Z. Zhu, Z. F. Chen, H. B. Zeng, *Nano Lett.* **2017**, *17*, 3434.

[275] J. Wang, Y. Qiao, T. Wang, H. Yu, Y. Feng, L. Li, *Inorg. Chem. Commun.* **2018**, *92*, 110.

[276] B. P. Lu, J. L. Tang, *Dalton Trans.* **2014**, *43*, 13948.

[277] W. Zhang, M. Tan, P. Zhang, L. N. Zhang, W. N. Dong, Q. S. Wang, J. W. Ma, E. L. Dong, S. C. Xu, G. Q. Wang, *Appl. Surf. Sci.* **2018**, *455*, 1063.

[278] Y. Liu, Z. Tai, J. Zhang, W. K. Pang, Q. Zhang, H. Feng, K. Konstantinov, Z. Guo, H. K. Liu, *Nat. Commun.* **2018**, *9*, 3645.

[279] N. Dhar, N. Syed, M. Mohiuddin, A. Jannat, A. Zavabeti, B. Y. Zhang, R. S. Datta, P. Atkin, N. Mahmood, D. Esrafilzadeh, T. Daeneke, K. Kalantar-Zadeh, *ACS Appl. Mater. Interfaces* **2018**, *10*, 42603.

[280] S. S. Yao, J. Cui, J. Q. Huang, Z. H. Lu, Y. Deng, W. G. Chong, J. X. Wu, M. Ihsan Ul Haq, F. Ciucci, J. K. Kim, *Adv. Energy Mater.* **2018**, *8*, 10.

[281] Y. Y. Zhu, P. Nie, L. F. Shen, S. Y. Dong, Q. Sheng, H. S. Li, H. F. Luo, X. G. Zhang, *Nanoscale* **2015**, *7*, 3309.

[282] H. B. Song, T. Y. Li, J. Zhang, Y. Zhou, J. J. Luo, C. Chen, B. Yang, C. Ge, Y. Q. Wu, J. Tang, *Adv. Mater.* **2017**, *29*, 7.

[283] Z. H. Miao, L. X. Fan, X. L. Xie, Y. Ma, J. Z. Xue, T. He, Z. B. Zha, *ACS Appl. Mater. Interfaces* **2019**, *11*, 26664.

[284] L. X. Fan, D. D. Huang, Y. C. Wang, Z. H. Miao, Y. Ma, Q. L. Zhao, Z. B. Zha, *Chem. Commun.* **2019**, *55*, 2805.

[285] Y. D. Zhou, W. Feng, X. Q. Qian, L. D. Yu, X. G. Han, G. L. Fan, Y. Chen, J. Zhu, *ACS Appl. Mater. Interfaces* **2019**, *11*, 19712.

[286] K. H. Nam, C. M. Park, *J. Power Sources* **2019**, *433*, 126639.

[287] a) W. D. Shi, L. Zhou, S. Y. Song, J. H. Yang, H. J. Zhang, *Adv. Mater.* **2008**, *20*, 1892; b) W. D. Shi, J. B. Yu, H. S. Wang, H. J. Zhang, *J. Am. Chem. Soc.* **2006**, *128*, 16490.

[288] T. Saltzmann, M. Bornhofft, J. Mayer, U. Simon, *Angew. Chem., Int. Ed.* **2015**, *54*, 6632.

[289] a) S. Singh, S. Hong, W. Jeon, D. Lee, J. Y. Hwang, S. Lim, G. D. Kwon, D. Pribat, H. Shin, S. W. Kim, S. Baik, *Chem. Mater.* **2015**, *27*, 2315; b) S. Singh, S. Kim, W. Jeon, K. P. Dhakal, J. Kim, S. Baik, *Carbon* **2019**, *153*, 164.

[290] W. D. Zhang, Q. Y. Zhang, Q. F. Shi, S. Xin, J. Wu, C. L. Zhang, L. F. Qiu, C. F. Zhang, *ACS Appl. Mater. Interfaces* **2019**, *11*, 29934.

[291] K. H. Nam, C. M. Park, *J. Mater. Chem. A* **2016**, *4*, 8562.

[292] S. Schulz, S. Heimann, J. Friedrich, M. Engenhorst, G. Schierning, W. Assenmacher, *Chem. Mater.* **2012**, *24*, 2228.

[293] a) G. H. Dong, Y. J. Zhu, L. D. Chen, *J. Mater. Chem.* **2010**, *20*, 1976; b) B. Xu, J. Zhang, G. Q. Yu, S. S. Ma, Y. S. Wang, Y. X. Wang, *J. Appl. Phys.* **2018**, *124*, 6.

[294] H. Sahin, S. Cahangirov, M. Topsakal, E. Bekaroglu, E. Akturk, R. T. Senger, S. Ciraci, *Phys. Rev. B* **2009**, *80*, 12.

[295] L. H. Li, Y. Chen, *Adv. Funct. Mater.* **2016**, *26*, 2594.

[296] a) L. H. Li, J. Cervenka, K. Watanabe, T. Taniguchi, Y. Chen, *ACS Nano* **2014**, *8*, 1457; b) H. Zhou, J. Zhu, Z. Liu, Z. Yan, X. Fan, J. Lin, G. Wang, Q. Yan, T. Yu, P. M. Ajayan, J. M. Tour, *Nano Res.* **2014**, *7*, 1232; c) L. Lindsay, D. A. Broido, *Phys. Rev. B* **2011**, *84*, 155421.

[297] R. C. Andrew, R. E. Mapasha, A. M. Ukpong, N. Chetty, *Phys. Rev. B* **2012**, *85*, 125428.

[298] L. Song, L. Ci, H. Lu, P. B. Sorokin, C. Jin, J. Ni, A. G. Kvashnin, D. G. Kvashnin, J. Lou, B. I. Yakobson, P. M. Ajayan, *Nano Lett.* **2010**, *10*, 3209.

[299] a) D. Pacilé, J. C. Meyer, Ç. Ö. Girit, A. Zettl, *Appl. Phys. Lett.* **2008**, *92*, 133107; b) C. Jin, F. Lin, K. Suenaga, S. Iijima, *Phys. Rev. Lett.* **2009**, *102*, 195505; c) W.-Q. Han, L. Wu, Y. Zhu, K. Watanabe, T. Taniguchi, *Appl. Phys. Lett.* **2008**, *93*, 223103; d) A. Nagashima, N. Tejima, Y. Gamou, T. Kawai, C. Oshima, *Phys. Rev. B* **1995**, *51*, 4606.

[300] K. Zhang, Y. Feng, F. Wang, Z. Yang, J. Wang, *J. Mater. Chem. C* **2017**, *5*, 11992.

[301] N. R. Glavin, C. Muratore, M. L. Jespersen, J. J. Hu, P. T. Hagerty, A. Hilton, A. T. Blake, C. A. Grabowski, M. F. Durstock, M. E. McConney, D. M. Hilgefort, T. S. Fisher, A. A. Voevodin, *Adv. Funct. Mater.* **2016**, *26*, 2640.

[302] K. K. Kim, A. Hsu, X. Jia, S. M. Kim, Y. Shi, M. Dresselhaus, T. Palacios, J. Kong, *ACS Nano* **2012**, *6*, 8583.

[303] F. X. Yang, L. Jin, L. J. Sun, X. C. Ren, X. L. Duan, H. J. Cheng, Y. K. Xu, X. T. Zhang, Z. P. Lai, W. Chen, H. L. Dong, W. P. Hu, *Adv. Mater.* **2018**, *30*, 7.

[304] Q. K. Qian, B. K. Li, M. Y. Hua, Z. F. Zhang, F. F. Lan, Y. K. Xu, R. Y. Yan, K. J. Chen, *Sci. Rep.* **2016**, *6*, 9.

[305] a) A. Sengupta, *Appl. Surf. Sci.* **2018**, *451*, 141; b) S. F. Rastegar, A. A. Peyghan, H. R. Ghenaatian, N. L. Hadipour, *Appl. Surf. Sci.* **2013**, *274*, 217; c) Y. Ding, Y. L. Wang, *J. Mater. Chem. C* **2016**, *4*, 1517.

[306] X. T. Zhang, Z. Liu, S. K. Hark, *Solid State Commun.* **2007**, *143*, 317.

[307] P. Wang, T. Wang, H. Wang, X. X. Sun, P. Huang, B. W. Sheng, X. Rong, X. T. Zheng, Z. Y. Chen, Y. X. Wang, D. Wang, H. P. Liu, F. Liu, L. Y. Yang, D. Li, L. Chen, X. L. Yang, F. J. Xu, Z. X. Qin, J. J. Shi, T. J. Yu, W. K. Ge, B. Shen, X. Q. Wang, *Adv. Funct. Mater.* **2019**, *29*, 7.

[308] W. L. Wang, Y. L. Zheng, X. C. Li, Y. Li, H. Zhao, L. G. Huang, Z. C. Yang, X. N. Zhang, G. Q. Li, *Adv. Mater.* **2019**, *31*, 9.

[309] E. Durgun, S. Tongay, S. Ciraci, *Phys. Rev. B* **2005**, *72*, 075420.

[310] A. V. Kolobov, P. Fons, J. Tominaga, B. Hyot, B. André, *Nano Lett.* **2016**, *16*, 4849.

[311] a) D. C. Camacho-Mojica, F. López-Urías, *Sci. Rep.* **2016**, *5*, 17902; b) H. Zhang, F.-S. Meng, Y.-B. Wu, *Solid State Commun.* **2017**, *250*, 18.

[312] Z. Y. Al Balushi, K. Wang, R. K. Ghosh, R. A. Vila, S. M. Eichfeld, J. D. Caldwell, X. Y. Qin, Y. C. Lin, P. A. DeSario, G. Stone, S. Subramanian, D. F. Paul, R. M. Wallace, S. Datta, J. M. Redwing, J. A. Robinson, *Nat. Mater.* **2016**, *15*, 1166.

[313] W. Wang, Y. Li, Y. Zheng, X. Li, L. Huang, G. Li, **2019**, *15*, 1802995.

[314] Y. Chen, K. Liu, J. Liu, T. Lv, B. Wei, T. Zhang, M. Zeng, Z. Wang, L. Fu, *J. Am. Chem. Soc.* **2018**, *140*, 16392.

[315] T. Imaoka, T. Okada, S. Samukawa, K. Yamamoto, *ACS Appl. Mater. Interfaces* **2017**, *9*, 41629.

[316] P. Kocinski, M. Zbroszczyk, *Semicond. Sci. Technol.* **1995**, *10*, 1452.

[317] S. Ullah, P. A. Denis, F. Sato, *Appl. Surf. Sci.* **2019**, *471*, 134.

[318] D. Cakir, D. Kecik, H. Sahin, E. Durgun, F. M. Peeters, *Phys. Chem. Chem. Phys.* **2015**, *17*, 13013.

[319] B. Onat, L. Hallioglu, S. İpek, E. Durgun, *J. Phys. Chem. C* **2017**, *121*, 4583.

[320] T.-T. Yu, P.-F. Gao, Y. Zhang, S.-L. Zhang, *Appl. Surf. Sci.* **2019**, *486*, 281.

[321] H. R. Jiang, W. Shyy, M. Liu, L. Wei, M. C. Wu, T. S. Zhao, *J. Mater. Chem. A* **2017**, *5*, 672.

[322] A. Akbari, M. Naseri, J. Jalilian, *Chem. Phys. Lett.* **2018**, *691*, 181.

[323] A. Kelrich, O. Sorias, Y. Calahorra, Y. Kauffmann, R. Gladstone, S. Cohen, M. Orenstein, D. Ritter, *Nano Lett.* **2016**, *16*, 2837.

[324] W. Yi, X. Chen, Z. Wang, Y. Ding, B. Yang, X. Liu, *J. Mater. Chem. C* **2019**, *7*, 7352.

[325] N. H. Miao, B. Xu, N. C. Bristowe, J. Zhou, Z. M. Sun, *J. Am. Chem. Soc.* **2017**, *139*, 11125.

[326] T. Ouyang, E. L. Jiang, C. Tang, J. Li, C. Y. He, J. X. Zhong, *J. Mater. Chem. A* **2018**, *6*, 21532.

[327] J. Liu, C.-S. Liu, X.-J. Ye, X.-H. Yan, *J. Mater. Chem. A* **2018**, *6*, 3634.

[328] M. Ashton, S. B. Sinnott, R. G. Hennig, *Appl. Phys. Lett.* **2016**, *109*, 192103.

[329] B. C. Revard, W. W. Tipton, A. Yesypenko, R. G. Hennig, *Phys. Rev. B* **2016**, *93*, 054117.

[330] J. H. Lin, H. Zhang, X. L. Cheng, Y. Miyamoto, *Phys. Rev. B* **2017**, *96*, 12.

**ADVANCED
SCIENCE NEWS**
www.advancedsciencenews.com

**ADVANCED
FUNCTIONAL
MATERIALS**
www.afm-journal.de

[331] S. L. Zhang, S. Y. Guo, Y. X. Huang, Z. Zhu, B. Cai, M. Q. Xie, W. H. Zhou, H. B. Zeng, *2D Mater.* **2017**, *4*, 6.

[332] F. Shojaei, H. S. Kang, *J. Phys. Chem. C* **2016**, *120*, 23842.

[333] J. Guo, Y. Liu, Y. Ma, E. B. Zhu, S. Lee, Z. X. Lu, Z. P. Zhao, C. H. Xu, S. J. Lee, H. Wu, K. Kovnir, Y. Huang, X. F. Duan, *Adv. Mater.* **2018**, *30*, 6.

[334] a) S. X. Yang, Y. H. Yang, M. H. Wu, C. G. Hu, W. F. Shen, Y. J. Gong, L. Huang, C. B. Jiang, Y. Z. Zhang, P. M. Ajayan, *Adv. Funct. Mater.* **2018**, *28*, 10; b) C. S. Jung, D. Kim, S. Cha, Y. Myung, F. Shojaei, H. G. Abbas, J. A. Lee, E. H. Cha, J. Park, H. S. Kang, *J. Mater. Chem. A* **2018**, *6*, 9089.

[335] F. Q. Wang, Y. G. Guo, Q. Wang, Y. Kawazoe, P. Jena, *Chem. Mater.* **2017**, *29*, 9300.

[336] P. Li, W. Zhang, D. Li, C. Liang, X. C. Zeng, *ACS Appl. Mater. Interfaces* **2018**, *10*, 19897.

[337] Z. Q. Li, X. Z. Shi, C. Y. He, T. Ouyang, J. Li, C. X. Zhang, S. F. Zhang, C. Tang, R. A. Romer, J. X. Zhong, *Surf. Sci.* **2019**, *680*, 6.

[338] F. Shojaei, H. S. Kang, *Phys. Chem. Chem. Phys.* **2016**, *18*, 32458.

[339] L. Li, W. Wang, P. Gong, X. Zhu, B. Deng, X. Shi, G. Gao, H. Li, T. Zhai, **2018**, *30*, 1706771.

[340] D. Kim, K. Park, F. Shojaei, T. T. Debela, I. S. Kwon, I. H. Kwak, J. Seo, J. P. Ahn, J. Park, H. S. Kang, *J. Mater. Chem. A* **2019**, *7*, 16526.

[341] F. Shojaei, J. R. Hahn, H. S. Kang, *J. Mater. Chem. A* **2017**, *5*, 22146.

[342] Y. Jing, Y. Ma, Y. Li, T. Heine, *Nano Lett.* **2017**, *17*, 1833.

[343] M. S. Ramzan, V. Bacic, Y. Jing, A. Kuc, *J. Phys. Chem. C* **2019**, *123*, 25470.

[344] K.-H. Nam, K.-J. Jeon, C.-M. Park, *Energy Storage Mater.* **2019**, *17*, 78.

[345] X. Y. Deng, X. F. Chen, Y. Huang, B. B. Xiao, H. Y. Du, *J. Phys. Chem. C* **2019**, *123*, 4721.

[346] C. H. Zhang, G. T. Yu, R. Q. Ku, X. R. Huang, W. Chen, *Appl. Surf. Sci.* **2019**, *481*, 272.

[347] H. H. Wu, H. Huang, J. Zhong, S. Yu, Q. B. Zhang, X. C. Zeng, *Nanoscale* **2019**, *11*, 12210.

[348] a) S. S. Sun, F. C. Meng, H. Y. Wang, H. Wang, Y. X. Ni, *J. Mater. Chem. A* **2018**, *6*, 11890; b) L. P. Feng, A. Li, P. C. Wang, Z. T. Liu, *J. Phys. Chem. C* **2018**, *122*, 24359; c) B. Ghosh, S. Puri, A. Agarwal, S. Bhowmick, *J. Phys. Chem. C* **2018**, *122*, 18185.

[349] C. S. Liu, X. L. Yang, J. Liu, X. J. Ye, *ACS Appl. Energy Mater.* **2018**, *1*, 3850.

[350] S. Y. Wu, Y. Q. Shen, X. Gao, Y. Y. Ma, Z. X. Zhou, *Nanoscale* **2019**, *11*, 18628.

[351] R. Weihrich, V. Eyert, S. F. Matar, *Chem. Phys. Lett.* **2003**, *373*, 636.

[352] H. K. Liu, G. Z. Qin, Y. Lin, M. Hu, *Nano Lett.* **2016**, *16*, 3831.

[353] T. He, M. Zhao, W. Li, C. Song, X. Lin, X. Liu, Y. Xia, L. Mei, *J. Phys. Chem. C* **2007**, *111*, 16840.

[354] J. Z. Jiang, F. Kragh, D. J. Frost, K. Ståhl, H. Lindelov, *J. Phys.: Condens. Matter* **2001**, *13*, L515.

[355] X. W. Zhu, Y. Sakka, *Sci. Technol. Adv. Mater.* **2008**, *9*, 033001.

[356] T. Taguchi, H. Yamamoto, S. Shamoto, *Nanotechnology* **2008**, *19*, 485601.

[357] K. Kumagai, M. Suzuki, T. Sekiguchi, *J. Appl. Phys.* **2012**, *111*, 7.

[358] S. Dong, P. Hu, X. H. Zhang, Y. Cheng, D. Y. Zhang, L. W. Yan, G. Q. Chen, *J. Mater. Chem. C* **2016**, *4*, 11212.

[359] L. Xiong, J. H. Dai, B. Zhong, G. W. Wen, Y. Song, *Phys. Chem. Chem. Phys.* **2014**, *16*, 24266.

[360] W. Y. Yu, C. Y. Niu, Z. L. Zhu, X. F. Wang, W. B. Zhang, *J. Mater. Chem. C* **2016**, *4*, 7.

[361] W. Z. Xiao, G. Xiao, Q. Y. Rong, L. L. Wang, *Phys. Chem. Chem. Phys.* **2018**, *20*, 22027.

[362] H. Zhang, M. Y. Chen, *J. Mater. Chem. C* **2018**, *6*, 11694.

[363] S. Y. Guo, W. H. Zhou, B. Cai, K. Zhang, S. L. Zhang, H. Zeng, *Nanoscale Horiz.* **2019**, *4*, 1145.

[364] Y. Z. Nie, M. Rahman, D. W. Wang, C. Wang, G. H. Guo, *Sci. Rep.* **2015**, *5*, 6.

[365] Y. Z. Nie, M. Rahman, P. Liu, A. Sidike, Q. L. Xia, G. H. Guo, *Phys. Rev. B* **2017**, *96*, 7.

[366] H. Yin, J. Gao, G.-P. Zheng, Y. Wang, Y. Ma, *J. Phys. Chem. C* **2017**, *121*, 25576.

[367] C. Liu, W. H. Wan, J. Ma, W. Guo, Y. G. Yao, *Nanoscale* **2018**, *10*, 7984.

[368] M. Q. Xie, S. L. Zhang, B. Cai, Y. Huang, Y. S. Zou, B. Guo, Y. Gu, H. B. Zeng, *Nano Energy* **2016**, *28*, 433.

[369] Z. Zhu, J. Guan, D. Tomanek, *Nano Lett.* **2015**, *15*, 6042.

[370] B. L. Liu, M. Kopf, A. N. Abbas, X. M. Wang, Q. S. Guo, Y. C. Jia, F. N. Xia, R. Weihrich, F. Bachhuber, F. Pielnhofer, H. Wang, R. Dhall, S. B. Cronin, M. Y. Ge, X. Fang, T. Nilges, C. W. Zhou, *Adv. Mater.* **2015**, *27*, 4423.

[371] F. Shojaei, H. S. Kang, *J. Phys. Chem. C* **2015**, *119*, 20210.

[372] Y. J. Sun, Z. G. Shuai, D. Wang, *Phys. Chem. Chem. Phys.* **2018**, *20*, 14024.

[373] J. Sun, N. Lin, H. Ren, C. Tang, L. T. Yang, X. Zhao, *Phys. Chem. Chem. Phys.* **2016**, *18*, 9779.

[374] E. P. Young, J. Park, T. Y. Bai, C. Choi, R. H. DeBlock, M. Lange, S. Poust, J. Tice, C. Cheung, B. S. Dunn, M. S. Goorsky, V. Ozolins, D. C. Streit, V. Gambin, *ACS Appl. Nano Mater.* **2018**, *1*, 4737.

[375] M. Amani, E. Regan, J. Bullock, G. H. Ahn, A. Javey, *ACS Nano* **2017**, *11*, 11724.

[376] M. S. Long, A. Y. Gao, P. Wang, H. Xia, C. Ott, C. Pan, Y. J. Fu, E. F. Liu, X. S. Chen, W. Lu, T. Nilges, J. B. Xu, X. M. Wang, W. D. Hu, F. Miao, *Sci. Adv.* **2017**, *3*, 7.

[377] X. Y. Cai, Y. Z. Chen, B. Sun, J. Chen, H. Y. Wang, Y. X. Ni, L. Tao, H. Wang, S. H. Zhu, X. M. Li, Y. C. Wang, J. Lv, X. L. Feng, S. A. T. Redfern, Z. F. Chen, *Nanoscale* **2019**, *11*, 8260.

[378] S. Y. Ma, C. Y. He, L. Z. Sun, H. P. Lin, Y. Y. Li, K. W. Zhang, *Phys. Chem. Chem. Phys.* **2015**, *17*, 32009.

[379] X. H. Tan, Y. J. Ji, H. L. Dong, M. Y. Liu, T. J. Hou, Y. Y. Li, *RSC Adv.* **2017**, *7*, 50239.

[380] F. Baumer, Y. Q. Ma, C. F. Shen, A. Y. Zhang, L. Chen, Y. H. Liu, D. Pfister, T. Nilges, C. W. Zhou, *ACS Nano* **2017**, *11*, 4105.

[381] T. Teshome, A. Datta, *J. Phys. Chem. C* **2018**, *122*, 15047.

[382] S. L. Zhang, M. Q. Xie, B. Cai, H. J. Zhang, Y. D. Ma, Z. F. Chen, Z. Zhu, Z. Y. Hu, H. B. Zeng, *Phys. Rev. B* **2016**, *93*, 7.

[383] L. Z. Kou, Y. D. Ma, X. Tan, T. Frauenheim, A. J. Du, S. Smith, *J. Phys. Chem. C* **2015**, *119*, 6918.

[384] X. T. Sun, Y. X. Liu, Z. G. Song, Y. D. Li, W. Z. Wang, H. P. Lin, L. Wang, Y. Y. Li, *J. Mater. Chem. C* **2017**, *5*, 4159.

[385] S. D. Guo, J. T. Liu, *Phys. Chem. Chem. Phys.* **2017**, *19*, 31982.

[386] P. Zhao, J. W. Li, W. Wei, Q. L. Sun, H. Jin, B. B. Huang, Y. Dai, *Phys. Chem. Chem. Phys.* **2017**, *19*, 27233.

[387] N. Zhao, Y. F. Zhu, Q. Jiang, *J. Mater. Chem. C* **2018**, *6*, 2854.

[388] S. Singh, A. H. Romero, *Phys. Rev. B* **2017**, *95*, 10.

[389] J. R. Yuan, Y. Q. Cai, L. Shen, Y. Xiao, J. C. Ren, A. Z. Wang, Y. P. Feng, X. H. Yan, *Nano Energy* **2018**, *52*, 163.

[390] W. Y. Yu, C. Y. Niu, Z. L. Zhu, X. L. Cai, L. W. Zhang, S. Y. Bai, R. Q. Zhao, Y. Jia, *RSC Adv.* **2017**, *7*, 27816.

[391] T. Hirahara, Y. Sakamoto, Y. Saisyu, H. Miyazaki, S. Kimura, T. Okuda, I. Matsuda, S. Murakami, S. Hasegawa, *Phys. Rev. B* **2010**, *81*, 5.

[392] Y. Ueda, N. H. D. Khang, K. Yao, P. N. Hai, *Appl. Phys. Lett.* **2017**, *110*, 5.